Fabrication of a new Cu-Ni bi metallic substrate and deposition of La2Zr2O7 (LZO) film on metallic substrate by chemical solution deposition process.

Zeming Yu

To cite this version:

Zeming Yu. Fabrication of a new Cu-Ni bi metallic substrate and deposition of La2Zr2O7 (LZO) film on metallic substrate by chemical solution deposition process.. Material chemistry. Université Joseph-Fourier - Grenoble I, 2008. English. NNT : . tel-00376983

HAL Id: tel-00376983
https://theses.hal.science/tel-00376983

Submitted on 20 Apr 2009

Northeastern University, Shenyang, China

Université Joseph Fourier — Grenoble 1, France

Ecole Doctorale
Physique /Science des matériaux

Doctorat
Physique des Matériaux

YU Zeming

Fabrication of a new Cu-Ni bi metallic substrate and deposition of $La_2Zr_2O_7$ (LZO) film on metallic substrate by chemical solution deposition process.

Thèse dirigée par: Zhou Lian/Odier philippe

Soutenue le 19 juin 2008

Jury:

Professor Liu Chunming	rapporteur
Doctor Zhang Yudong	rapporteur
Professor Wang Yandong	examinateur
Professor Noudem Jacques	examinateur
Professor Zhou Lian	co-directeur de thèse
Doctor Odier Philippe	co-directeur de thèse

Acknowledgement

I would like to express honestly my gratitude to my advisors, Dr. P. Odier, Prof. L. Zhou, and Prof. P.X. Zhang, for their support, guidance and enthusiasm. Their knowledge of science, ability to solve the hard questions and humbleness impress on me. I feel very fortunate to have a chance to work with them. It is unimaginable for me to finish all the experiments without their support and help. And I am also grateful to their contribution to my professional and personal growth. They have shown me a way to get finial success, and told me how to enjoin it. To work with them has become the most important experience in my life.

All my experiments were finished in Superconducting materials researching center (SMRC) in Northwest Institute for Nonferrous Metal Research and Laboratoire de Cristallographie CNRS. During I worked at SMCR, Director Lu Yafeng, Director LI Chengshan and vice director Yan Guo offered the favourable experiment conditions, and discussion with them was very helpful to finish my thesis. I greatly appreciate them. My other colleagues, Mrs. Duan Ying, Mrs. Xiong Xiaomei, Mrs. Zheng Huiling, Mrs. Xu Xiaoyan, Mr. Jin Lihua, Mr. Hao Qingpin, Mr. Wang Qingyang, Mr. Liang Ming and Mr. Liu Guoqing, also gave me a hand. I wish to give my thanks to them. Besides the internal colleagues, I am fortunate enough to get the chance to conduct experiments with my French friends in Laboratoire de Cristallographie. Dr L. Ortega is acknowledged for many technical assistance and helpful discussions. Discussion with Dr. A. Girard and Dr. S. Morlens was very helpful to me. And I also express my special gratitude to Prof. A. Suplice, Dr. Ph. David, Dr. O. Fruchart for measuring my samples.

In aspect of my personal growth, I would like to appreciate Mr. Meng Decheng, the chief of human resource of Northwest Institute for Nonferrous Metal Research. Without his help, I can not focus all my energy on my experiments. And Mrs. Wang Jun also helped me a lot. I would like to express my gratitude to Prof. A. Suplice. I not only got a lot help from Prof. A.Suplice in my experiment, but also got many help from Prof. A. Suplice during I lived in France.

Finally, Special gratitude is owed to my wife, Li Qinghong. She never let me worry about my family, and make me focus all energy on my researching.

The author thanks for the financial support of the French embassy in Beijing, the International Laboratory for the Applications of Superconductor and Magnetic Materials (LAS2M-CNRS-NIN), the National High Technology Research and Development Program of China (863 Program) under contracts Nos. 2006AA03Z202 and 2006AA03Z204, and French ANR-Madisup project.

A word of thanks is given to all the people who help me!

Abstract

In this dissertation, a new Cu-Ni bi-metallic substrate is developed by electro-depositing Ni layer on a cube-textured Cu tape, and other main discussion is about how to fabricate cube-textured $La_2Zr_2O_7$(LZO) film on metallic substrate by chemical solution deposition (CSD) process.

Rolling-recrystallization process to obtain a cube-textured Cu tape was studied. The results show there is a critical rolling deformation rate to obtain a cube textured Cu tape before the final recrystallizing annealing. Other rolling parameters do not influence whether the cube-textured Cu tape is obtained or not, but they would influence the sharpness of cube texture of Cu tape. Studying recrystallization annealing shows the volume fraction of cube texture of Cu tape increases with increasing the annealing temperature, and it also can be found the growth speed of cube texture in Cu tape is very rapid.

A cube-textured Ni layer can be deposited on a cube-textured Cu tape by electro-deposition only if the cathode potential is lower than -0.96V (SEC), and the pH value is the range from 4 to 5, and the temperature of electrolyte is room temperature. It has also been proved that it is impossible that a cube-textured Ni layer is deposited on a cube-textured Cu tape which is polished mechanically.

It is obvious that the magnetic loss induced by Cu-Ni bi-metallic substrate is lower than one induced by Ni-5at%W substrate.

In order to deposit a cube-textured LZO film on metallic substrate, preparation of precursor solution and heat-treatment of precursor film were studied. It is clear that propionic acid is a good solvent for preparing a good precursor solution. A simple sulfuration process was reported to control the orientation of initial LZO layer formed on the surface of metallic substrate. The residual carbon in LZO precursor film is main inhibiting factor to the growth of LZO grains, and increasing the gas speed flowing over the sample is the best way to improve the epitaxial growth of LZO film on metallic substrate.

Key words: coated conductors, Cu-Ni bi-metallic substrate, $La_2Zr_2O_7$ buffer layer, rolling-recrystallization, electrodeposition, sulfuration, chemical solution deposition

Contents

Introduction

Background

Due to a strong anisotropy of superconducting property of YBa_2Cu_3Oy (YBCO), large grains boundary angle results in the problem of “weak link” which means that the intergrain critical current density is lower than the intragrain current density. So to be usable YBCO superconductor in practice all YBCO grains should be arranged along a special orientation. In the early stage of research, it was clear that the melt-textured process was a good method to fabricate the textured YBCO superconductors. But due to the high heat-treatment temperature used in melt-textured process, it can only fabricate bulk superconductors. However, flexible superconducting tapes are necessary in many application fields, for example, motor, cable, magnet, and so on. In order to extend the application field of YBCO superconductors, a method to fabricate YBCO tapes should be developed. In 1990’s, researchers in USA and in Japan found that it was possible to deposit a textured YBCO film on a textured metallic substrate to obtain YBCO tapes. This idea provides a new method to fabricate YBCO superconductors, and extends the application fields of YBCO superconductors.

Comparing with Bi-2223/Ag tapes, YBCO tapes own better superconducting property under a high applied magnetic field. At the same time, the cost of raw materials which are used for fabricating YBCO tapes is cheap because there is no Ag. So it is believed that YBCO tapes will replace the Bi-2223/Ag tapes in future. YBCO tapes are also called coated conductors.

The structure of coated conductors can be divided into four parts: metallic substrate, buffer layer, YBCO layer and protecting layer. The functions of the four parts are as follow: the metallic substrate is a mechanical carrier and origin of texture for coated conductors; the buffer layer prevents diffusion of metallic elements into YBCO layer, and transmits the texture from the metallic substrate to YBCO layer; YBCO layer is the major part which carries the supercurrent; the protecting layer prevents YBCO layer from corrosion and mechanical degradations, it also serves as an electrical shunt.

From the viewpoints of material, the metallic substrate is usually fabricated by Ni-W alloys but hastelloy or steel are also used. Because the Curie temperature of most of Ni-W alloys is higher than 77K, Cu and Cu-based alloys attract interest to many researchers. In a word, material researchers try to develop a cube-textured substrate with lower magnetic property and high mechanical strength. Because the buffer layer should take multi-functions, the architecture of buffer layers is usually composed of two or three oxide layers. In order to simplify the fabrication process of coated conductors and decrease its cost, it is a main challenge for material researchers to simplify the structure of buffer layer. ReBCO superconducting layers are studied, but the attention of researchers is mainly focused on YBCO. The protecting is usually made of Cu layer on top of a Ag layer.

From the viewpoints of fabrication process of each layers, Ion Beam Assisted Deposition (IBAD) process and Rolling Assisted Biaxially Textured Substrate (RABiTS) are the main two methods used to obtain textured substrates. The fabrication process of the buffer layer can be divided into two classes: physical vapor deposition (PVD) and chemical solution deposition (CSD). Because the architecture of the buffer layer is usually composed of two or three oxide layers, a successful architecture of buffer layer is usually fabricated by a combination of multi-technologies. However, with simplifying the structure of buffer layer, it could be foreseen that the use of a single method like CSD process will become possible. It is believed that the metalorganic deposition using trifluoroacetates (TFA-MOD) is the best method to deposit economically YBCO layer with high superconducting property. The protecting layer is obtained by electro-deposition.

Objectives and aims

Based on the above-mentioned review, it can be found that the development of cube-textured metallic substrate with sharp texture, high mechanical strength and low magnetic property is one of the important research fields for coated conductors. Another two highlights of research for coated conductors are to deposit the buffer layer by chemical solution processes and to deposit the YBCO layer by TFA-MOD process.

So the development of cube-textured metallic substrate with sharp texture and deposition of buffer layer on metallic substrate by CSD process have been studied in this dissertation.

In order to obtain cube-textured metallic substrate with sharp texture and low magnetic property, a new Cu-Ni bi-metallic substrate was developed. The characteristic of this new substrate is that Ni layer is deposited on a cube-textured Cu tape by electro-deposition. After Ni layer is deposited on the Cu tape, it can overcome the disadvantages of pure Cu substrate which has low thermal stability of texture and poor oxidization resistance. The advantages of this new substrate are a sharper cube texture and a low magnetization. After the heat-treatment required by the deposition process of buffer layer and YBCO layer, the interdiffusion of Cu with Ni layer would decrease the global magnetic moment wear by the substrate compared to that of the Ni layer.

We consider $La_2Zr_2O_7$ (LZO) as a good material for the buffer layer. In order to obtain cube-textured LZO film with good surface texture and crystallinity on metallic substrate, the nucleation stage and growth stage during deposition of LZO film was considered. Nucleation of an oxide film on a metal surface is not fully understood, it involves the complex formation of ionic/non-ionic interface. On the other hand, a slight irreproducibility in the buffer layer texture is not tolerated for a long YBCO tape. Recently, researchers in United States found that c(2x2)-S superstructure on Ni substrate was of benefit to obtaining a cube-textured oxide film on Ni substrate. But the efficiency of c(2x2)-S superstructure was only proved in PVD process, no body could tell if c(2x2)-S superstructure was useful or not in CSD process. So a simple way to obtain a c(2x2)-S superstructure on metallic substrate was developed firstly, and then its influence on the texture of LZO film was studied.

Due to a large crystallization driving force in CSD process, it is possible that the homogenous nucleation takes place in the bulk and top layer of LZO precursor film. It results in a poor texture on the top layer of final LZO film. This can not be tolerated. The sharp cube texture from bottom to top layer of LZO film, especially surface texture of final LZO film, is necessary. In this dissertation, the thermodynamic analysis about pyrolysis of LZO precursor film was done. Based on this analysis, the epitaxial growth of LZO film was optimized to obtain cube-textured LZO film with good surface texture and crystallinity.

Overview of this dissertation

In previous parts, researching background and research objectives were featured. According to the researching fields in this dissertation, this dissertation is organized in following manner.

Chapter I is the literature view about how to fabricate coated conductors.

Chapter II focuses on the fabrication of sharpe cube-textured Cu substrate.

Chapter III analyzes the process of depositing cube-textured Ni layer on Cu substrate by electro-deposition.

Chapter IV presents how to obtain a good precursor solution for depositing $La_2Zr_2O_7$(LZO) film, and reports some results about deposition of LZO film on constantan substrate.

Chapter V introduces a process of obtaining a c(2x2)-S superstructure on metallic substrate, and discuss the influence of c(2x2)-S superstructure on the texture of LZO films.

Chapter VI describes in detail improvement of epitaxial growth of LZO film with a good surface texture and crystallinity on metallic substrate.

Chapter I Literatures Review

1.1 Coated Conductors

Since $YBa_2Cu_3O_{7-x}$(YBCO) superconductor has be found[1-2] in 1987, research of high-Tc superconducting material has developed enormously. Bismuth-system, Tl-system and Hg-system were found one after the other. In aspect of practical application, many research are focused on YBCO superconducting material and Bi-2212 and Bi-2223 superconducting materials. Comparing with Bi-2223 superconductor, YBCO superconductor have stronger intrinsic flux pinning force, and good superconducting properties under high magnetic field at 77K. Except for temperature lower than 30K, the critical current density of Bi-2223 superconductor decreases rapidly with increasing the magnetic field. So under high magnetic field at 77K, YBCO superconductor is the best choice. Results in Fig.1.1[3] compare the irreversibility field of different superconducting materials, it indicates that YBCO superconductor is better than other superconducting material at the boiling point of liquid nitrogen.

Due to the anisotropy of superconducting properties of YBCO and Bi-2223 superconducting material, the first thing that must be done is to control the orientation of grains in order to improve the superconducting properties. Comparing with YBCO material, Bi-2223 grains can be partially textured by cold working and heat-treatment process, and the temperature of processing of Bi-2223 is lower (<850°C)[4-8]. Due to these characteristics, the powder-in-tube process is the main process to fabricate the Bi-2223 superconductors. This process is inapplicable to fabricate YBCO superconductor with high current density. In order to decrease the “weak-link” induced by large misorientation angle, the melt-textured processes were experimented by many research groups[9-11]. The melting process is a good way to overcome the “weak-link”, but it needs high annealing temperature (>1015°C), and molten parts can degrade most kind of metals, except Ag and Pt. So the melt-textured process can be used only to fabricate rods of YBCO superconductors. It limits the practical applications of YBCO superconductor. Considering that the main application of superconductors is in the field of cables or magnets, the fabrication of the long tape is the key to the development of YBCO superconductor.

Y.Iijima[12] has fabricated successfully biaxially textured YBCO layer on a flexible metal substrate by Ion Beam Assisted Deposition (IBAD) process opening a new way to fabricate YBCO superconductors. But IBAD technology has some disadvantages: a high cost and a low deposition speed. Then a new route was discovered by D. Norton [13] and A. Goyal [14] using a cube-textured Ni substrate produced by a rolling-heat treatment process as a template to grow the YBCO layer by epitaxial growth. They named this route of substrate processing “Rolling Assisted Biaxially Textured Substrates” or RABiTS. Due to the outcome of IBAD and RABiTS routes, the YBCO deposited layer on the biaxially textured flexible metal substrate induces the replacement of Bi-2223/Ag tapes, first generation tape. The YBCO tapes are also called coated conductors or G conductors.

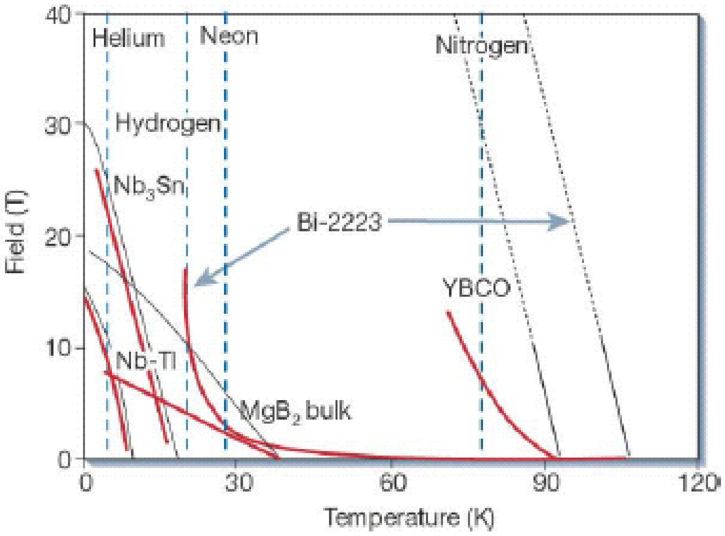

Fig. 1.1 Irreversibility field of different superconductors vs. temperature[3]

1.2 Structure of Coated Conductors and Functions of Substructure of Coated Conductors

Because of the anisotropic superconducting properties of YBCO, misorientation angle between adjacent grains affects obviously the transport properties of YBCO superconductors (shown in figure 1.2)[15,16]. The orientation of YBCO grains is the first question which must be solved. A c-axial orientation of YBCO grains is achieved in the melt-textured processes, but at high annealing temperature. But the only control of the orientation of c axes of YBCO grains is not sufficient for carrying high critical current. In order to transport large current, the orientation of YBCO grains must be biaxially textured, that is c axes and a axes of YBCO grains are parallel to each other respectively. In other words, not only c axises of YBCO grains are oriented, but also a or b axes of YBCO grains must be arranged with special orientations. These differences are shown in figure 1.3.

Iijima[12] and Norton[13] succeeded to grow YBCO film on bi-axially textured flexible metals. It not only solves the orientation of YBCO grains, but also overcomes the disadvantages of melt-textured process. Analyzing their reports shows that a coated conductor can be divided into three main parts: a metal substrate (or flexible template), a buffer layer and a YBCO film. In practice, besides these three layers, a protecting layer is also necessary to prevent the YBCO film from being corroded by different atmospheres or mechanical erosion and also serves as a shunt layer. The figure 1.4 shows the architecture of coated conductor.

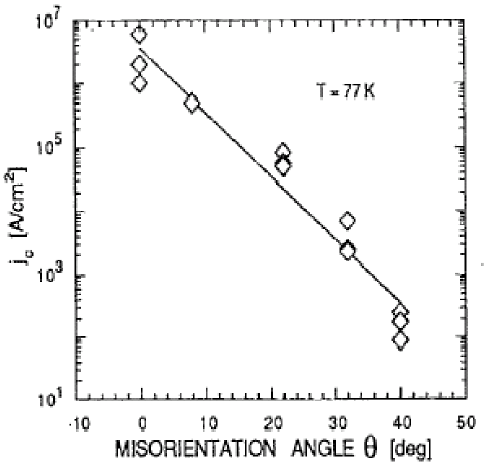

Fig. 1.2 Effect of misorientation angle on the Jc value[15]

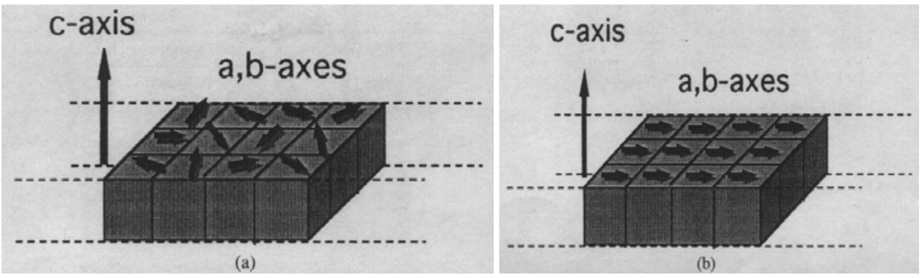

Fig. 1.3 The texture difference between the melting process and biaxial texture

a: Texture after melting process

b: Biaxial texture which is necessary for coated conductor

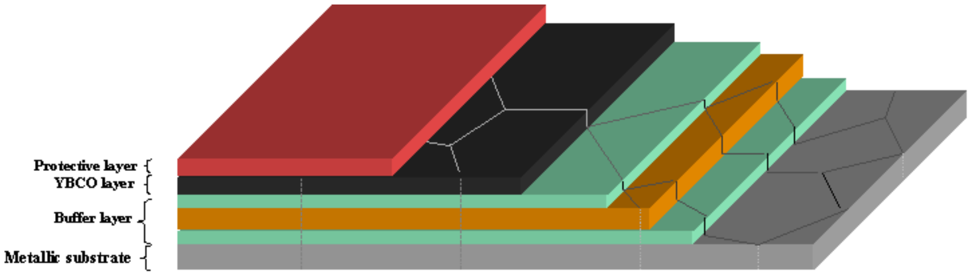

Fig. 1.4 Architecture of coated conductor

The metal substrate plays the role of a mechanical carrier, but it is also flexible. Another function of the metal substrate is to be used as a template to transmit the texture. The metal substrate is a biaxially textured tape (RABiTS process), or is polycrystalline (IBAD process). If the metal substrate is polycrystalline, the texture is given by the biaxial textured oxide film which is deposited on the polycrystalline metal substrate by IBAD process. Except Ag or Pt, most metallic elements degrade the superconducting properties of YBCO if they diffuse into it. So to prevent such diffusion is essential and the main function of buffer layers. At the same time, buffer layers also prevent oxidation of the metal substrate during the fabrication process of the YBCO layer. Besides the chemical resistance, transmitting the texture and decreasing the lattice mismatch between metal substrate and YBCO are essential functions of the buffer layers. The YBCO layer is the core of the coated conductor which carries the super-current. The protecting layer prevents the degradation of the properties of YBCO that could be induced by any circumstance. Because the considered buffer layers are oxide, and dielectric, the protection in the case of overcurrents must be considered. So another function of the protecting layer is the electrical stabilization of the tape.

1.3 Choice of Material and Fabrication of Coated Conductors

Recently, most of the researchers focus their work on the three following aspects about coated conductors: fabrication technology of metallic substrates, deposition technologies of buffer layer and deposition technologies of the YBCO layer. The issues related to these three aspects will be discussed below.

1.3.1 Substrate

1.3.1.1 Substrate Material

Coated conductors are obtained by hetero-epitaxial growth of YBCO on the metal substrate with intermediate buffer layers. In order to obtain a bi-axially textured YBCO layer, the metal substrate must have be a single texture component, at the same time the mismatch of crystal lattice between YBCO and the metal substrate must be as small as possible. Ni is a face-centered cubic metal, it is easy to obtain a high volume fraction of cube texture by rolling-heat treatment process. Concerning the mismatch of crystal lattice between YBCO and the metal substrate, due to the parameter of crystal lattice of Ni (0.3524nm), the mismatch with YBCO is –8.57%. So based on the viewpoint of cube texture and mismatch of crystal lattice, Ni is the first candidate of metal substrate material [13, 14, 17, 18]. But pure Ni is ferromagnetic and mechanically too soft. It is a strong disadvantage in practical application if pure Ni is to be used as substrate. Recently, several research groups focused on the Ni-based alloy, and wanted to increase the mechanical strength and decrease the Curie temperature of Ni-based substrate by alloying. About these Ni-based alloy, for example Ni-W[19-23], Ni-Cr[24,25] and Ni-Cu[26,27] and others, Ni-W alloy has been highlighted. Considering the decrease the AC loss, a non-ferromagnetic substrate is the best. So Cu, another face-centered cubic metal, has been considered[28-34]. Compared with Ni, Cu is non-ferromagnetic, has a high thermal and electric conductivity, and a low cost, but the disadvantages of Cu are a poor thermal-stability of texture, and a poor oxidizing resistance. Depositing a protecting layer on the Cu is a good way to overcome these disadvantages[35-37]. Another candidate is Ag[38-44]. Compared with Ni and Cu, Ag substrate does not need a buffer layer, YBCO layer can be deposited directly on Ag substrate [38-42] and oxygen can diffuse through sivel to oxidize YBCO at the right stoichiometry. However its low stacking fault energy making dynamic recrystallization easy during the rolling-annealing process is a great disadvantage to obtain a pure cube texture. Due to this characteristic of Ag, the texture of (110)<110> or (110)<112> is usually formed[43,44]. The Table 1.1 concludes all the review.

Polycrystalline metal can also constitute a substrate for coated conductors using the the IBAD or ISD technology to deposit a first buffer layer able to be a template for the grow of epitaxial YBCO layer[12, 45-49]. This broadens the field of usable metals; for example, stainless steel or hastelloy, can be chosen for substrate for coated conductors in IBAD or ISD routes. It is an advantage of IBAD and ISD routes that not only face-centered cubic metal or its alloy can be chosen for coated conductors[49].

Table 1.1 Properties comparison of metallic substrate

Substrate material	Comparing items								
	Mismatch (%)	texture	Thermo stability of texture	magnetic	Oxidization resistance	thermo extension coefficient	chemical compatibility	mechanical property	cost
Ni	-8.57	good	good	yes	good	13-17.4	worst	soft	medial
Cu	-6.10	good	bad	no	worst	17	worst	soft	low
Ag	6.10	normal	bad	no	good	18.9-25	better	soft	high

The choice of the best material for coated conductor is still an open question, it is complex since the substrate has several functions. However, some requirements muts be fulfilled like: sharp cube-texture, high mechanical strength and low magnetic moment.

1.3.1.2 Fabrication Technologies of Substrates for Coated Conductors

There are three main technologies to fabricate substrate for coated conductors: Rolling Assisted Biaxially Textured Substrates (RABiTS) process, Ion Beam Assisted Deposition (IBAD) process, and Inclined Substrate Deposition (ISD) process. Recent results show that the first two processes have attracted many researchers.

1.3.1.2.1 Rolling Assisted Biaxially Textured Substrates (RABiTS) process[13, 14, 19-34, 50-53]

After being cold worked and recrystallized by annealing, non-random orientations of grains are found in metals. This defines rolling texture or recrystallization texture respectively. Usually, a cube texture is obtained in a face-centered cubic metal with high stacking fault energy after being cold worked and submitted to a recrystallization process. That is the base of the RABiTS process. In comparison to other processes, RABiTS process shows a high efficiency and a low cost. Fig. 1.5 shows the schematic plan of RABiTS route. Because of these advantages, many research groups focus on this process[50-53]. Compared to IBAD process, the disadvantage of RABiTS process is that it applies only for face-centered cubic metal with high stacking fault energy while other metals can be used in IBAD process. In the beginning of coated conductor, Ni was chosen in RABiTS process, but Ni-W alloy is now preferred and other Ni-based alloys investigated. Besides Ni-W alloy, some interest has been raised for Cu[28-34].

1.3.1.2.2 Ion Beam Assisted Deposition (IBAD) process[12,45,49,54-56]

It has been proved in the results reported by Fujitsu company [12] that a textured buffer layer can be deposited on Hastelloy by Ion Beam Assisted Deposition (IBAD) process. In this process, the metal substrate is polycrystalline, and the texture is based on a textured seed layer. So, the substrate is a combination of a metal tape with a textured oxide layer. In the IBAD process, an ion beam assists the deposition of the oxide during the growth of the buffer films. Usually, the assisting ion beam is tilted form the substrate normal by an angle close to 55^{o}. The advantage of IBAD process is to apply to any metals like Ni-based alloy[12,54-55] and stainless steel[49]. It is very good to fulfill the requirements for substrate to have high mechanical properties and low magnetic properties. But IBAD has a low fabrication speed and needs a complex equipment. So, only the seed layer is fabricated by the IBAD process[46,57] while other layers are deposited by more economical methods. Fig. 1.6 shows the mechanism of IBAD process.

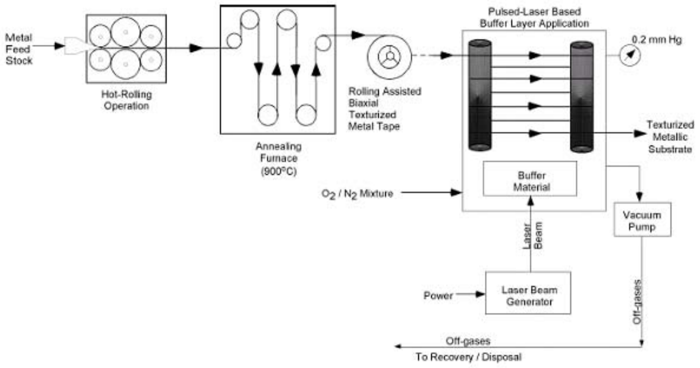

Fig. 1.5 a RABiTS route to fabricate coated conductors

(cited from www.ornl.gov/sci/htsc/documents/pdf/CCRoadmap8-23.PDF)

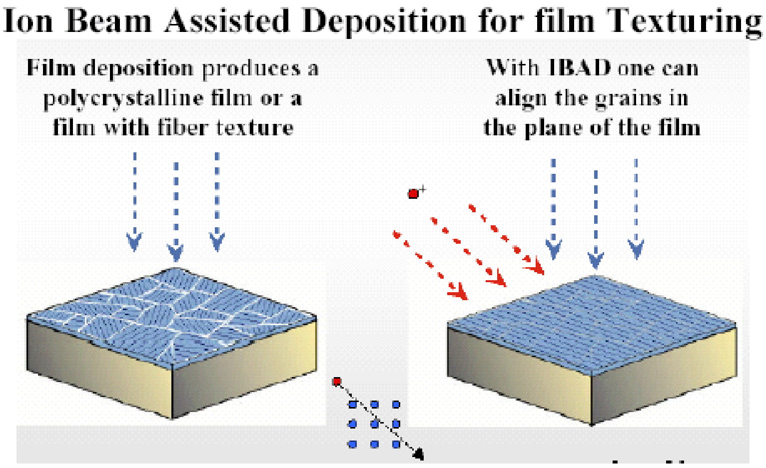

Fig. 1.6 IBAD process (cited from Las Alamos)

1.3.1.2.3 Inclined Substrate Deposition (ISD) process[47,48,58,59]

Similar to IBAD process, Inclined Substrate Deposition (ISD) process is a vacuum-based technology to texture an oxide layer on a polycrystalline metal substrate. In ISD process, a textured oxide layer is deposited by using an off-axis pulsed laser ablation without other assisting ion beam. The advantages and disadvantages of ISD process are similar to those of IBAD process. However the surface roughness of the oxide layer deposited by ISD is high. Fig. 1.7 shows the ISD process.

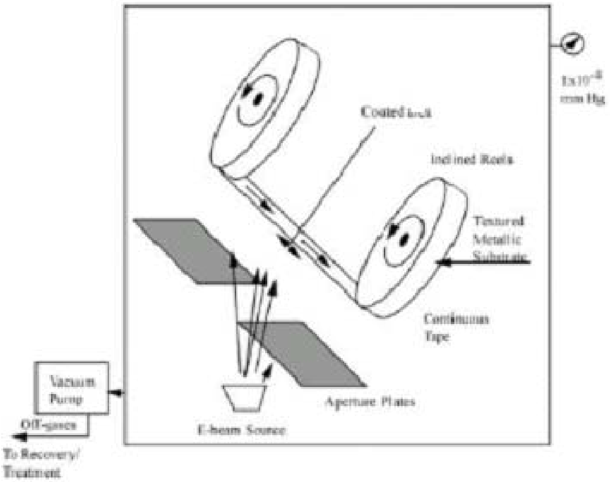

Fig. 1.7 ISD process

(cited from www.ornl.gov/sci/htsc/documents/pdf/CCRoadmap8-23.PDF)

1.3.1.3 Required Substrate's Characteristics

Based on the uses of the substrates, the first requirement for a substrate is to have a sharp cube texture. The texture is characterized by measurements using ω-scans were ω is the incident angle of the

X-rays, ϕ-scans where ϕ is the rotation angle around the normal to the sample, and tilts of the sample (χ) with respect the horizontal axis of the diffractometer. Usually, FWHM (Full Width at Half Maximum) value of ω scan and ϕ scan are used to quantify the sharpness. Because the texture is 3D, and ω and ϕ scans only show 1D information, then FWHM of ω and ϕ scans can not characterize all aspects of the texture's sharpness. For example, FWHM of ω scan of Ni substrate is different along the rolling direction and transversally to it, thus it depends of ϕ angle. So researchers in America proposed the concept of a "true in-plane texture"[60] which can be expressed by:

$$\Delta\Phi_{true} = \sqrt{\Delta\phi_{observed}^{2} - \tan^{3}\chi\left(\Delta\varpi_{\phi=0}^{2}\cos^{2}\phi - \Delta\varpi_{\phi=90}^{2}\sin^{2}\phi\right)}.$$

Where $\Delta\phi$ and $\Delta\omega$ are FWHM of ϕ-scans and ω-scans respectively. Besides this, there have been many questions about how to characterize the texture's sharpness, this is however beyond the scope of this work.

A second requirement is to have a strong mechanical strength and a low magnetic moment. A strong mechanical strength is required for tapes to support the stretches and the bending imposed during the cabling process. That is why the Ni-5at%W substrate is preferred over pure Ni. A low magnetic substrate is needed to decrease the AC losses resulting from the magnetic properties of the substrate.

Because the epitaxial growth will be used to form the buffer layer on the metallic substrate, the surface characteristics of substrates are important. References showed that a c(2×2)-S superstructure could be formed on the surface of Ni-based substrate[61-63], and this superstructure was needed to obtain a cube textured oxide layer on metallic substrate[64,65]. So the knowledge of the surface characteristics is important in order to obtain a good buffer layer on metallic substrates.

Besides surface characteristics, topological properties like grooves, grain boundaries and grains size of the substrates, would indirectly influence the superconducting properties of coated conductors. However, some results[66] show that thermal grooving in substrate influences slightly the Jc value of coated conductors, while grain boundaries and grain sizes will influence more the Jc value of coated conductors. From the viewpoint of epitaxial growth, the surface roughness of and cleanness of the substrate are also important, but a few results were reported on this apsect.

1.3.1.4 Brief Summary

Based on this review, the development of metallic substrate with low magnetic property, high mechanical property and sharp cube texture is the main effort of research in the field of coated conductors. A comparison of the processes RABiTS, IBAD and ISD shows that RABiTS is the process having the best chance to be used for economic metallic substrates.

1.3.2 Buffer Layer

1.3.2.1 Buffer Layer Materials

The functions of buffer layer require that its characteristics should be as follow: 1) small lattice mismatch with the substrate and with YBCO; 2) no chemical reaction with YBCO and with the substrate; 3) low diffusivity of metals and oxygen; 4) similar thermal expansion coefficient with that of YBCO. Usually, the buffer layer materials can be divided into, conductive buffer layers[67-69] and insulating buffer layers [46,51,52,70-79]. The Table 1.2[79] shows the characteristics of some highlighted buffer layers, and Fig. 1.8 shows the lattice thermal expansion of some oxide used as buffer layer and YBCO.

Table 1.2 Characteristics of highlighted buffer layers [79]

Materials	Crystal structure	Lattice parameter (Å) (pseudcubic)	Mismatch (%)		Diffusion coefficient of oxygen at 800℃ (cm^2/s)
			With YBCO	With Ni	
MgO	Rocksalt	4.21	9.35	-16.3	8×10^{-22}
CeO_2	Fluorite	3.83	-0.52	-7.99	6×10^{-9}
Y_2O_3	Mn_2O_3	3.75	-2.60	-6.03	6×10^{-10}
YSZ	Fluorite	3.63	-5.71	-2.92	2×10^{-8}
$SrTiO_3$	Peroyskite	3.91	1.56	-9.87	------
$La_2Zr_2O_7$	Pyrochlore	3.81	-1.04	-7.50	------
$Gd_2Zr_2O_7$	Pyrochlore	3.72	-3.38	-5.27	------

Note: The mismatch is defined by $M = \left(a_s - a_f\right)/a_f$, in which a_s is the lattice parameter of the substrate, and a_f is the lattice parameter of the film. a_{YBCO} = 3.85 Å in mean value.

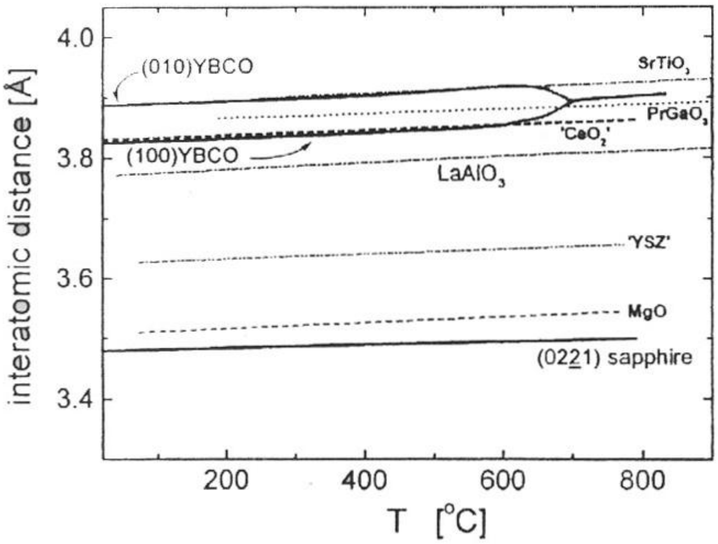

Fig. 1.8 The lattice change of some oxide and YBCO with changing temperature

Because the buffer layer should satisfy several functions, it is difficult to find an appropriate single material. The architecture of buffer layers is usually composed of two or three different oxide layers. For example, the buffer layer architecture of CYC [80] is composed of a CeO_2 layer, a Y-stabilized ZrO_2 layer and a CeO_2 cap layer. Due to different chemical and physical properties, a combination of multi-technologies is necessitated to fabricate the buffer layers. The fabrication process of the buffer layers is complex, hard and expensive. So simplifying the buffer layer architecture become an important issue. According to this viewpoint CeO2/$RE_2Zr_2O_7$ (RE=La, Gd) [46,52,75,81,82] and $SrTiO_3$ [67,68,69,73] buffer layers become very attractives.

1.3.2.2 Fabricating Technologies of Buffer Layer

All the technologies[83] which have been used to fabricate an oxide layer on a substrate can be used to fabricate the buffer layer. But only some of these are discussed in this section. They can be divided into two main classes: vacuum deposition and chemical solution deposition (CSD).

1.3.2.2.1 Pulsed Laser Deposition process

The pulsed laser deposition (PLD) process is a typical vacuum deposition approach. Many high Tc superconducting film has been fabricated successfully since 1987[82,84-87], and it has become one of the best method to fabricate superconducting film. In PLD process, the target is ablated by a pulsed laser to form a plasma from which ionic species are deposited on a hot substrate. Because of the high energy of the pulsed laser, all the components in target can be ablated and deposited simultaneously on the substrate. This is very suitable for depositing a complex buffer layer material. At the same time, different targets can be used during the deposition process in order to obtain multi-layers. Fig. 1.9 shows a schematic figure of PLD system.

The disadvantages of PLD process are that it is difficult to fabricate long samples; the cost is high and processing speed slow. So researchers in Japan developed a multi-deposition system to avoid these disadvantages[84].

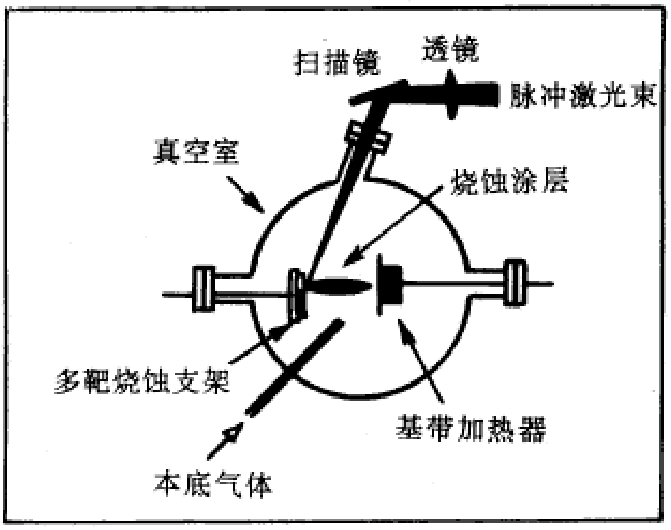

Fig. 1.9 Schematic diagram of PLD system

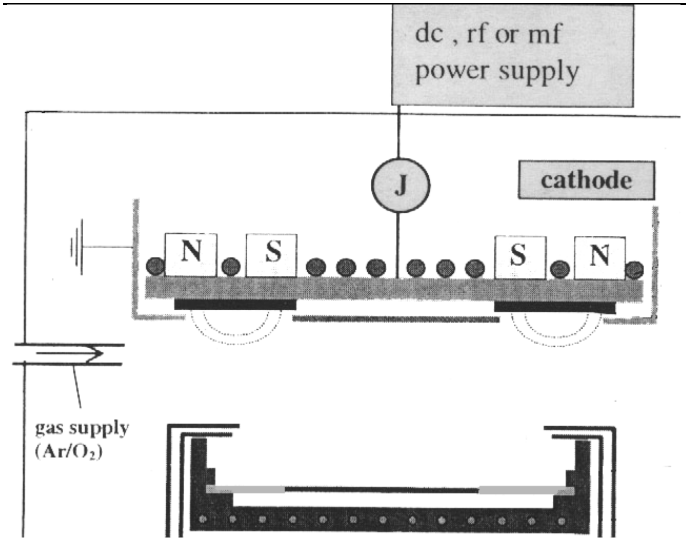

Fig. 1.10 Schematic diagram of sputtering process

1.3.2.2.2 Sputtering Deposition[51,53,88]

Sputtering deposition is another vacuum deposition approach in which an inert gas is introduced into a vacuum chamber and ionized. The ions bombard the target which is sputtered on the substrate and form the film. In order to increase the sputtering efficiency, a magnetic field is usually applied at the cathode; this technology is also called the magnetron sputtering deposition. The magnetron sputtering can be divided into two classes: direct current sputtering and radio frequency sputtering. Comparing with direct current sputtering, the radio frequency sputtering process does not need a conductive target, so it is often used to fabricate buffer layers of insulating compounds. Fig. 1.10 shows the schematic diagram of sputtering process.

1.3.2.2.3 Chemical Solution Deposition (CSD) Processes

An ultrahigh vacuum device is necessary for vacuum deposition. So it is not appropriate for fabricating economic coated conductors. At the same time, vacuum deposition approaches need complex equipments, and fabricating speed is slow.

Contrasting with vacuum deposition, chemical solution deposition (CSD) processes are economical and easy methods to fabricate buffer layers. No complex equipments are needed and deposition speed is fast and can be real-to-real. Besides this, a characteristic of CSD processes is that it is easy to control the composition of the film by adjusting the stoichioemtry in the precursor solution. So more and more research are being focused on the CSD process[52,70,75,89-92].

The fabrication of a buffer layer by CSD processes includes four basic steps: to prepare a precursor solution, to cover the substrate by spin-coating or dip coating method, to pyrolyze and to crystallize the precursor film. Usually, the last two steps occur in same time. Based on the chemical properties of the precursor solution, the CSD processes can be divided into three classes[93,94]: Sol-gel process, Metal-organic decomposition (MOD) process and Hybrid routes. The alkoxide precursors are used in Sol-gel process, carboxylates or β-diketonates are used in MOD and combined ligands are used in Hybrid routes.

Whatever the precursors are, the preparation of the precursor solution is a key for CSD processes and the parameters of the process are very sensitive to the properties of the precursor solution. The required characteristics of the precursor solution are: i) sufficient long-term stability; ii) no macroscopic phase separation during drying or pyrolysis; iii) acceptable wetting of the substrate; iv) no reaction with the substrate. If the precursor solution with good properties can be prepared successfully, the next step would be to optimize deposition and the heat-treatment of the precursor film.

Several disadvantages of CSD processes must be however recalled: depositing thick films in one step is not easy without crack formation in the precursor film[95]; surface crystallinity and texture of film fabricated by CSD processes must be perfect if the film is used to fabricate the buffer layer[96]. However, results reported by many labs show that CSD process is a potential method to obtain coated conductors with high Jc value. ORNL has obtained several records on YBCO coated conductor with high superconducting properties[81].

1.3.2.2.4 Other Deposition Processes

1.3.2.2.4.1 Metal Organic Chemical Vapor Deposition[71]

Metal organic chemical vapor deposition (MOCVD) uses metal organic materials with high vapor pressure as sources, its vapors obtained at moderate pressure (~ 5 Torr) are carried into a reaction chamber by an inert gas. A film is obtained by reaction of the different vapor of metal organic materials on the substrate. A high vacuum is not necessary and it is possible to fabricate long tapes in a continuous process. However it is difficult to stabilize the injection of the vapor which will influence the uniformity of the tape[97]. Fig.1.11 is a schematic diagram of MOCVD system.

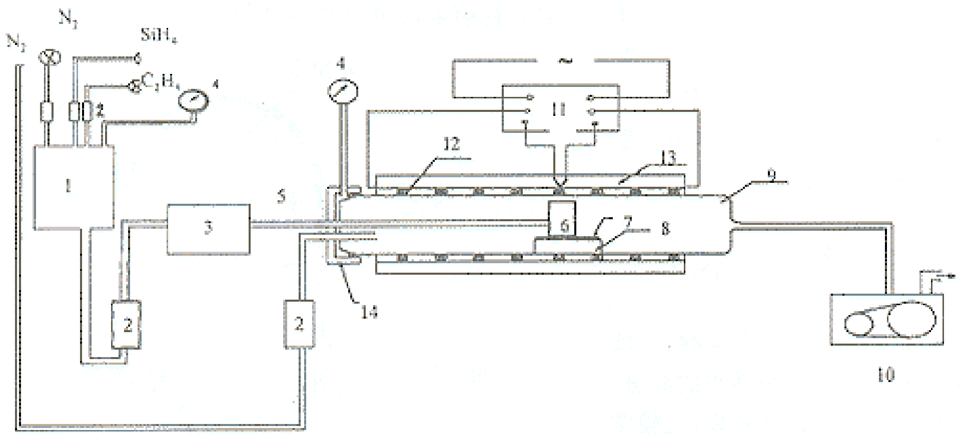

Fig. 1.11 A schematic diagram of MOCVD system

1: mixed gas chamber; 2: flow meter; 3: motor; 4: manometer; 5: stainless steel pipe; 6: injection head; 7: sample; 8: sample holder; 9: reaction chamber; 10: vacuum pump; 11: temperature controller; 12: heater; 13: adiabatic material; 14: airtight seal

1.3.2.2.4.2 Surface Oxidation Epitaxy Process[77,98,99]

Surface Oxidation Epitaxy (SOE) process [98] has been reported by ISTEC for the fabrication of a buffer layer in 1999. In this process, the Ni substrate is heated at a high temperature (1000~1300°C) under oxygen or air atmosphere, forming a cube textured NiO layer on the surface of substrate. The NiO layer can be used as a seed layer for growing another oxide layer deposited on it. It is difficult to grow uniform cube textured NiO on a long tape without grain boundaries where Ni diffuses fast. Only a few groups continue to study it.

1.3.2.2 Brief Summary

Although the properties of coated conductors fabricated by vacuum deposition processes are better than those obtained by chemical solution deposition processes, the chemical solution deposition still have some strong potentialities due to their economic, continuous and easily scaleable features. CSD are potential methods to fabricate low cost coated conductors with good properties.

1.3.3 YBCO Layer

Except the SOE process, almost all the technologies which were mentioned previously can be used to deposit YBCO layer. Three main processes are used to deposit the YBCO layer: Metal Organic Decomposition (MOD) process[88, 100 -105], Metal Organic Chemical Vapor Deposition (MOCVD) process[97, 106, 107,108] and Physical Vapor Deposition (PVD) process[46, 109-112]. Among these technologies, metal-organic deposition using trifluoroacetates (TFA-MOD) process, is considered as the best candidate for fabricating YBCO layer at atmospheric pressure.

1.3.3.1 TFA-MOD process

The obstacle of fabricating YBCO layer by normal MOD process is $BaCO_3$ that always forms during normal MOD process. Because the thermal stability of $BaCO_3$ is very large, $BaCO_3$ will impede to reach high superconducting properties of YBCO layer. However, using trifluoroacetates, BaF_2, instead of $BaCO_3$, is formed during pyrolysis of precursor film. BaF_2 can be decomposed easily under humid gas. So this process using trifluoroacetates can overcome the obstacle which the normal MOD always meets. This process is called the TFA-MOD process[100]. The up-to-date result[118] shows very high superconducting performances with YBCO layer reaching 735 A/cm at 77 K.

In the TFA-MOD process[101] a stoichiometric mixture acetates is dissolved into trifluoroacetic acid, and the solution is refined under decompression to obtain a blue gel with impurities. The blue gel is dissolved into methanol, and the solution is refined under decompression again to remove the impurities. This refining process is repeated several times to obtain a pure precursor solution. The precursor solution is deposited on the substrate and the sample is heated to obtain YBCO layer. The heat treatment is divided in two steps, showed in Fig. 1.12. From Fig. 1.12, it can be seen that the process is very long. So a modified TFA-MOD was reported [102] with a shorter schedule. High Ic values were obtained successfully by this modified TFA-MOD process with a short heat-treatment process[102].

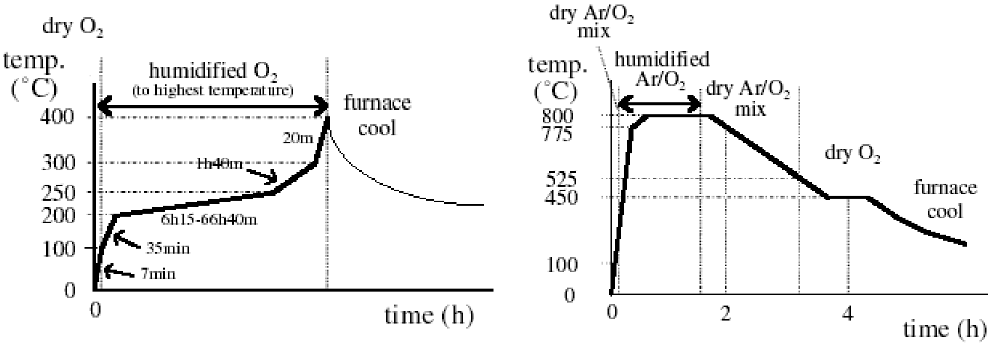

Fig. 1.12 The schematic heat-treatment of TFA-MOD process[101]

1.3.3.2 Brief Summary

Besides the Pulsed Laser Deposition process, MOCVD process and MOD process, there are still other alternatives to fabricate YBCO layer, like Pulsed Electron Deposition process[112], Liquid Phase Epitaxy process[115], BaF_2 ex-situ process[113, 114,116] and Spray pyrolysis process[41,117]. However, researchers prefer the TFA-MOD process, MOCVD process and PLD process.

1.4 Summary

Due to good superconducting properties under high magnetic field, YBCO coated conductor attracted many researchers efforts. Most attentions on materials are focused on the fabrication of metallic substrate, buffer layer and YBCO layer. Most researchers think that the TFA-MOD process is a potential method to fabricate YBCO layer, but there are still a lot debates concerning the best choice for the metallic substrate, the architecture of the buffer layers and the method for its deposition. However a clear agreement concerns the metallic substrate that should have a sharp cube texture and low magnetic property. Many researchers also agree that the chemical solution deposition is a potential way to fabricate economic coated conductors with good superconducting properties.

Chapter II Fabrication of Cube Textured Cu Substrate

2.1 Introduction

Due to good lattice matching with YBCO, easy fabrication and good thermal stability of its cube texture, Ni was the first metal to be selected for substrate material of coated conductors. But Ni is soft and ferromagnetic, this is a strong handicap for handling long tapes and for magnetic losses in cables carrying AC current. In order to decrease their magnetic properties, several Ni-based alloys were developed[19-27]. Alloying not only decrease the Curie temperature, but also improve the substrate's mechanical strength. Although alloying can decrease the magnetic property of Ni-based substrate, the non-magnetic metallic substrate is the best choice in the perspective of cable applications. This is why several researchers[28-34] have attempted to use Cu substrate .

Cu is a face centered cubic metal like Ni; Cu tapes can be fabricated cube-textured by the rolling-recrystallization process. At the same time, the mismatch of Cu with YBCO is only 5.4 % with the a-axis and 7.1 % with the b-axis. Based on these viewpoints, Cu is an important alternative to nickel based substrates. Besides these, Cu has other advantages, for example, it is cheaper, it has a high thermal conductivity and a low electrical resistance. But the disadvantages of Cu substrate are obvious, the thermal stability of the cube texture and the oxidation resistance of Cu tapes are poor. These weaknesses can be overcome by depositing buffer layers with a special architecture[31,33] or adding a protecting metal layer[35-37] like a Ni layer. This chapter is focused on the fabrication of cube textured Cu tapes. How to protect the Cu substrate will be studied in next the chapter.

2.2 Experiments

2.2.1 Preparation of samples

A Cu plate, whose purity was larger than 99.7%, was used as raw material. It was divided in several pieces of different thicknesses: 2.6mm, 4.3mm, and 14mm, respectively. Before rolling, each piece was polished mechanically. The samples were rolled uni-directionally to a final thickness of 0.18mm. The total rolling deformation rates was 93%, 95.8% and 98.7%, respectively. After rolling, all the samples were heat treated under vacuum (total pressure lower than 10^{-2}Pa), and annealed at 600°C with a heating rate of 1200°C/h.

In order to compare the influence of cold working on the texture of the substrate, Cu rods were also investigated. A copper rod was extruded from an ingot and drawn to reach the diameters of 3.8mm or 10mm respectively, then rolled uni-directionally to reach a final thickness of 0.19mm. In this experiment, the rolling direction was reversed at each end of the sample until the final thickness was reached. All samples were annealed at 600°C for 1 hour under vacuum. Based on the engineering viewpoint, the reversed rolling process is better controlled than the unidirectional rolling. In order to compare these two processes, some Cu rods were chosen to test the influence of changing the rolling direction..

The influence of the recrystallization was also investigated. For this, Cu tapes rolled from the largest

Cu rods (diameter of 10mm) were annealed at different temperatures during different times.

In order to decrease the roughness of the Cu substrates, their surfaces were electro-polished with an electrolyte containing a high concentration, of H_3PO_4.

2.2.2 Data treatments

Texture, or preferred orientation of crystallites, is an intrinsic feature of materials that influences several of their physical properties. Texture means that the crystallographic orientations are not random. Textures are quantified by the Orientation Distribution Function (ODF) which is defined as:

$$\frac{dV}{V} = f(g)dg$$

where:

f(g) – is the ODF;

g – is the orientation wit respect to the sample's referential;

dV –is the volume of the crystallites having the orientation g in the element of space orientation dg;

V – is the sample's volume. The ODF can not be obtained directly, ODF calculation is usually calculated from several pole figures by an appropriate algorithm now included in the software of LaboTex.

The characteristics of a texture can be described by its sharpness and volume fraction. Usually, the sharpness of a texture can be quantified by the Full Width at Half Maximum (FWHM) of ω and ϕ scans. These two terms refers respectively to out-of-plane component of the texture (ω scan) and the in-plane texture component of the texture (ϕ scan). The volume fraction can be obtained directly from ODF calculation.

In this chapter, all textures were checked by X-ray diffraction (Cu Kα) with a four circles goniometer (Seifert MZ IV equipped with Xenocs multilayer optics, the incident x-ray beam has a horizontal divergence of 0.06°) to measure pole figures, ω and ϕ scans. Considering that the sample's texture is not uniform in Euler space, the ω scan were done under conditions where the ϕ angle was 0^{o}, 90^{o} or varied (72^{o}/s), which corresponds respectively to measurements performed along the transverse direction, along the rolling direction and for an average of both.

The values of FWHM of ω and ϕ scans were obtained by fitting the curves using Gaussian functions (considering the large FWHM of our samples, using other functions more appropriate for x-ray diffraction will have marginal effect on the results) with the software Origin. Raw data were used to plot the pole figures using the software IgorPro, there were no defocusing corrections made in these plots. The Orientation Distribution Function (ODF) was calculated using the software LaboTex after taking into account the defocusing corrections calculated from a pole figure of a Cu powder free of texture.

2.3 Results and Discussions

2.3.1 Rolling process

The fabrication process of cube textured Cu substrate can be divided in two main steps: rolling and recrystallization. Several parameters of the process influence the final texture of Cu tapes. The influences of rolling process will be discussed first in this part

2.3.1.1 Influence of rolling deformation rate on the formation of the cube texture

A: Cu plates

The texture of recrystallization is influenced by the texture of the raw material[121], so as received Cu plates were studied first. Fig. 2.1 shows the pole figure of a typical raw Cu plate. It is clear that there is no special orientation. Fig. 2.2a-to 2.2c show the (111) pole figures of Cu tapes submitted to different deformation rates: 93%, 95.8%, 98.7%, respectively. Usually, the rolling texture of high stacking fault energy FCC metals is as shown on Fig. 2.3[124], where the dominant texture components are S component ({123}<634>) and C component ({112}<111>). A comparison of Fig. 2.2 with Fig. 2.3 shows that the texture of Cu tapes is similar to that of high stacking fault energy FCC metals, but with a small additional shear texture component[122,123], the amount of which increases with the rolling deformation rate. The influence of the shear texture contribution will be discussed later.

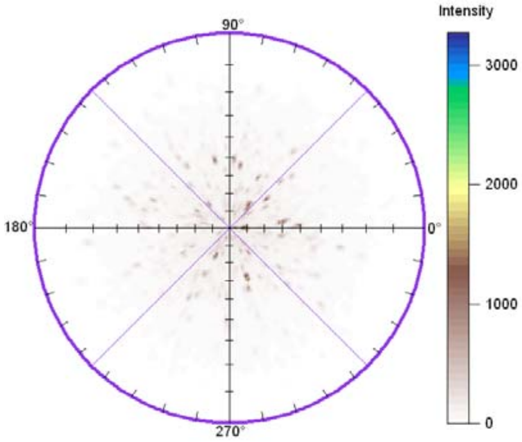

Fig. 2.1 The texture of raw Cu plates

The texture after annealing at 600°C for 1 h is shown in Fig. 2.4. A comparison of Fig 2.4a, Fig 2.4b and Fig 2.4c shows that the cube texture can be found only in sample which was rolled with a deformation rate of 98.7%. Annealing at 600°C of samples deformed only at 95.8% does not provide the cube texture. In order to know if this is due to the heat treatment, these samples were annealed at 300°C or 700°C for 2 hours, and then their texture were compared. It is clear from Fig.2.5 that the cube texture can not be found in both samples showing that 700°C is not sufficient to crystallize the cube texture for this low deformation rate. Combining Fig 2.4 and Fig 2.5 shows that the rolling process is a key to obtain cube textured Cu tapes. Only sufficiently large deformation rate is able to induce cube texture after recrystallization. The deformation rate must be larger than a critical value as suggested before in ref. [29]. In our case, the critical value is larger than 95.8 %, while it was found equal to 83 % in ref. [29]. Ref. [28] also studied the influence of the rolling process on the texture of Cu tapes made from a raw Cu plate. These authors were unable to reach the cube texture. We think that the difference between these experiments is due to differences in the thermal/mechanical process applied. The Cu plate treated in ref. [28] was submitted to a series of deformation and heat treatments, because the recrystallization temperature of Cu is very low (~150°C), the texture of the starting Cu plate was not random. Based on the above-mentioned analysis, we can conclude that the final annealing texture of Cu is very sensitive to the rolling-annealing process.

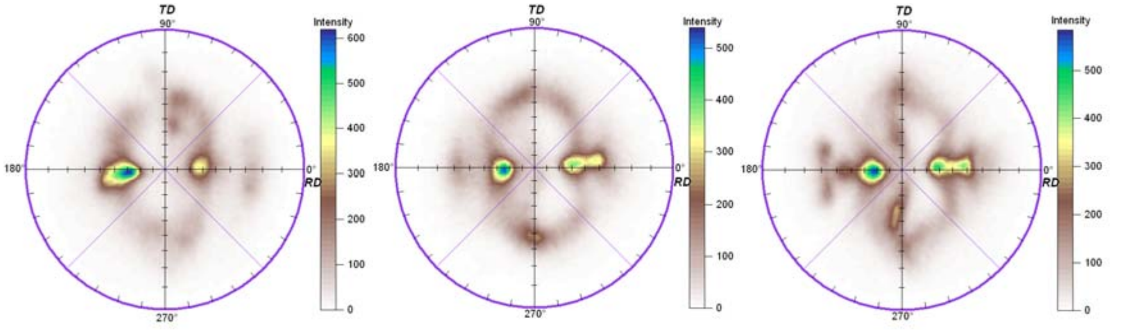

2.2a 2.2b 2.2c

Fig 2.2 (111) pole figures of Cu tapes after rolling at different deformation rate

2.2a: 93%; 2.2b: 95.8%; 2.2c: 98.7%

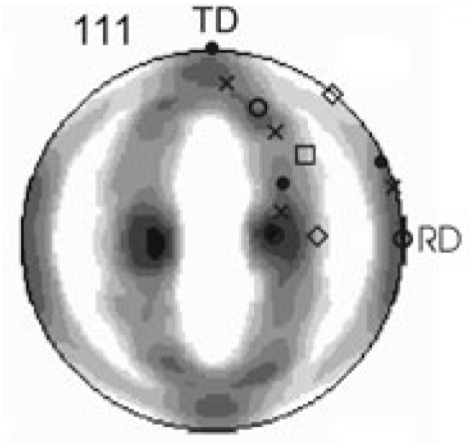

Fig. 2.3 (111) pole figure of Cu rolled[124]

Texture components: × S component; O C component; • B component; ◊ G component; □ cube texture

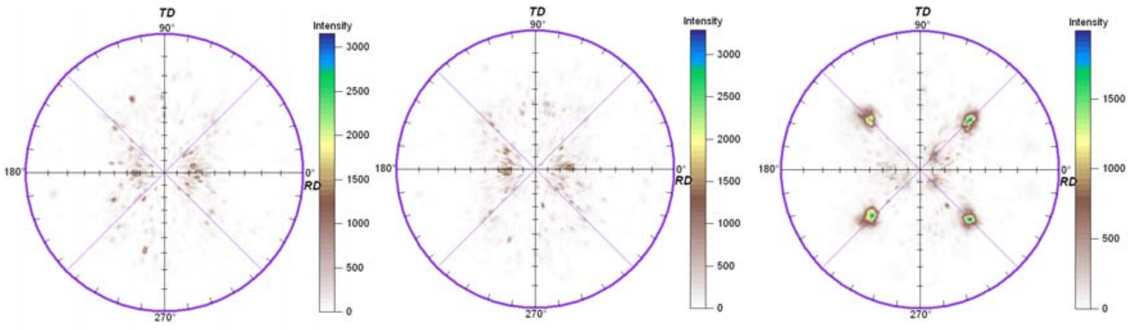

2.4a 2.4b 2.4c

Fig. 2.4 Influence of the rolling deformation rate on the recrystallization texture of Cu tapes. 2.4a 93%; 2.4b: 95.8%; 2.4c: 98.7%

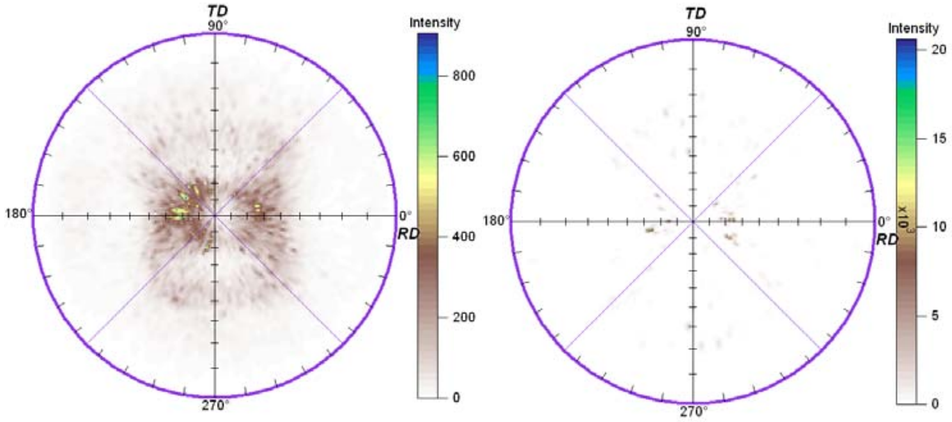

2.5a 2.5b

Fig. 2.5 Influence of annealing temperature on the recrystallization texture of Cu tapes with a rolling deformation rate of 95.8%. 2.5a: 300°C; 2.5b: 700°C.

B: Cu rods

In order to know more on how is influenced the formation of cube texture by the deformation rate, Cu rods with different diameter ($\phi = 3.8$ mm and $\phi = 10$ mm) were studied. They were submitted to the same process as described previously. The sample's textures are shown in Fig. 2.6, where the raw diameter of the samples are $\phi = 3.8$mm in Fig. 2.6a, and $\phi = 10$mm Fig. 2.6b respectively. These figures show that the cube texture can be obtained only if the Cu rod were heavily deformed. These results stress that a heavy rolling deformation is a key to obtain cube textured Cu tapes.

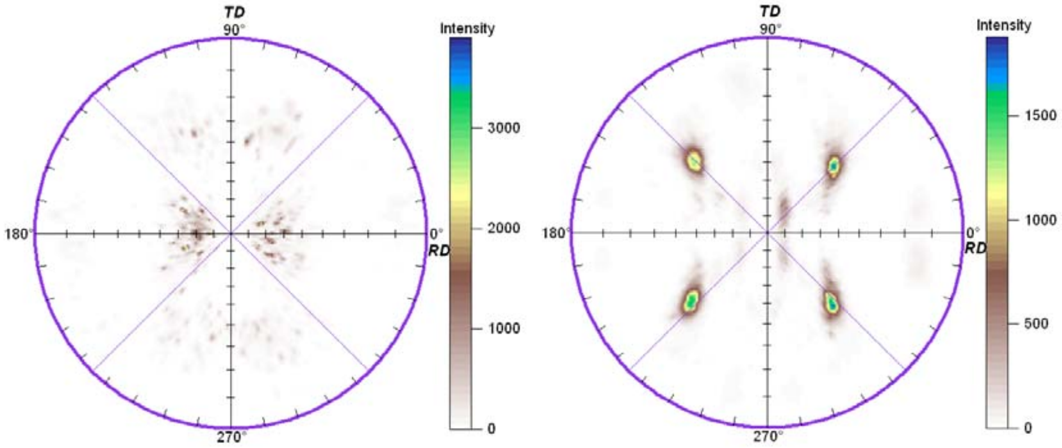

2.6a 2.6b

Fig. 2.6 Influence of the rolling deformation on the texture of Cu tapes. Raw material is a rod rolled to a final thickness of 0.19 mm.

2.6a initial diameter $\phi = 3.8$mm; 2.6b initial diameter $\phi = 10$mm

2.3.1.2 Effect of surface deformation during rolling process

Friction between roller and sample results in a non uniform texture across the sample thickness. This is linked to the roller gap geometry which is defined by the ratio l/h, where l is the projected length of contact between roller and sample, and h is the mean thickness of sample. Friction causes shear stress in the surface layer resulting in shear texture. Shear texture must be distinguished from non uniformity in the texture caused by the roller gap. Fig.2.7 shows a typical shear texture. Compared to rolled texture, the characteristic of a shear texture is in the position of the diffraction spot which shifts from χ=25º to 52º in the RD direction while the contribution is broadened along the TD. After removing the top layer of the sample in Fig. 2.2c (0.001 mm), the (111) pole figure was measured again. The result shows a typical rolling texture of high stacking energy FCC metal (Fig. 2.8b). The calculation of l/h shows that the value of the roller gap increases with decreasing thickness of sample for constant thickness reduction per pass, and the value of l/h is larger than 5 if the thickness of the sample is smaller than 0.74 mm. Under this condition, a shear texture occurs easily in the surface layer[122]. At the same time, the amount of shear texture becomes large with increasing the rolling deformation rate. This is well evidenced in Fig. 2.2.

Besides the rolling deformation rate, the thickness reduction per pass also influences the amount of shear texture. Fig. 2.9 shows this influence, in which the thickness reduction per pass of sample in Fig. 2.9a is 10 %, and 30 % in Fig. 2.9b. It is clear that the larger the thickness reduction per pass, the larger the shear texture contribution is. This is due to the increase of friction when the thickness reduction per pass is increased, this is quantified by l/h increasing from 5.3 for a reduction rate of 10 % to 8.5 when the reduction rate is 30 %.

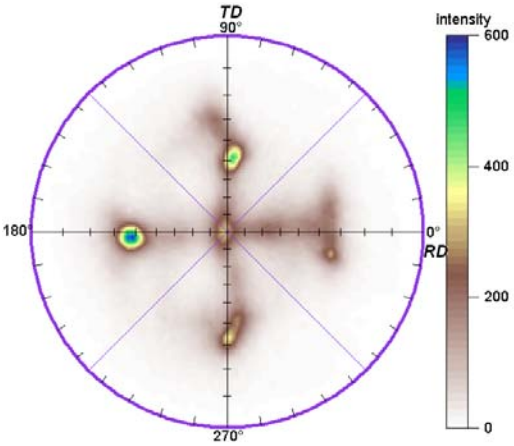

Fig. 2.7 (111) pole figure of sample with a strong shear texture

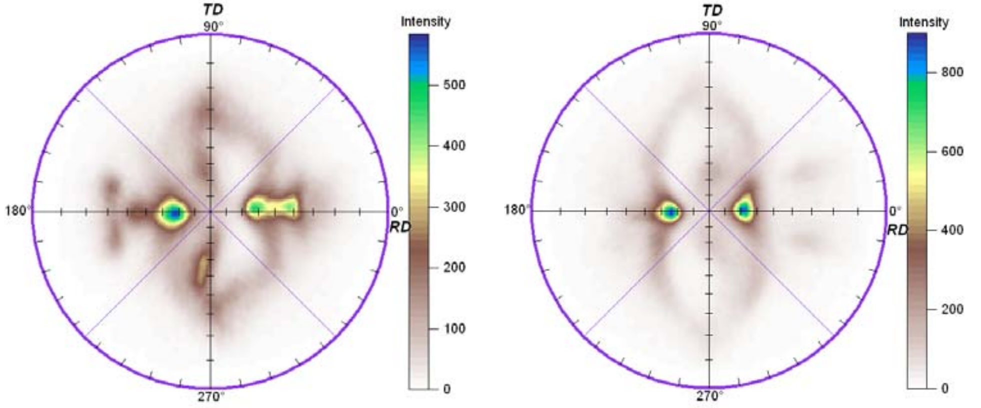

2.8a (Figure 2.2c) 2.8b

Fig. 2.8 Comparison of (111) pole figures of sample in figure 2.2 before and after removing 0.001mm of the top layer. 2.8a: before; 2.8b: after

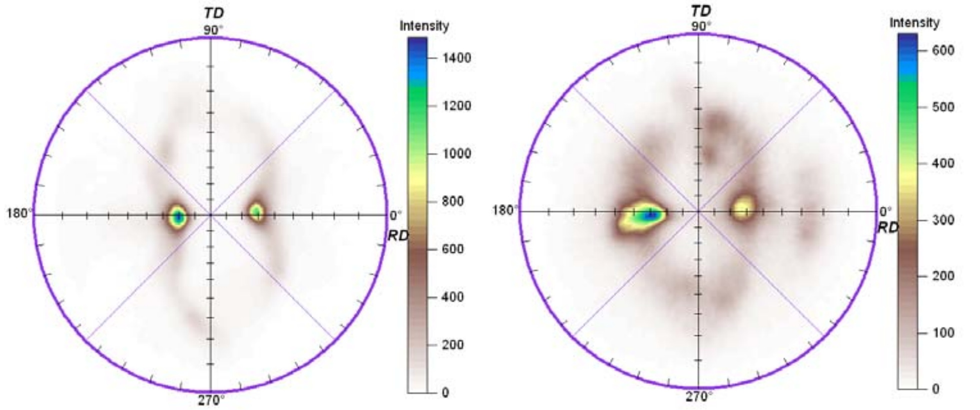

2.9a 2.9b

Fig. 2.9 Role of thickness reduction per pass. (111) pole figures of samples rolled with a deformation rate of 93%. 2.9a: the thickness reduction per pass is 10 %; 2.9b: the thickness reduction per pass is 30 %

Based on the results of Fig. 2.4, it is qualitatively clear that the formation of cube texture is not influenced by the occurrence of shear texture if the rolling deformation rate is large enough. But a shear texture will contribute to decrease the volume fraction of cube texture; this is the case in the sample of Fig.2.4b. Besides this influence, the shear texture also influences the annealing procedure to obtain a cube texture. The Fig. 2.10 compares θ-2θ scans of two samples recrystallised at 800°C for half hour, the sample on the top was exempt of shear texture while the sample at bottom had a shear texture. It is clear that a cube texture is only found in the sample without shear texture.

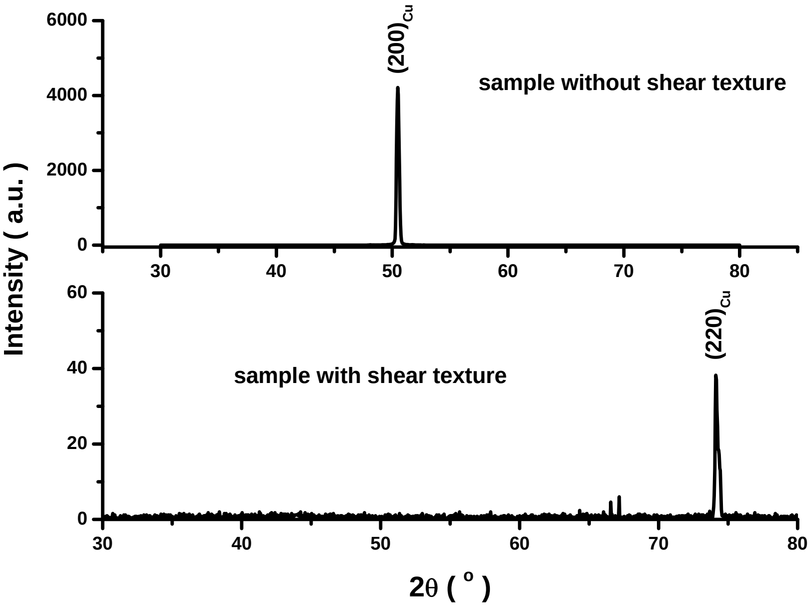

Fig. 2.10 Influence of shear texture on the formation of cube texture. Both samples were annealed at 800°C for half hour.

2.3.1.3 Influence of thickness reduction per pass on the sharpness of cube texture

Rolling and recrystallization textures have been investigated for many years but very few concerned the influence of thickness reduction per pass on the sharpness of cube texture. So we investigate this influence in this section.

The shear texture can be always found after Cu plates were heavily rolled even for small thickness reduction per pass, i.e. 10 %. It means that the texture of deformation of Cu plates is inhomogeneous at a macroscopic scale. In order to eliminate this influence we investigated the rolling process of Cu rods was.

A Cu rode with a diameter of $\phi = 10$ mm was rolled with a thickness reduction per pass of 10% or 30%. The Fig. 2.11 shows the (111) pole figures of both rolled samples. It is clear that the patterns of Fig. 2.11 are similar with the one of Fig. 2.3 (ref.[124]) with S component and C component being the major texture components of the texture.

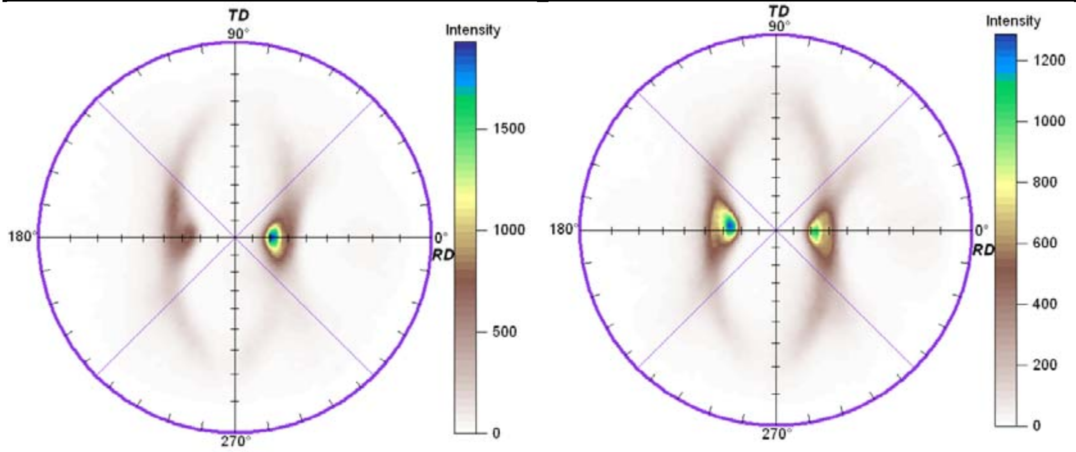

2.11a 2.11b

Fig. 2.11 Influence of thickness reduction per pass on the rolling texture. 2.11a: thickness reduction per pass of 10%; 2.11b: thickness reduction per pass of 30%

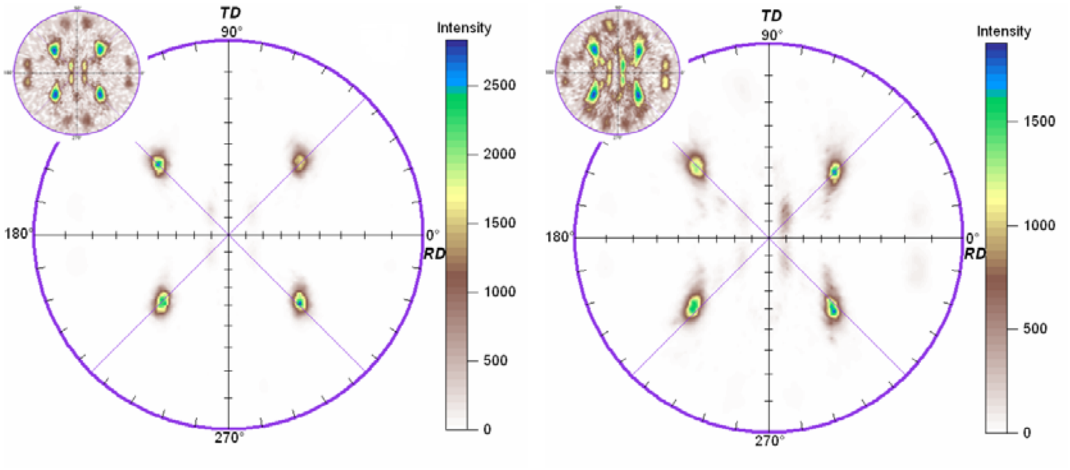

2.12a 2.12b

Fig. 2.12 (111) pole figures of recrystallized samples rolled under a different thickness reduction per pass. 2.12a: thickness reduction per pass of 10%,. 2.12b: thickness reduction per pass of 30%. In both cases, the insert shows the pole figure represented with a log scale for z axis.

The samples were annealed at 600°C for 1 hour and their (111) pole figures are shown in Fig. 2.12. Fig. 2.12a shows a sample rolled under a low thickness reduction per pass (10 %) and compared in Fig. 2.12b with a sample rolled with a high thickness reduction per pass (30 %). These figures are similar at first sight. However there is more twinning components of cube texture when the reduction per pass is larger, Fig .2.12b. Twinning is evidenced by diffracted intensities visible at $\phi = 45°$ (and equivalent positions) and $\chi=15.8^o$. Moreover, in addition to cube texture and twinning components, some extra component arises for large thickness reduction per pass (see insert of Fig. 2.12).

The table 2.1 lists the full with at half maximum (FWHM) for ω and ϕ scans. These data show that the thickness reduction per pass does not influence very much the sharpness of the in-plane texture (ϕ scan), but has a significant influence on the sharpness of out-of-plane texture (ω scan), especially for $\phi = 0^o$.

Table 2.1 Influence of thickness reduction per pass on the sharpness of cube texture of Cu tape

Thickness reduction per pass	FWHM value of ω scan (^{o})			FWHM value of ϕ scan (^{o})
	$\phi = 0^{o}$	$\phi = 90^{o}$	ϕ = rotation	
10%	7.9	4.5	6.3	7.0
30%	9.2	3.1	9.1	7.5

Note: "rotation"means that the sample rotates around the ϕ axis (72^{o}/s)

Because FWHM for in-plane texture represents the spread of the orientation distribution of <200> direction, it is observed that large reduction per pass affects more the transverse direction ($\phi = 0$) than the rolling direction. We think that this phenomenon is related to the friction between the roller and the sample. During the rolling, the sample expand at each rolling pass. The friction along the transverse direction is increased and this amplified by increasing the reduction per pass. It results in a decrease of the texture sharpness along the transverse direction.

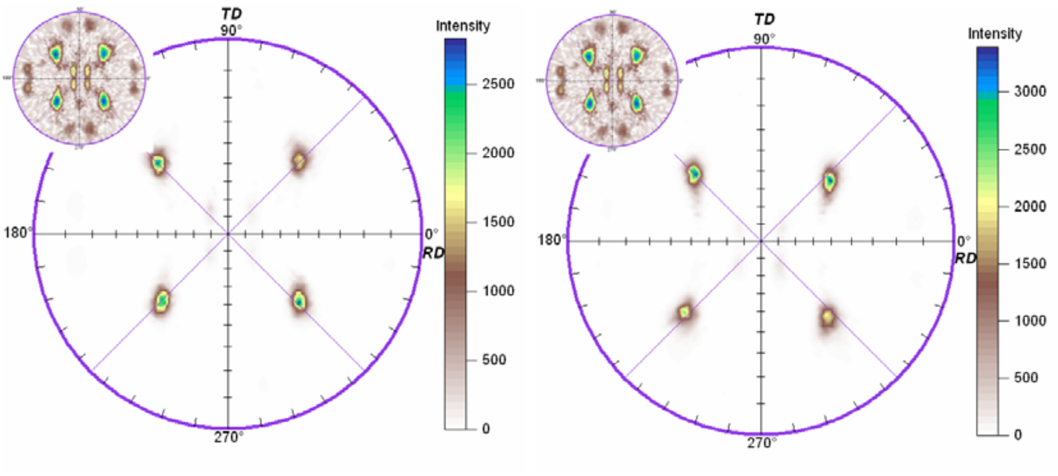

2.13a 2.13b

Fig. 2.13 (111) pole figures of two samples submitted to different rolling process. 2.13a unidirectional rolling. 2.13b reversed rolling. In both cases, the insert shows the pole figure represented with a log scale for z axis.

2.3.1.4 Influence of the rolling direction on the sharpness of cube texture

The unidirectional rolling is the best way to obtain cube textured Ni substrate. But it is necessary in practice to change two times the roller gap at each pass. This is complex and makes the control of the rolling process difficult. So the reversed rolling is more convenient and we investigated it.

Fig. 2.13 and Table 2.2 show the influence the two procedures on a Cu rods with diameter of ϕ = 10 mm rolled to a final thickness of 0.19 mm with a thickness reduction per pass of 10%, and recrystallized. The results show that changing the rolling direction during the rolling process does not influence the formation of the cube texture, but influences hardly its sharpness. Changing the rolling direction is benefiting for obtaining easily cube textured Cu substrates.

Table 2.2 Influence of rolling direction on the sharpness of cube texture of Cu tape

Rolling direction	FWHM value of ω scan (°)			FWHM value of ϕ scan (°)
	$\phi = 0^o$	$\phi = 90^o$	ϕ = rotation	
Unidirectional rolling	7.9	4.5	6.3	7.0
Reversed rolling	8.7	3.4	6.2	6.5

Note: "rotation"means that the sample rotates around the ϕ axis (72 ^{o}/s)

2.3.2 Recrystallization heat treatment

The influences of rolling parameters on formation and sharpness of cube textures were studied in the last section. In this section, the influences of recrystallization on the sharpness of cube texture will be discussed.

2.3.2.1 Influence of pre-annealing on the texture of Cu substrate

Usually some pre-annealing treatments are made during the cold working performed to process Cu tapes. In order to study the influence of pre-annealing on the sharpness of the cube texture, Cu rods with diameter $\phi = 10$ mm were pre-annealed at 400°C, and then rolled and recrystallized. Typical (111) pole figures of these samples are shown in Fig. 2.14. When a pre-annealing at 400°C is made before rolling, the texture is composed of rolling texture plus cube texture plus twinning, Fig.2.14a. Clearly the cube texture has been formed before the recrystallization treatment. The recrystallisation treatment, makes the rolling texture to disappear but still some twinning remain. Combination the results in Fig. 2.14 and one in Fig. 2.6 shows the rolling deformation rate before the final recrystallization is very important for formation of cube texture, the pre-annealing process does not influence the formation of cube texture if the rolling deformation rate before the final recrystallization is larger a critical rate.

Although, the pre-annealing process does not impede the cube texture formation, it influences the sharpness of cube texture. All the results have listed in Table 2.3. It is surprising that the FWHM value of ω scan is very large if the measurement condition is that the sample rotates about the ϕ axis. There is no reasonable explanation to explain this result, and more analysis should be done in future.

Table 2.3 Influence of pre-annealing before rolling on the sharpness of cube texture of Cu tape

Pre-annealing	FWHM value of ω scan (°)			FWHM value of ϕ scan (°)
	$\phi = 0^o$	$\phi = 90^o$	ϕ = rotation	
Yes	6.8	4.3	9.9	6.4
No	7.9	4.5	6.3	7.0

Note: "rotation"means that the sample rotates around the ϕ axis (72 ^{o}/s)

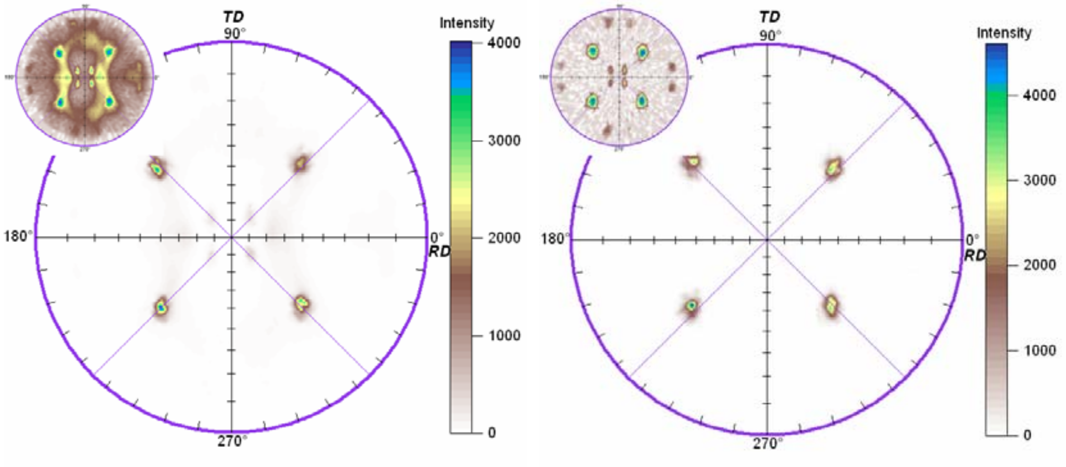

2.14a 2.14b

Fig. 2.14 Influence of a pre-annealing at 400°C before rolling on the formation of cube texture. 2.14a: rolling texture. 2.14b: annealed texture. In both cases, the insert shows the pole figure represented with a log scale for z axis.

2.3.2.2 Influence of annealing temperature on the formation of and sharpness of cube texture

Fig. 2.15 shows the texture of annealed Cu substrates made from Cu rods. The Cu rods had a diameter of $\phi = 10$ mm and were rolled to 0.19 mm with a thickness reduction per pass of 10%, and then annealed at different temperatures for 1 hour. From this figure, it is obvious that the range of annealing temperature to obtain the cube textured Cu substrates is very broad if the rolling deformation rate is large enough. Using a quantified analysis using ODF, the volume fraction of cube texture was calculated, it increases with increasing the annealing temperature, fig.2.16. The results show that the volume fraction of cube texture increases form 65 % to 97.5 % when the annealing temperature is increased from 400°C to 800°C.

A high volume fraction of cube texture is one requirements for Cu substrate but its the sharpness is also important. The effect of annealing temperature on the sharpness of cube texture is shown in Fig. 2.17. The results indicate that the cube texture becomes sharper with increasing annealing temperatures. But this effect is less rapid than the variation of the volume fraction of cube texture. The difference of FWHM value for out-of-plane texture is about 1^o, and for in-plane texture is only 2^o while the difference of volume fraction of cube texture is larger than 50%.

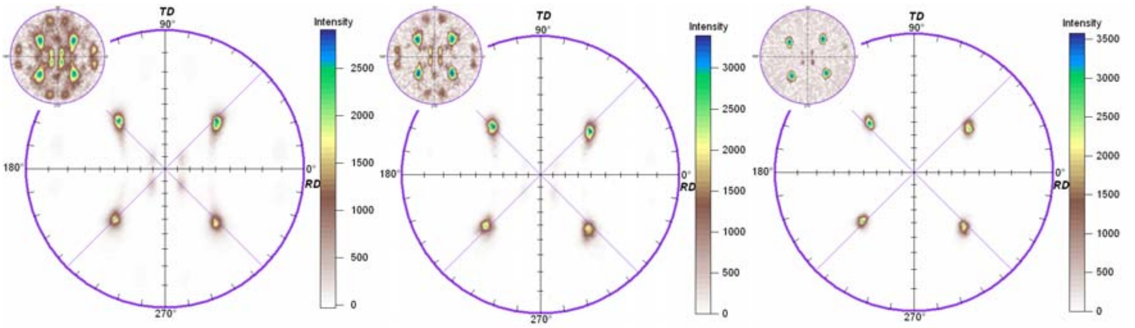

2.15a 2.15b 2.15c

Fig. 2.15 Influence of annealing temperatures on the formation of cube texture. 2.15a annealing at 400°C;2.15b annealing at 600°C;2.15c annealing at 800°C. In each of these figures, the insert shows the pole figure represented with a log scale for z axis.

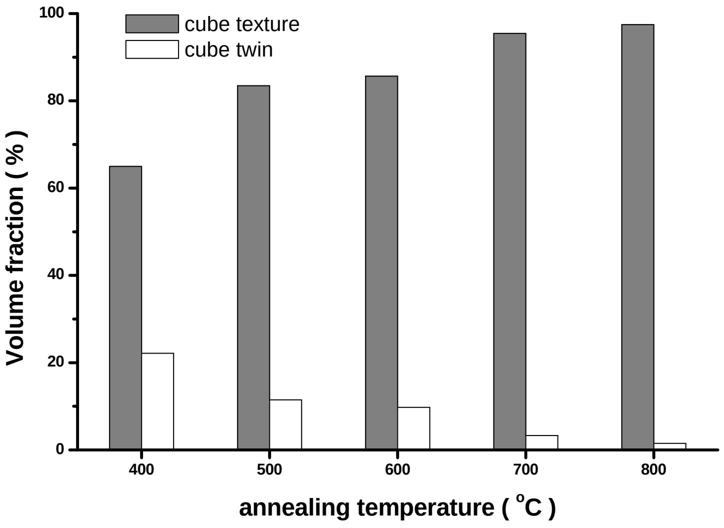

Fig. 2.16 The volume fraction of cube texture and of cube twin vs. annealing temperature

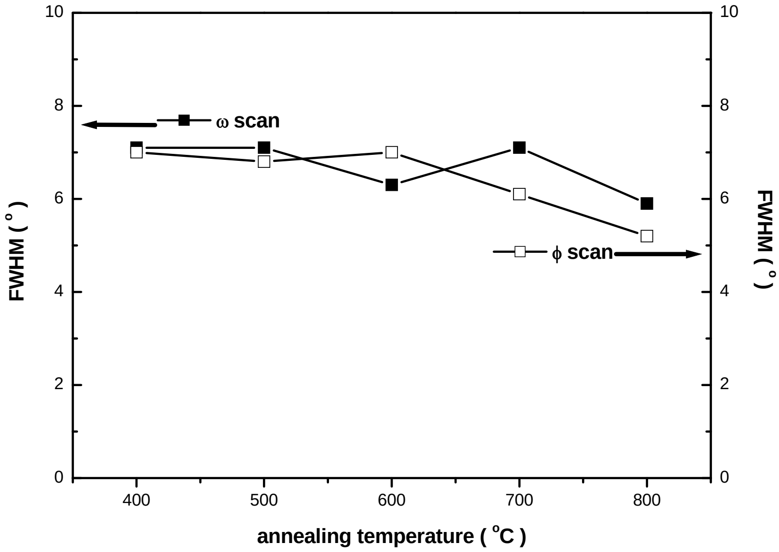

Fig. 2.17 Sharpness of cube texture of Cu tape vs. annealing temperature

2.3.2.3 Influence of annealing time on the formation and sharpness of the cube texture

Fig. 2.18 shows the annealing texture of Cu substrate versus time for Cu rods. The Cu rods had a diameter of ϕ = 10 mm and were rolled to 0.19 mm with a thickness reduction per pass of 10 %, and then annealed at 600°C for different times. The results show that the kinetic of cube texture formation is fast, the cube texture volume fraction reaches 85% in the first 10min and does not change much after (6 % between 10 min and 60 min). The annealing time has only a small influence on the cube texture volume fraction.

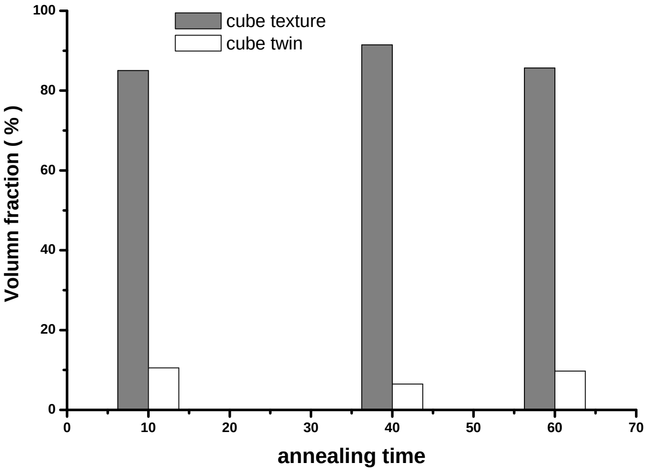

Fig. 2.18 The cube texture volume fraction vs. the annealing time

Table 2.4 Influence of the annealing time on the sharpness of cube texture of Cu tape

Annealing time (min)	FWHM value of ω scan (^{o})			FWHM value of ϕ scan (^{o})
	ϕ = 0^o	ϕ = 90^o	ϕ = rotation	
10	8.2	3.4	5.2	6.5
40	7.2	3.4	5.6	6.4
60	8.7	3.4	6.2	6.5

Note: “rotation”means that the sample rotates around the ϕ axis (72 ^{o}/s).

Table 2.4 shows the influence of the annealing time on the sharpness of cube texture of Cu substrate. The results show no influence of the annealing time. A comparison of all results shows that the annealing time of 40min is best.

A combination of Fig. 2.16, Fig. 2.18 and Table 2.4 shows that the volume fraction of and the sharpness of cube texture of Cu substrate are less sensitive to annealing time that to annealing temperature.

2.3.3 Macroscopic inhomogeneity of cube texture

During the rolling process, the stress state is different at the top surface and in the bulk. This results in macroscopic inhomogeneities in the rolling texture with thickness. Ref. [122,123] showed that there is a texture gradient across the sample. Our results also show a difference between the surface and the bulk (Fig.2.8). Maybe this macroscopic inhomogeneity of rolling texture will induce an inhomogeneity in the cube texture after annealing.

Table 2.5 compares the sharpness of cube texture of as-received samples to the sharpness of cube texture of a sample which thickness was reduced by 10% by polishing. The results show that there is very little advantage to remove the top surface. However, the roughness must be as small as possible and then it is most important that the rollers's surface be as smooth as possible.

Table 2.5 Inhomogeneity of cube texture across the normal direction to the tape

Sample's state	FWHM value of ω scan (^{o})			FWHM value of ϕ scan (^{o})
	$\phi = 0^o$	$\phi = 90^o$	ϕ = rotation	
as-received	8.7	3.4	6.2	6.5
after polished	8.1	4.7	7.8	7.6

Note: "rotation"means that the sample rotates around the ϕ axis (72 ^{o}/s)

2.3.4 Polishing technology of Cu substrate

The polishing process can be mechanical or electrolytic. Because mechanical polishing is not suitable for depositing a cube textured Ni layer on the Cu substrates by electro-deposition (this will be shown in the next chapter), Cu tapes was polished by electro-polishing.

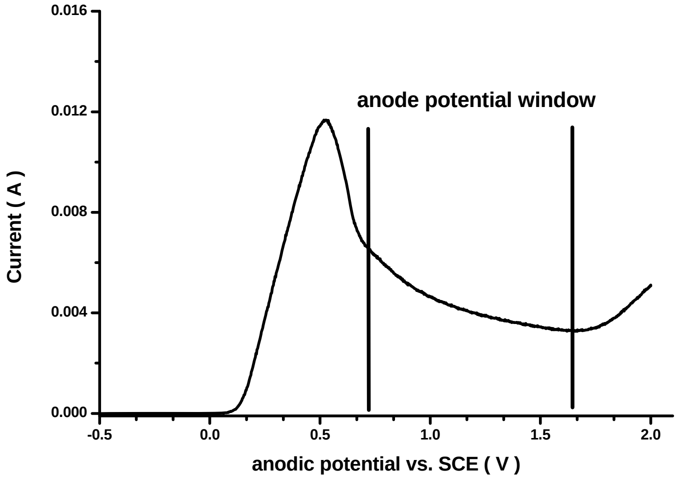

Fig. 2.19 The graph of anode current versus anodic potential.

Fig. 2.19 shows the graph of anodic current versus anodic potential. According to Fig. 2.19, the range of anodic potential should be from 0.7V (SEC) to 1.6V (SEC) in order to reduce the surface roughness. Because a high anodic potential is faster, we choose an anodic potential of 1.4V (SEC). Fig. 2.20 compares the sample's surface morphology of the polished zone to that of the un-polished one; Fig. 2.21 shows the morphology by AFM. The results show a clear improvement of the roughness after electro-polishing, but still some sharp peaks remain at a microscale which origin are unclear. The AFM show that the roughness is 8nm (R_{rms}) at a scale of 40μm × 40μm, and only 1nm (R_{rms}) if one excluding areas containing shap peaks Fig. 2.21b.

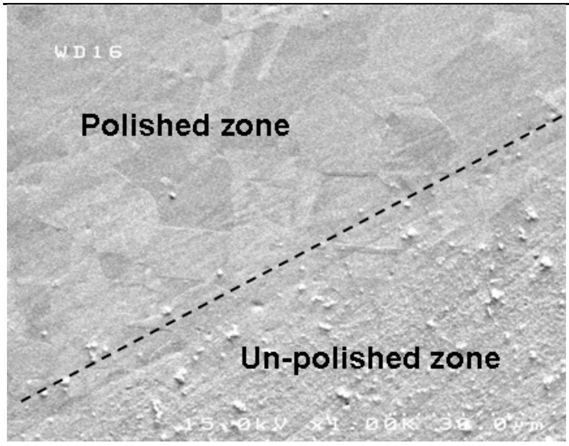

Fig. 2.20 Morphology comparison of polished zone and un-polished zone

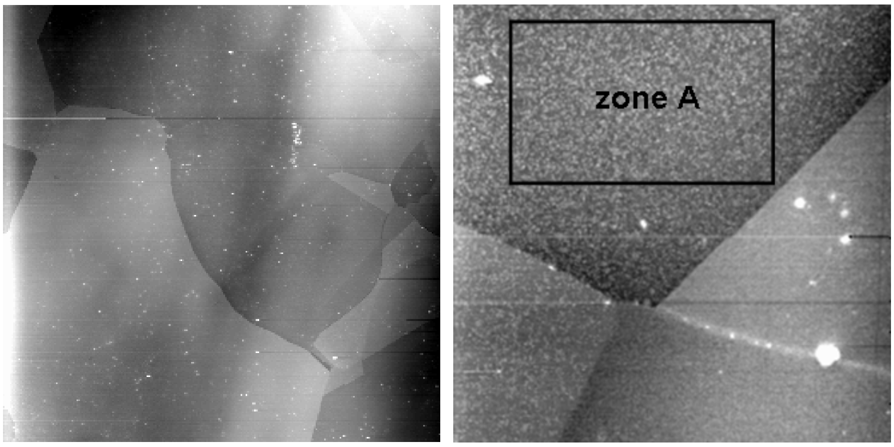

2.21a Rrms: 8nm (40μm × 40μm) 2.21b Rrms: 1.6nm (5μm × 5μm)

Fig. 2.21 AMF results of electro-polished sample

2.4 Summary

After adjusting the rolling-recrystallization process of Cu (Cu rods with diameter of $\phi = 10$ mm were rolled to 0.19mm with 10% of thickness reduction per pass, and then were annealed at 800°C for 1 hour), the volume fraction of cube texture of Cu tapes become larger than 97 % with a sharpness of the out-of-plane component equal to 5.9^{o}, and the sharpness of the in-plane texture equal to 5.2^{o}.

The rolling deformation rate is a key parameter to obtain the cube textured, it must be larger than a critical value to allows the cube texture to be formed. Thickness reduction per pass and rolling direction have not great influences on the sharpness of the texture.

Studying the recrystallization show that the development of cube texture in Cu substrate is very rapid, and increasing the annealing temperature provides shaper textures , at least below 800°C.

Chapter III Deposition of Cube-textured Ni Layer on Cu Substrate by Electro-deposition

3.1 Introduction

Cu substrates have a good thermal conductivity and non magnetic properties, but have some disadvantages: a low thermal stability of the cube texture and a poor oxidization resistance because Cu unlike Ni is not protected by its oxide layer. On the other hand, chemical solution deposition needs a high temperature to crystallize; in some cases more than 1000°C is required, bringing the substrate in a temperature range where its mechanical properties become poor.

In order to overcome these disadvantages of Cu, a special architecture is needed[31,33], alternatively a protecting layer deposited on the Cu substrate[35-37] might be used. The first way is realized by physical vapor deposition which is expensive. Our aim is to find a more economic way and the second route was investigated.

Ni is a good protecting material for Cu substrate, its advantages are as follow: 1) depositing Ni layer on a Cu tape is easy; 2) depositing a buffer layer on Ni substrates has been researched for several years and the knowledge can be transferred to our case; 3) during the thermal treatments used in coating process (involving buffer layer and YBCO layer crystallization), Cu and Ni will inter-diffuse to form a Cu-Ni alloy with lower magnetic properties than Ni. This is advantageous for decreasing the magnetic losses.

There are several ways to deposit Ni on a Cu tape, the electro-deposition being the most economical one. It is known that the texture of a deposited layer is usually a fiber texture which is not appropriate for coated conductors. In order to overcome this weak point the Ni layer will be deposited on a cube textured Cu tape. By this way, we expect the electro-deposited Ni layer to adopt the texture of the Cu tape. So the process of electro-depositing a Ni layer on a cube textured Cu substrate was studied in this chapter to develop a new Cu-Ni bi-metallic substrate.

3.2 Experiments

The preparation of the samples is as follow: the cube-textured Cu substrates were mechanically polished or electro-polished, and then cleaned by acetone in an ultrasonic bath. A Ni layer was then deposited on the cube-textured Cu substrates by electro-deposition.

The Watt-type electrolyte was chosen in which the major components were: $NiSO_4 \cdot 6H_2O$ (200 g/L), $NiCl \cdot 6H_2O$ (50 g/L), H_2BO_4 (40 g/L), and some organic additives. The pH value of as-received electrolyte was about 4.2.

The influences of cathodic potential, pH values of the electrolyte, and its temperature were studied on the texture of the deposited Ni layer. In these experiments, the electro-depositing time was 1 hour to provide a sufficiently thick layer. The Watt-type electrolyte was used after having explored the influences of the cathodic potential and temperature. The pH effect was studied by adding concentrated H_2SO_4 to decrease the pH to 3 and then adding concentrated ammonia to reach given values of the pH.

In order to identify the influence of the electro-deposition parameters on the sharpness of the Ni layer, the influence of the thickness must be eliminated. So the thickness of the Ni layer was limited to about 23μm during these experiments.

In addition to a sharp cube texture, a high thermal stability of the texture and low magnetic properties are also important for substrates of coated conductors. So after depositing a Ni layer, the samples were annealed at 950°C for 30min. The thermal stability of cube texture of samples was studied by comparing the textures before and after annealing. The magnetic properties were measured by Superconducting Quantum Interference Device (SQUID) to know the changes of magnetic properties after annealing. In these measurements, the applied magnetic field was parallel to the surface of the samples, and the measuring temperature was 77K.

All textures were checked by X-ray diffraction with a four circle goniometer (Seifect MZ IV equipped with Xenocs multilayer optics). All pole figures were plotted using raw data (no defocusing corrections) by the software IgorPro. ω and ϕ scans were measured and fitted by a Gaussian distribution to obtain the FWHM values. Information about texture measurements can be found in chapter II.

Finally, the $La_2Zr_2O_7$ (LZO) buffer layer was deposited on this new Cu-Ni bi-metallic substrate by the chemical solution deposition process[37], the deposition of LZO film by CSD process is presented in chapters IV, V and VI. The characteristics of LZO films were checked to know if this new Cu-Ni bi-metallic substrate is suitable for substrate of coated conductors or not. XRD diffraction was used to check the LZO film's texture, EBSD was used to check the surface texture of LZO film, and RHEED was used to check the surface crystallinity of LZO film.

3.3 Results and Discussions

3.3.1 Formation of the cube textured electro-deposited Ni layer

The preferred orientation of Ni electro-deposits is well known since many years[125-127]. In this section, the origin of such preferred orientation is not discussed but the research is focused on the type of texture obtained and on the parameters influencing their sharpness.

3.3.1.1 Influence of cathode potential on texture of Ni layer

Results of Ref.[127] show that the most important parameters are the cathode potential and the pH value of electrolyte. So the influence of cathode potential on the Ni layer's texture is discussed first.

For a given electrolyte, the relationship between the cathode potential and the cathode current density is fixed if the temperature is maintained constant. It means that controlling the cathode potential is equivalent to control the cathode current density. We preferred to control the cathode potential in our experiments.

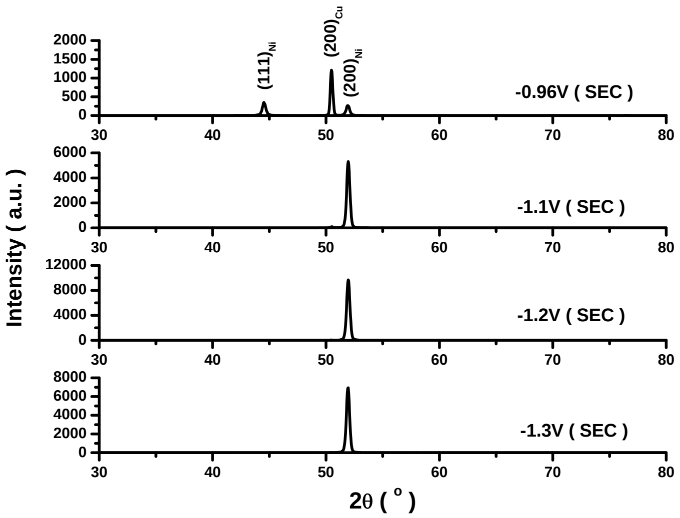

Fig. 3.1 θ-2θ scans of samples obtained under different cathode potential

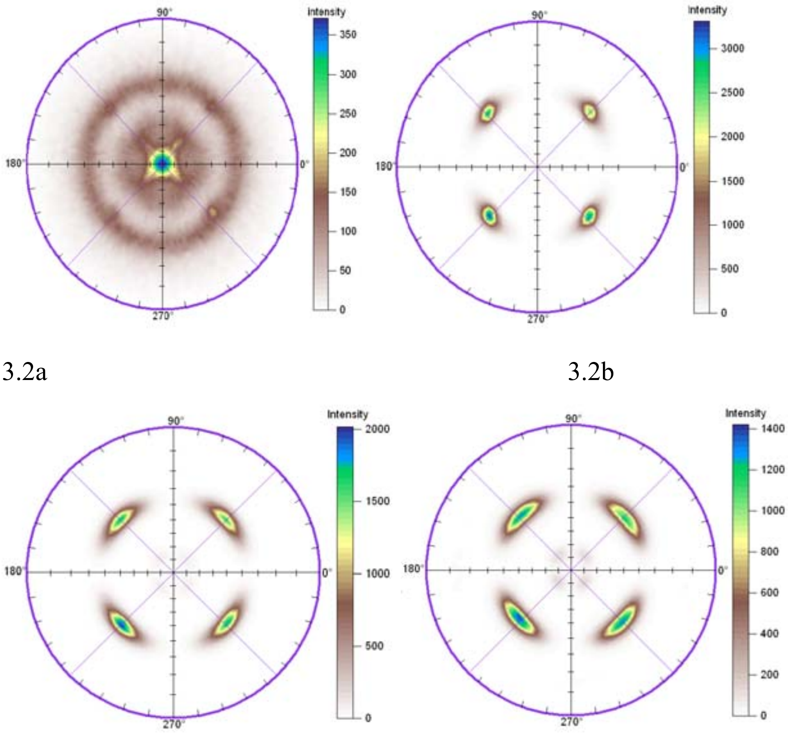

3.2a 3.2b

3.2c 3.2d

Fig. 3.2 Influence of the cathode potential on the texture of Ni layer. 3.2a: -0.96V (SEC); 3.2b: -1.1V (SEC);3.2c: -1.2V (SEC); 3.2d: -1.3V (SEC)

Fig. 3.1 shows how the texture of Ni layer is changed with modification of the cathode potential in the range -0.96V (SEC) to -1.3V (SEC). It is clear that the (111) diffraction peak of Ni is observed in θ-2θ scan when the cathode potential was -0.96V (SEC), but it is not observed for smaller values. Fig. 3.2 shows the (111) pole figures of the samples examined in Fig. 3.1. Because the difference of diffraction peak position of $(111)_{Ni}$ with $(111)_{Cu}$ is about 1^o, it is large enough to separate their diffraction contribution, so the Ni(111) poles were investigated and are shown on Fig.3.2. It proves that the cube textured Ni layer can be obtained only if the cathodic potential is lower than -0.96V (SEC).

Although the main texture component of the Ni layer in Fig. 3.2a is not that of a cube texture, the cube texture contribution can be found in this figure. This is also proved in by Fig. 3.3 which plots a $\phi(111)_{Ni}$ scan of that. Combining the results of Fig. 3.2a with that of Fig. 3.3 shows that, the texture of Ni layer is fixed by that of the Cu substrate in the initial stage of the electro-deposition process. With increasing thickness, the texture of the Ni layer is controlled by the conditions used during the electro-deposition. So the final samples have a cube texture mixed with other components.

In previous works[125-127], it was thought that the stress state of the deposit was similar to that of samples submitted to heavy rolling, so the researchers believed that the texture of the deposit resulted form internal stress. But this can not explain the origin of the preferred orientation found in electro-deposited layers of Cu, Zn, and Au, in which the internal stress in the deposited layer was very low. Recently, more people refer to the two-dimensional nucleation theory[126] or to the geometrical selection theory.

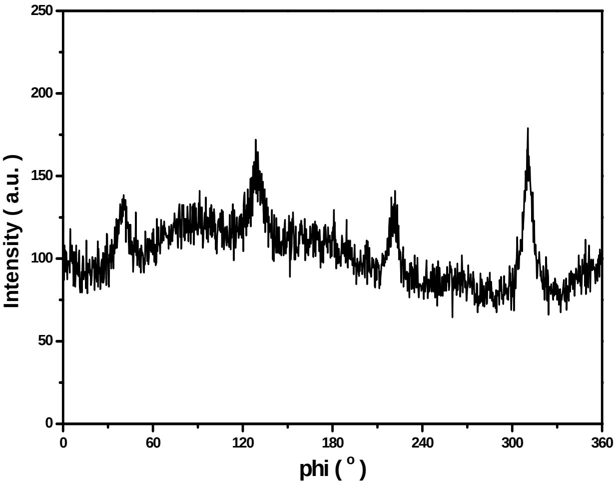

Fig. 3.3 ϕ $(111)_{Ni}$ scan of the sample investigated in Fig. 3.2a

The two-dimensional nucleation theory assumes that the probability of the formation of a two-dimensional nucleation can be expressed by formula 3.1:

$$P_{hkl} = \exp(-W_{hkl}/KT) \quad (3.1)$$

in which the W_{hkl} represents the work required to form a two-dimensional nucleus of the type (hkl), the value of W_{hkl} is linked to the cathode overpotential which is the difference of the cathode potential at a given current density with the cathode potential at equilibrium. This equation implies that the two-dimensional nucleus, whose formation works are the smallest appears first. Based on this idea, this theory predicts that <111> texture is formed for low values of the cathode potential, the <100> texture is formed with more negative cathode potential; the <110> texture, <113> texture or <210> texture appear if the cathode potential is too negative.

The geometrical selection theory claims that the formation of a preferred orientation is due to the difference between the growth rates of the various crystal faces. Reddy[125] believed that the growth rate of a crystal face was influenced by the adsorption of hydrogen which is crystal face dependent. For a given face, it differs with the electrodeposition conditions; the growth rate for a given face decrease with the amount adsorbed. Based on these ideas, Amblard developed a complete description for electro-deposition of Ni[127]. He assumed that the cathode over-potential required for the formation of a two-dimensional nucleus was lower than the usually applied cathode over-potential. In consequence, all type of two-dimensional nucleus could appear. That is why he thought that the two-dimensional nucleus theory could not explain the formation of preferred orientation of deposits. In contrary, he believed that, not only the adsorbed hydrogen influences selectively the growth rate of different crystal faces, but also other chemical species may interfere. Since the concentrations of the different adsorbed species depended on the electro-depositing conditions, it should be possible to control the texture formation of deposit by controlling the electro-depositing conditions. The results of Amblard showed that while <100> orientation was regarded as being characteristic of a rather free growth, the three other textures (<110>, <113> and <210>) were associated with definite chemical species (H_{ads}, $Ni(OH)_2$ or gaseous H_2) which selectively influence the Ni electro-crystallization.

Although results in Fig. 3.2a seem not to totally agree with these theories for cathode potential close to -0.96V (SEC), the theory of Amblard is preferred because it can explain very well the results developed in the next paragraph. Amblard thought that the metallic surface was much more sensitive to any strong adsorbants since there was practically no renewal. At the same time, the orientation of electrodeposited Ni layer was sensitive with the organic additives[127]. Maybe the different organic additives were used during the electro-depositing process, it resulted in the different texture type.

Fig. 3.2b show a typical cube texture of the Ni layer, by decreasing the cathode potential to more negative values shows only a broadening of the poles size. Two reasons explain this: one is due to the increase of thickness of the Ni layer, the other is due to the cathode potential itself.

The thickening rate of the Ni layer is linked with the cathode potential. The cathode current density and therefore the thickening rate of the deposit increase for decreasing cathode potential. During the electro-deposition, the texture of the deposit will change to a fiber texture with increasing thickness. Therefore the in-plane mosaicity will change very much. In order to differentiate between thickness effects and voltage effects, the samples were polished in order to reduce to similar values by steps of 20 μm. The results are shown in Table 3.1. It can be found that the in-plane texture of the Ni layer is sharper for decreasing thickness. It is a clear proof that the poor sharpness of the cube texture results from an excessive thickness of the Ni layer. On the other hand the sharpness of the out-of-plane texture is not influenced by the the thickness of the Ni layer.

Table 3.1 Influence of thickness of Ni layer on the sharpness of cube texture of Ni layer

Thickness (μm)	Out of plane FWHM (ω scan (°) measured with rotation)	In plane FWHM (ϕ scan (°))
as-received sample	8.2	27.7
after the first polish	------	16.1
after the second polish	8.1	8.1

Note: “rotation”means that the sample rotates around the ϕ axis (72°/s)

Based on the results of Table 3.1, it is clear that the influence of the thickness of the Ni layer must be eliminated in order to know the influence of the cathode potential on the sharpness of its texture. The influences of the cathode potential are shown in Table 3.2, in which all the deposit had the same thickness (23μm). Because the sharpness of the deposit also depends on that of the texture of the substrates (Cu substrate), these are also reported in Table 3.2. From this table, it is clear that, the sharpness of the Ni layer's texture is slightly poorer than that of the Cu substrate. The sharper the substrate's texture of Cu is, the better the Ni layer's texture is.

Table 3.2 Influence of cathode potential on the sharpness of cube texture of Ni layer

cathodic potentian（SEC）		FWHM value of ω scan (°)			FWHM value of ϕ scan (°)
		$\phi = 0^o$	$\phi = 90^o$	ϕ = rotation	
-1.1V	Ni layer	9.9	4.2	7.3	8.0
	Cu substrate	8.3	3.5	6.6	7.2
-1.2V	Ni layer	9.2	4.2	6.1	8.3
	Cu substrate	7.5	3.5	5.2	8.1
-1.3V	Ni layer	8.4	4.1	6.9	7.6
	Cu substrate	6.5	4.2	6.7	7.4

Note: “rotation”means that the sample rotates around the ϕ axis (72°/s)

To show concretely this influence, Fig. 3.4 was plotted by using data in Table 3.2. The insert shows the cathode potential versus the difference between the sharpness of the Ni layer's texture and that of the Cu substrate's texture. The results show that the cathode potential has not a large influence on the sharpness of the Ni layer's texture. The largest difference is just 1° for in-plane texture and 0.6° for out-of -plane texture. his figure also shows that lower cathode potential (-1.3V (SEC)) gives sharper textures. However, in this condition much gaseous hydrogen is delivered at the cathode and susceptible to creates defects like pores. So for practical application, we preferred to limit the cathode potential to -1.2V (SEC).

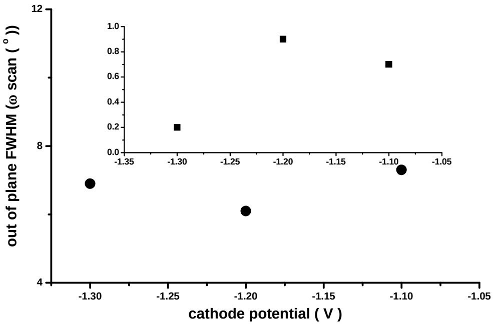

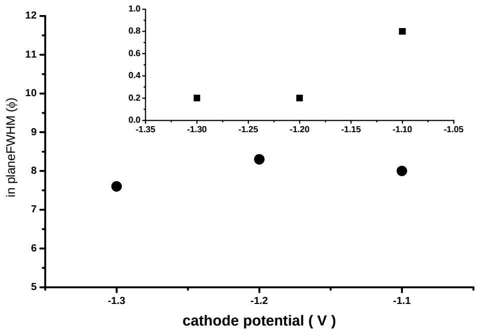

3.4a 3.4b

Fig. 3.4 Influence of the cathode potential on the sharpness of Ni layer's texture. 3.4a: out-of-plane; 3.4a: in-plane. Insert: difference with Cu

3.3.1.2 Influence of the pH on the texture of the electro-deposited Ni layer

The influence of the pH of the electrolyte has been explored since a long time. For high pH, some hydroxides are trapped in the Ni layer, which increase its brittleness. For too low pH[128] the current efficiency is decreased. Discussing these influences is not the aim of this section, in contrary we focus on the influence of the pH on the texture of the Ni layer.

Fig. 3.5 and Fig. 3.6 show respectively θ-2θ scan and (111) pole figure of Ni layers obtained under different pH values. This shows that the texture of Ni layers is a cube texture only if the pH range from 4 to 5. There is an additional unknown contribution ($2\theta = 42^{o}$) if the pH = 6.

Based on the viewpoint developed by Amblard, the Ni layer should have a <110> texture if the pH value is low and a <211> texture at high pH. The angle between the (111) plane and (110) plane is 35.26^{o}, and it become 19.47^{o} or 61.84^{o} with (211) plane. So diffraction intensities should be found at $\chi = 35.26^{o}$ in a (111) pole figure if the a <110> texture would have developed, it should be found at $\chi = 19.47^{o}$ or 61.84^{o} for a <211> texture. After analyzing Fig. 3.6, it can be found that the main diffraction contribution is observed at $\chi = 35.26^{o}$ in Fig. 3.6a, and at $\chi = 19.47^{o}$ and 61.84^{o} in Fig. 3.6d. The above-mentioned analysis proves that the texture of the Ni layer is a <110> fiber texture for pH = 3, and a <211> fiber texture for pH = 6. These results agree very with the predictions of the theory of Amblard.

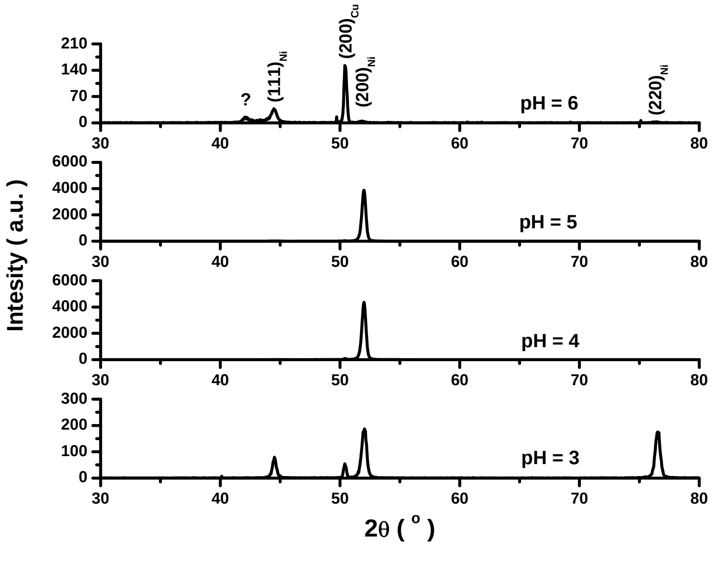

Fig. 3.5 θ-2θ scan for Ni layers obtained under different pH values

3.3.1.3 Influence of the temperature of the electrolyte on the texture of the deposit

Increasing the temperature of the electrolyte enables to accelerate the electro-deposition process and to decrease the cathode polarization. It is then relevant to control the temperature of electro-deposition, this is made in the range of 50°C.

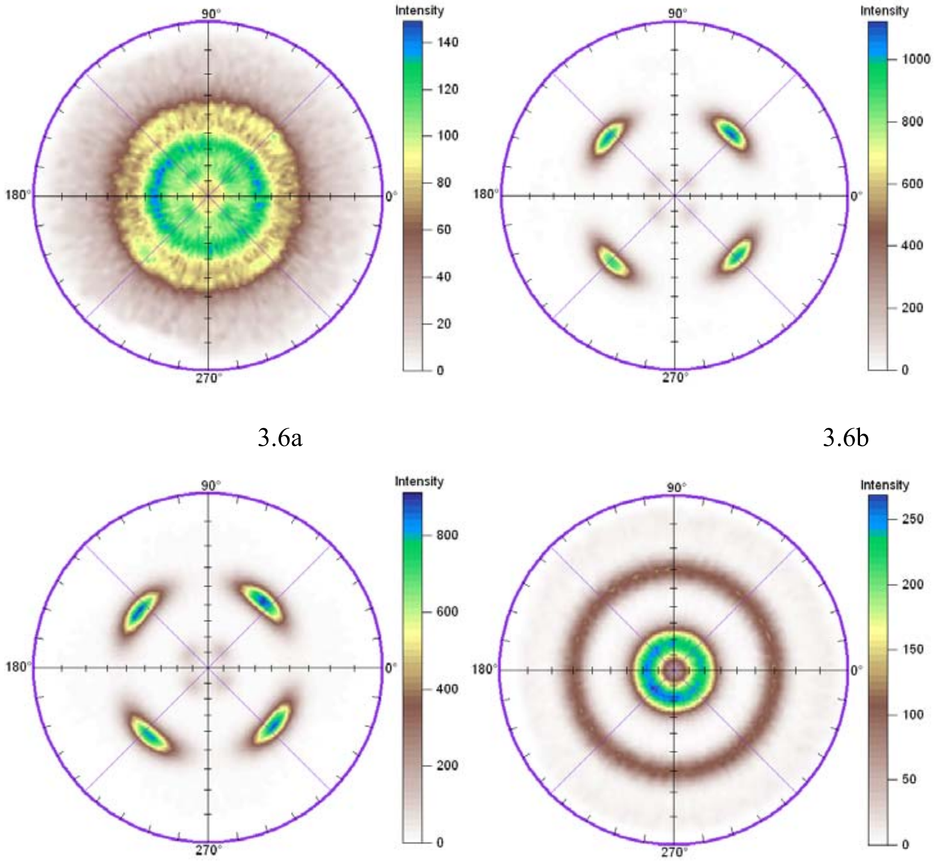

3.6a 3.6b

3.6c 3.6d

Fig. 3.6 (111) pole figures of Ni layers obtained under different pH values. 3.6a: pH = 3; 3.6b: pH = 4; 3.6c: pH = 5; 3.6d: pH = 6

Fig. 3.7 and Fig. 3.8 show respectively the θ-2θ scan and the (111) pole figure of a Ni layer deposited at 55℃ with a cathode potential of -1.2V (SEC). The texture of this Ni layer is not a cube texture, but a <211> fiber texture. This result is also in agreement with the theory of Amblard. Because the deposition temperature is increased, the deposition process is accelerated. It induces an increase of the local pH near the cathode, and the high pH value finally induces the formation of <211> texture. This explanation was confirmed after measuring the pH during the deposition at 55°C, it increased from 4.2 at the beginning to >5 after some time of deposition.

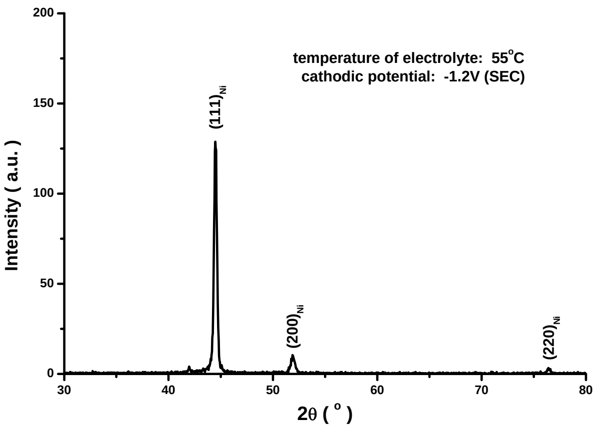

Fig. 3.7 θ-2θ scan of a Ni layer deposited at 55°C.

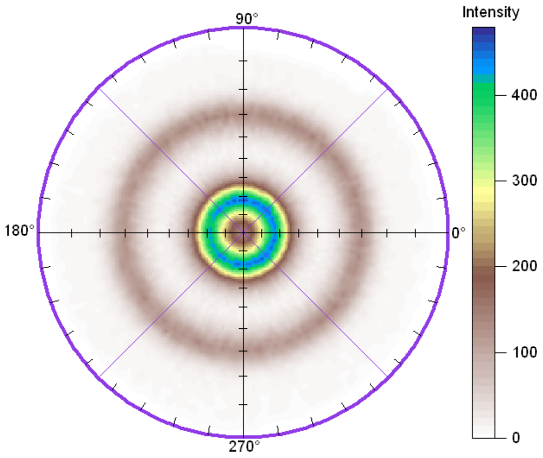

Fig. 3.8 (111) pole figure of a Ni layer deposited at 55°C

3.3.1.4 Influence of the surface preparation of the Cu substrate on the texture of the Ni layer

Fig. 3.9 shows textures of Ni layers which were deposited on Cu substrates whose surfaces were as received (Fig. 3.9a), mechanically polished (Fig. 3.9b), or electro-polished (Fig. 3.9c), all electrodepositing parameters being identical. It is clear that the best result is obtained on the Cu substrate which was electro-polished; some other texture components is detected in the Ni layer which was deposited on the as-received Cu substrate; the texture of the Ni layer is not a cube texture if the Cu substrate was mechanically polished. In order to check that the non-cube texture in Fig. 3.9b was not due to the texture of the substrate, its texture was probed and is shown the in the insert of Fig. 3.9b ((111) pole figure of Cu). It is clear that the non-cube texture of the Ni layer is not due to the texture of Cu substrate.

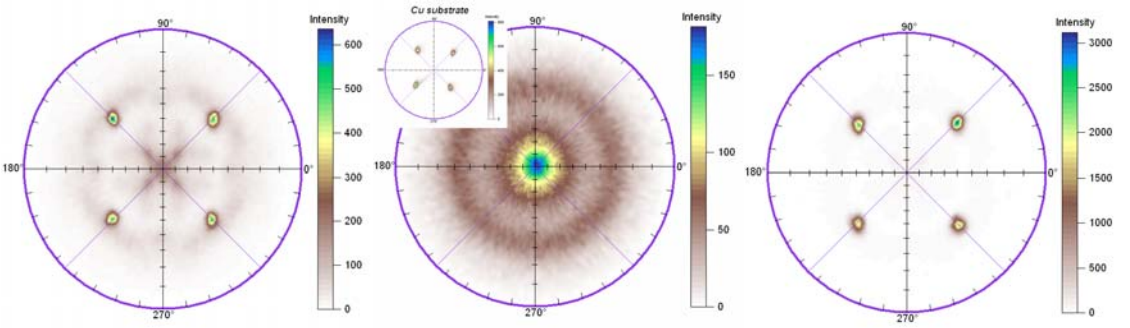

3.9a 3.9b 3.9c

Fig. 3.9 Influence of surface preparation of the Cu substrate on the texture of electro-deposited layer. 3.9a: as-received Cu substrate; 3.9b: mechanically polished Cu susbtrate; 3.9c: electro-polished Cu substrate. The insert shows the pole figure represented with a log scale for z axis

The above results show that the type of texture of the Ni layer depends not only of the Cu's texture and electro-depositing conditions, but also on its surface characteristics. The cube texture of the as-received Cu substrate was rather sharp, but the roughness of its surface in the as-received Cu substrate was high (rolling traces) contributing to develop wrong orientations in the deposited layer, perhaps because adsorbates coved these defects and modify the growth directions of the deposition.

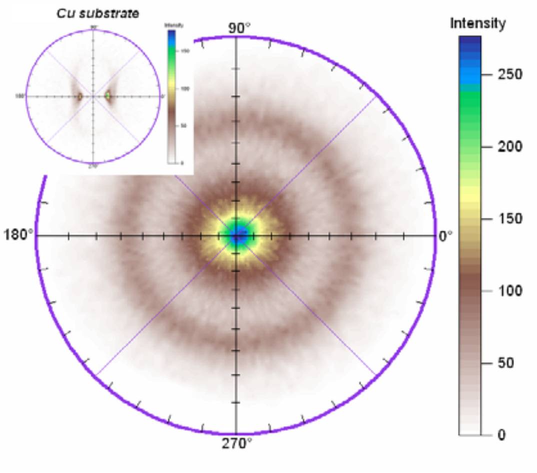

Fig. 3.10 (111) pole figure of a Ni layer electro-deposited on a rolled Cu tape. The insert shows the pole figure represented with a log scale for z axis.

Because the cathodic potential was sufficiently low, the adsorbates can be partially released and finally the texture of the deposit is a mixture of a main cube texture with other components. The above-mentioned reason can also explain why the best result can be obtained on the electro-polished Cu substrates. Its surface is better than that of as-received Cu substrate with no site for adsorption, permitting the development of the cube texture.

Mechanical polishing develops stress on the surface which influences the nucleation of the Ni layer on that of the Cu resulting in a fiber texture, fig.3.9b. It is then valuable to compare with the Ni electro-deposition on as rolled Cu tape which texture is shown in the insert of fig.3.10. The Ni layer has the same fiber texture than for a deposit on a mechanically polished surface. Clearly the detrimental influence of stresses on the surface is illustrated in these two cases.

3.3.2 Thermal stability of Texture and magnetic property of Cu-Ni bi-metallic substrate

3.3.2.1 Thermal stability of texture of Cu-Ni bi-metallic substrate

It is not sufficient that the deposit has a sharp and high volume fraction of cube texture, its cube texture must be thermally stable.

Table 3.3 Influence of annealing on the sharpness of the Ni layer's cube texture

	FWHM value of ω scan (°) (ϕ = rotation)	FWHM value of ϕ scan (°)
before annealling	6.1	8.3
after annealing	5.9	6.0

Note: "rotation"means that the sample rotates around the ϕ axis (72°/s)

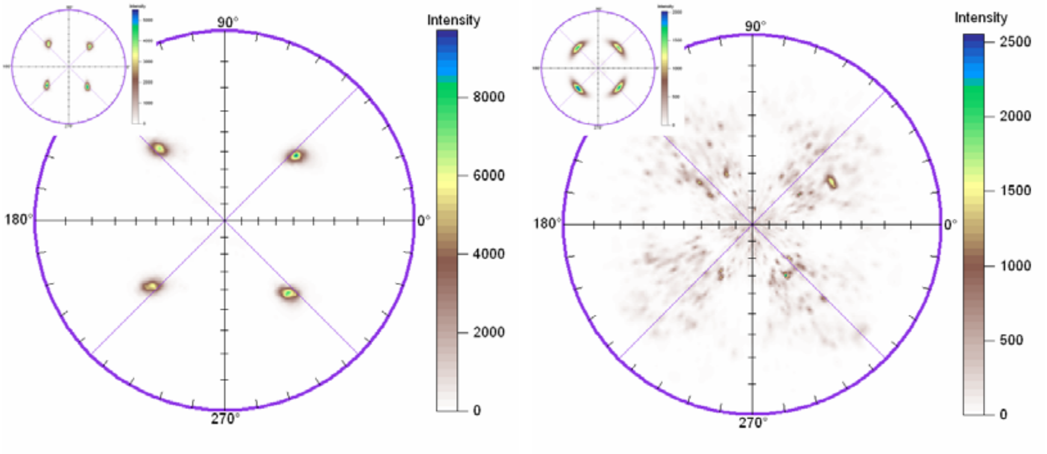

3.11a 3.11b

Fig. 3.11 Influence of Ni layer's thickness on its texture stability. 3.11a 23µm; 3.11b 63µm. The insert shows the pole figure of the sample before annealing, it is represented with a log scale for z axis.

Fig. 3.11 (a and b) shows the (111) pole figures of two samples which were annealed at 950℃ for 30min, their thicknesses were 23 µm and 63 µm respectively. The insert shows the texture before annealing. This figure points out that the thick Ni layer is less stable than the thin one. This may be related with defects and/or stress in the Ni layer, increasing with its thickness and favoring secondary recrystallization in the thick deposit.

Comparing the sharpness of their texture is made in Table 3.3. The texture's sharpness improves a little after annealing. This may be due to improvements in the crystallinity after annealing. No matter how, it is of benefit to depositing an oxide buffer layer on this Cu-Ni bi-metallic substrate.

3.3.2.2 Magnetic property of Cu-Ni bi-metallic substrate

Reducing AC losses requires a low ferromagnetic substrate. So the magnetization of a Cu-Ni bi-metallic substrate was measured by Superconducting Quantum Interference Device (SQUID) at 77 K. The magnetization of the initial Cu-Ni substrate was measured before and after annealing (950°C for 30mins) and compared in fig. 3.12.

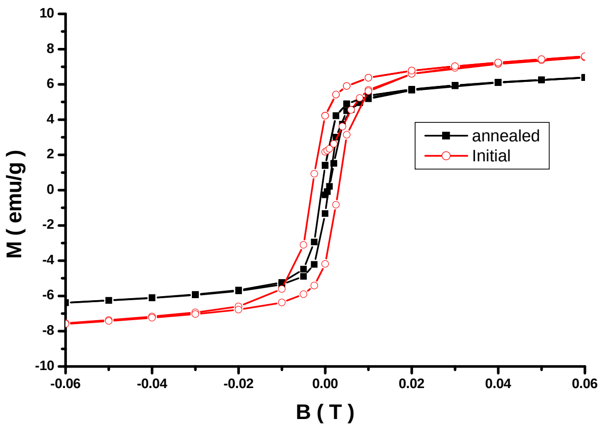

Fig. 3.12 Magnetic hysteresis loop of a Cu-Ni sample before and after annealing. The applied magnetic field was parallel to the surface of the samples, and the measuring temperature was 77K.

The results, Fig. 3.12 show that due to the interdiffusion between Cu and Ni, the magnetization and hysteresis decrease after annealing. A comparison of the data in Fig. 3.12 with data shown in Ref. [20] implies that the magnetic losses induced by this Cu-Ni substrate are smaller than those induced in Ni-5at%W substrates.

3.3.3 Characteristics of $La_2Zr_2O_7$ film deposited on Cu-Ni bi-metallic substrates

From the previous results, it is clear that Cu-Ni bi-metallic substrates have a good cube texture and low magnetization. Then Cu-Ni bi-metallic substrates are potential substrates for coated conductors, the successful deposition of a textured film would be a direct proof of it. $La_2Zr_2O_7$ oxide has been chosen as a good candidate for this.

Fig. 3.13 shows a θ-2θ scan curve and (222) pole figure of LZO film deposited on Cu-Ni bi-metallic substrate by chemical solution deposition, which deposition process is described in chapters IV- V and VI. Clearly LZO film has a good cube texture. In order to show its sharpness in-plane texture and of out-of-plane texture were recorded, Fig. 3.14 and Table 3.4. It implies that the sharpness of LZO film is very good, even better than that of the substrate.

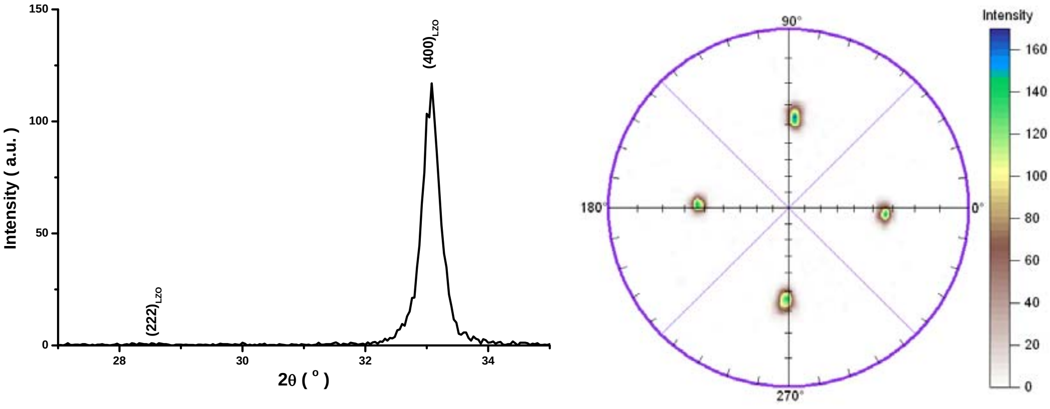

θ-2θ scan of LZO film (222) pole figure of LZO film

Fig. 3.13 texture of LZO film deposited on Cu-Ni substrate by CSD process

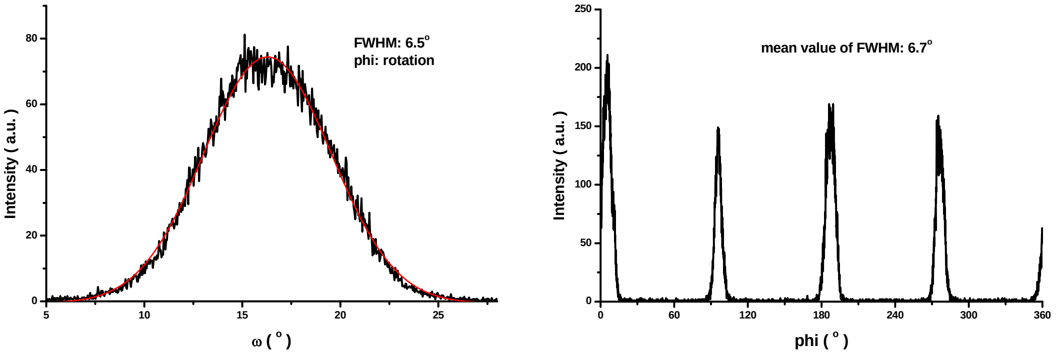

ω(400) scan of LZO film ϕ(222) scan of LZO film

Fig. 3.14 Sharpness of LZO film's texture on Ni-Cu texture

Table 3.4 Sharpness of LZO film's texture vs. sharpness of substrate's texture

	FWHM value of ω scan (°) (ϕ = rotation)	FWHM value of ϕ scan (°)
$La_2Zr_2O_7$ film	7.6	7.9
Cu-Ni bi-metallic substrate	8.3	7

Note: "rotation"means that the sample rotates around the ϕ axis (72^o/s)

Using this geometry, XRD cannot provide information concerning the surface. Electron Backscatter Diffraction (EBSD) and Reflection High Energy Electron Diffraction (RHEED) which are very sensitive to surface have been used to check the sample's surface texture and crystallinity. Fig. 3.15 and Fig. 3.16 show the EBSD and RHEED results, respectively. Both agree that cristallinity and texture of these LZO films are correct.

This results show that a LZO film can deposited successfully on the Cu-Ni bi-metallic substrate by chemical solution deposition process.

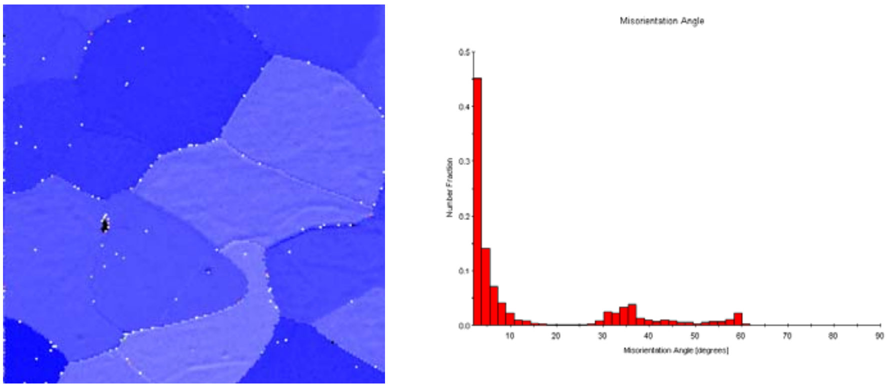

EBSD image (80μm × 80μm) misorientation angle

Fig. 3.15 Texture of LZO/Ni-Cu by EBSD

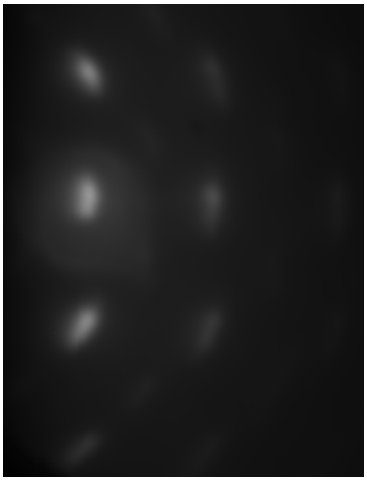

Fig. 3.16 Surface diffraction of LZO/Ni-Cu by RHEED.

3.4 Summary

Based on the research of the electro-depositing conditions on the texture of electro-deposited Ni layers, the electro-depositing process was optimized, and sharp and high volume fraction of cube texture of Ni layer was obtained. In plane texture and out of plane texture are sharp (in plane FWHM = 8.3° and out of plane FWHM = 6.1°), this is even better after annealing at 950℃ for 30mins (in plane and out of plane FWHM = 6°). Thus the Cu-Ni is sufficiently stable to support the heat treatments required to deposit oxide buffer layer like LZO by CSD process.

The deposition of LZO film on the Cu-Ni bi-metallic substrate successfully proves that the Cu-Ni bi-metallic substrate is a good substrate for coated conductors.

Chapter IV Deposition of $La_2Zr_2O_7$ Film on Metallic Substrate by Chemical Solution Deposition Process

4.1 Introduction

The functions of buffer layer require that the material have the following characteristics: 1, low mismatch with YBCO layer and the metallic substrate; 2, to act as a chemical barrier preventing diffusion of metallic elements into YBCO layer and also preventing oxidation of the metallic substrate during deposition of YBCO layer; 3, chemical inertness with both the metallic substrate and the YBCO layer. Based on the above-mentioned characteristics, buffer layer materials of Y-stabilized ZrO_2[51,71], Y_2O_3[50], CeO_2[70], $SrTiO_3$[73], $La_2Zr_2O_7$[52,75,119,120] and $Gd_2Zr_2O_7$[46] are focused interest of many research groups.

It is difficult to combine all the required functions of the buffer layer in a single buffer layer, so the most often used architecture is composed of two, three (or even up to ten different oxide layers), like $Y_2O_3/YSZ/CeO_2$ [88], $La_2Zr_2O_7/CeO_2$ [75,81], and $Gd_2Zr_2O_7/CeO_2$ [46,82].

Besides the needed characteristics for buffer layer, costless fabrication process of buffer layer is required. Chemical solution deposition (CSD) method is a good simple enconomical fabrication process of buffer layer, and it is also a highlight fabrication method of buffer layer recently. A new data reported by Oak Ridge National Laboratory (ORNL) shows the Ic value of coated conductor fabricated by All CSD process is 140A/cm-W[81]. This result implies that chemical solution deposition process is a good potential method to fabricate coated conductors.

Comparing with physical vapor deposition process, CSD process is economical and simple, and it fits well for large scale fabrication. However a shortcoming of CSD is the temperature of treatment which is very high, sometimes larger than 1000°C[50,70,120]. It restricts the choice of substrate materials to those sufficiently stable. For example, Cu-based substrate is not compatible alone with CSD process. Recently, Knoth et al ref.[52] show that $La_2Zr_2O_7$(LZO) buffer layer can be deposited directly on Ni-5at%W substrate by CSD process at 960°C. This opens the way to Cu-based substrate. LZO belongs to a cubic crystalline system with a lattice parameter of 10.786 Å, the lattice mismatch between LZO and YBCO is only 0.2% (YBCO is under compression), moreover, LZO layer can prevent diffusion of Ni and W very well. All these information shows that LZO is a good material of buffer layer.

In this chapter, the fabrication of a precursor solution, the powder and film formation of LZO from this precursor are recorded.

4.2 Experiments

Lanthanum(III) 2,4-pentanedionate (La(acac)3) and zirconium(IV) 2,4-pentanedionate ($Zr(acac)_4$) were used as solute. After weighing a stoichiometric mixture of $La(acac)_3$ and $Zr(acac)_4$, it was introduced into propionic acid at a concentration of 0.87 mol/l (with respect La plus Zr). The solution was place in an ultrasonic bath for 15 min, then stirred and heated at 60°C for 30 min. Finally, a transparent yellow-colored precursor solution was obtained[92].

The precursor solution was dried at 100°C to remove the solvent, a dry precursor powder was thus obtained, which was named after the “as-received” powder. The as-received powder was heat treated at different temperatures for 30 min under Ar-5%H_2 atmosphere, in which the flux of gas was fixed to 0.5 l/h by a flowmeter. The residual powder was checked by x-ray, and analyzed chemically to determine its chemical stoichiometry.

The precursor solution having a concentration of 0.87 mol/l was diluted with propionic acid to concentration of 0.5 mol/l or 0.1 mol/l. Constantan substrates (size: 5×5 mm) were cut from a long tape[26], cleaned by acetone for 10 min in an ultrasonic bath, and covered by the precursor solution using spin-coating (rotation speed: 2500 rpm, rotation time: 30 s, acceleration: 3000 rpm/min). The samples were dried at 80°C for several minutes in air after spin-coated. Finally, the samples were heated at 950°C for 30 min under Ar-5%H_2 flow.

The texture of all samples was characterized by a four-circle diffractometer (Siefert MZ IV using Xenocs multilayer optics) working at the Cu Kα wave length. The surface morphology of samples was checked by Scanning electron microscope (SEM) equipped with an EDS device.

4.3 Results and Discussions

4.3.1 Preparation of the Precursor Solution

4.3.1.1 Choice of the solvent

The preparation of the precursor solution is a key for the deposition an oxide film by CSD process. The characteristics of the precursor solution will influence directly the heat treatment process. Of course, the solubility of the precursor must be sufficiently large.

Table 4.1 Dissolvability of $La(acac)_3$ in different solvents

solvent	dissolvability
DMF	< 0.01 mol/L
DMSO	< 0.01 mol/L
Toluene	< 0.01 mol/L
Pyridine	~ 0.01 mol/L
Acetic acid	Not stable
Propionic acid	~ 0.8 mol/L

It is found that $Zr(acac)_4$ can be dissolved into many different solvents, but it is difficult to find a good one for $La(acac)_3$. Table 4.1 shows the dissolvability of $La(acac)_3$ into different solvents, carboxylic acid being the best. The carboxylic acid with short carbon chains is preferred because it will decompose with less amount of waste. Experimental results show that the precursor solution is not stable if the solvent is acetic acid, but it can be stabilized by methanol[52]. The precursor solution formed with propionic acid is very stable (during two months), even the the laboratory atmosphere, but the concentration of the solution must be smaller than 0.8 mol/l (with respect to La^{3+}). For these reasons we choose the propionic acid as a final solvent.

The good dissolvability of acetylacetonate into carboxylic acid is due to the chemical characteristic of acetylacetone. Because acetylacetone could ionize in aqueous solution as a weak acid:

$$CH_3COCH_2COCH_3 \leftrightarrow H^+ + CH_3COCHCOCH_3^-$$

La(acac)$_3$ and Zr(acac)$_4$ are weak acid salts, and can dissolve into propionic acid which is stronger than acetylacetone. Based on a theoretical calculation, 0.84 g La(acac)$_3$ and 0.93g Zr(acac)$_4$ can be dissolved into 1ml of propionic acid, but the largest concentration of precursor solution is only 0.87 mol/l (per metal).

Besides dissolvability, the solvent should not react with metallic substrate. Three kind of metallic substrates, Ni-5at%W substrate, constantan substrate and Cu-Ni bi-metallic substrate[37], were dipped into propionic acid for 12 hours, no reaction between metallic substrates and propionic acid can be observed.

All these results show that the propionic acid is a good solvent.

4.3.1.2 Pyrolysis characteristics of the precursor solution

CSD process can usually be divided into three steps: i)depositing a film, ii) pyrolysing the precursor, iii) crystallizing the film. In some cases, pyrolysis and crystallization can occur simultaneously. The choices of pyrolysis or crystallization temperatures are based on TG analysis.

Fig. 4.1 shows the TG analysis of the precursor powder obtained after drying the precursor solution at 80°C, the experiment was made under Ar flow. From Fig. 4.1, it is found that most of the weight loss is completed for temperatures higher than 400°C, but still a small weight loss remain up to 1000°C.

Fig. 4.2 shows the TG analysis of a mixed powder (La:Zr = 1) of La(acac)$_3$ and Zr(acac)$_4$. Comparing data of Fig. 4.1 to those of Fig. 4.2 shows that the weight loss of the mixed powder is 30% at 250°C while it is 20% for the precursor powder. This difference shows that La(acac)$_3$ and Zr(acac)$_4$ react with propionic acid and form a new propionate.

Considering that the precursor powders was a propionate, the theoretical weight loss of the precursor powder should be 61%, while the value obtained from Fig. 4.1 is only 57%. The difference, 4%, results in a residual fraction (like carbon base species) or is un transformed part of the precursor. In order to know which compound is responsible, La(acac)$_3$ and Zr(acac)$_4$ were dissolved separately into propionic acid to obtain La-precursor and Zr-precursor, TG analyses were done after drying the solvent. The results are shown in Fig. 4.3. It can be observed that La-compound is completely decomposed above 900°C giving a residue composed of pure La_2O_3 by XRD (Fig. 4.4a). Comparing with the theoretical weight loss for Lanthanum propionate (54.4%), the observed weight loss of 58.2%, Fig.4.3a, shows that there are some hydrated water molecules, amounting to 1.78 mol/mol of propionate.

Fig. 4.3b shows the TG analysis of the Zr-compound. The weight loss continues even up to 900°C. Assuming that the Zr-compound were a zirconium propionate, the difference between the theoretical weight loss and the observed one would be 8.8%. The XRD data of the residual powder after TG analysis confirm the presence of ZrO_2 with no other phase (Fig. 4.4b), implying that the residual is amorphous, presumably C like according to its black color. The La precursor gives approximately the expected weight loss, and La_2O_3 is obtained pure. Taking into account the stoichiometry of the mixed La-precursor/Zr-precursor to give $La_2Zr_2O_7$, it is easy to see that weight residual in the precursor decomposition is due to the residue obtained from the Zr-precursor alone.

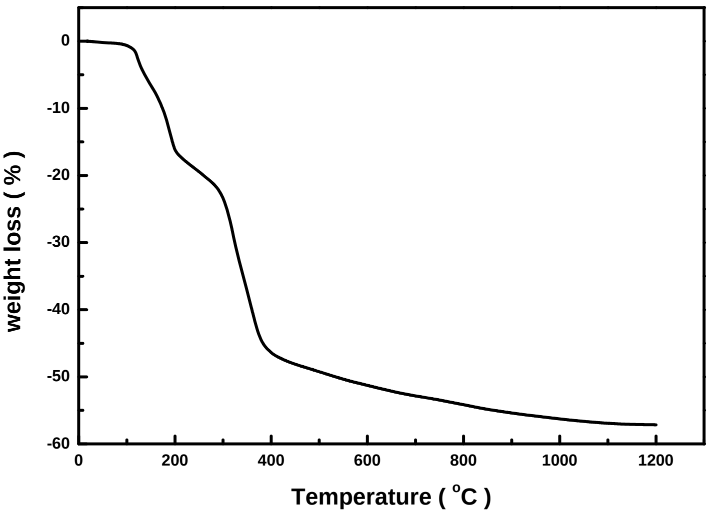

Fig. 4.1 TG analysis of precursor powder under Ar flow (heating rate of 10K/min)

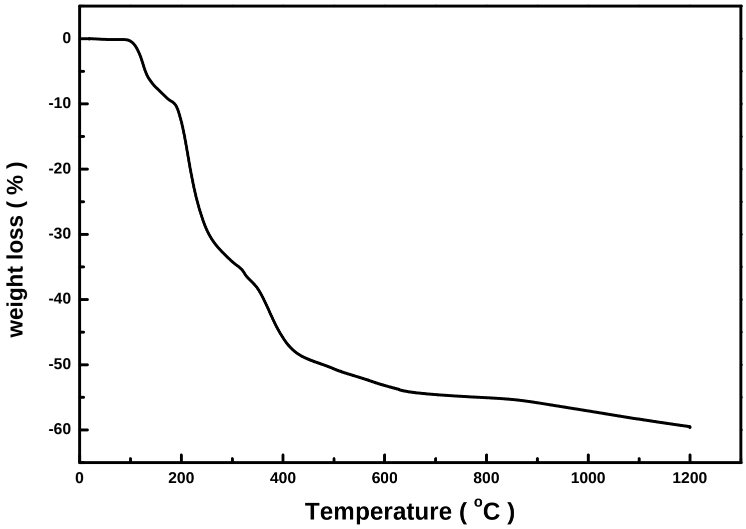

Fig. 4.2 TG analysis of mixed powder which is mixture of $La(acac)_3$ and $Zr(acac)_4$ under Ar flow (heating rate of 10K/min)

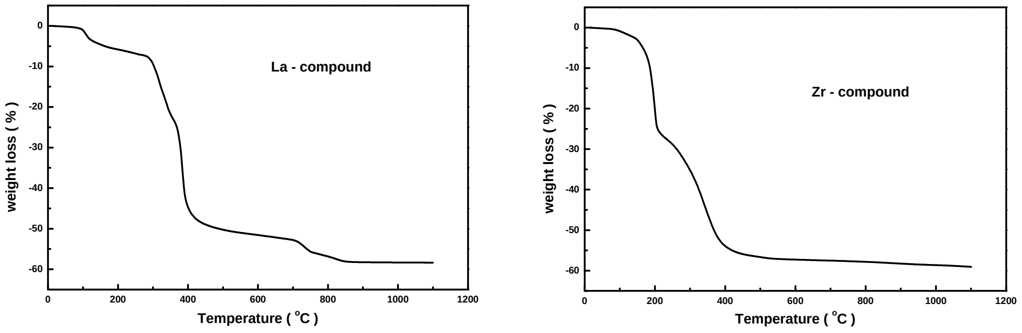

a b

Fig. 4.3 TG analysis of dried powders obtained by dissolving $La(acac)_3$ and $Zr(acac)_4$ respectively into propionic acid and drying the solution. The measurements are made under Ar flow. a: $La(acac)_3$ into propionic acid; b: $Zr(acac)_4$ into propionic acid

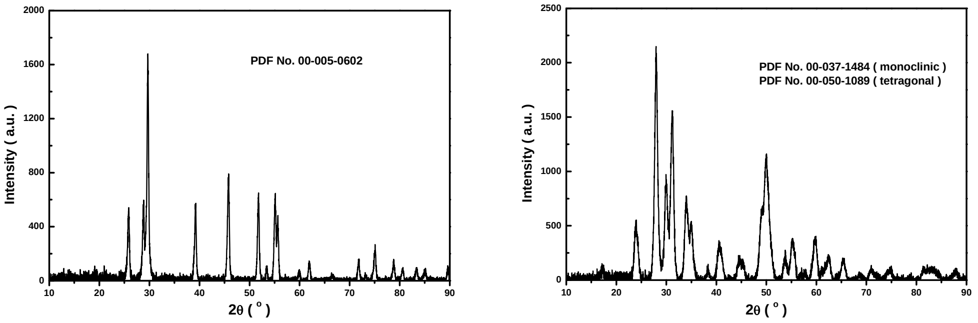

4.4a 4.4b

Fig. 4.4 XRD data of residual powder after TG experiment. a: residual powder of Lanthanum propionate after TG analysis. b: residual powder of zirconium propionate after TG analysis

4.3.1.3 Synthesis of LZO phase from the precursor solution

The precursor solution was dried at 80°C to remove all the solvent, the received powder is named the precursor powder. The precursor powder was heat treated under Ar-5%H_2 atmosphere at different temperatures (500°C, 700°C, 900°C, and 1100°C) for 30 min to be in similar conditions as those used in the preparation of the buffer layers. XRD data of the treated products are shown in Fig. 4.5. The first diffracted peak seen is observed at 28.6^o after annealing at 700°C, this peak is very broad, it corresponds to the most intense diffracted peak of LZO (222). With increasing the annealing temperature, several peaks appear, all indexed in the LZO unit cell. There is a small peak at 36.2^o observed after annealing at 1100°C, it is attributed to the (331) reflection of the pyrochlore phase. This result implies that the crystal structure of LZO powder has the pyrochlore structure when heated above 900°C. Below this, the structure adopted by LZO is fluorite, a disordered variant of the pyrochlore. No other crystallized phases were observed in this experiment.

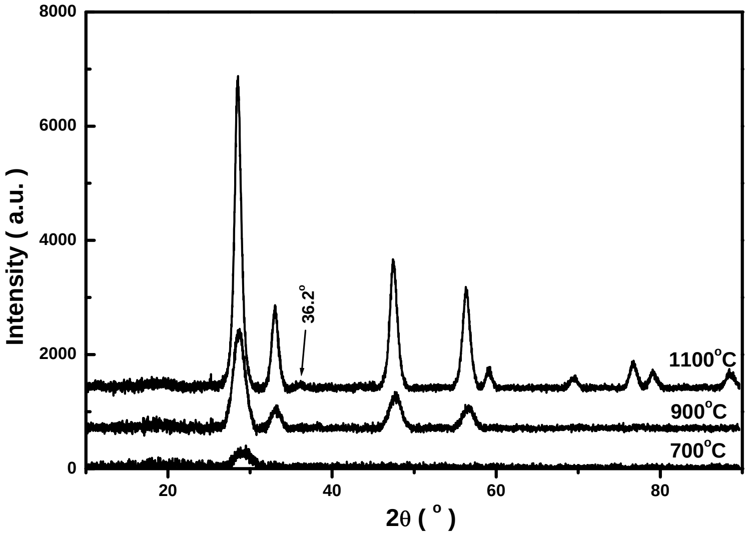

Fig. 4.5 XRD data of precursor powder after heat treatments

Table 4.2 shows the chemical analysis of the precursor powder after heat treatment at different temperatures. The theoretical weight fraction of propionate and LZO phase is also listed in table 4.2. The first evidence from this table concerns the precursor powder which composition is close to that of a propionate as already suggested before. The difference between the calculated value and the observed one might be explained by the presence of hydrated water in the La-precursor (1.78 water molecule per La(prop)3). This table also shows that the residue is C based, probably amorphous C, explaining the weight residue observed in TG analysis.

Table 4.2 composition of the precursor powder after treatment at different temperatures

Temperature	Weight fraction（wt%）				
	C	H	O	La	Zr
precursor powder	33.4	4.8	------	18.63	11.39
500°C	9.67	------	------	------	------
700°C	10.7	< 0.3	20.6	40.6	26.92
900°C	11.37	------	------	------	------
1100°C	11.99	< 0.3	18.92	41.76	25.38
$LaZr(prop)_7$	34	4.7	30.2	18.7	12.3
$La_2Zr_2O_7$	------	------	19.6	48.5	31.9

In order to know more about the synthesis of LZO, the precursor powder was also treated under oxygen atmosphere. XRD data of the precursor powder treated under oxygen atmosphere at 1100°C is shown in Fig. 4.6 and compared with data obtained under Ar – 5% H_2. It is clear that in pure oxygen the pure LZO phase is not obtained cannot be obtained as La_2O_3 and ZrO_2 impurities are found. Oxygen atmosphere changes the decomposition process of precursor powder, this has been studied by DT analysis.

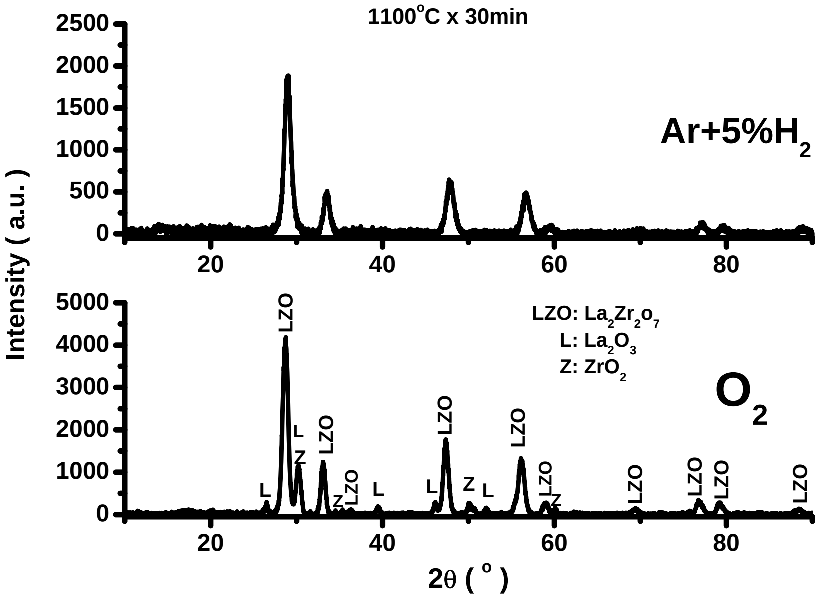

Fig. 4.6 XRD data of precursor powder treated under different atmospheres

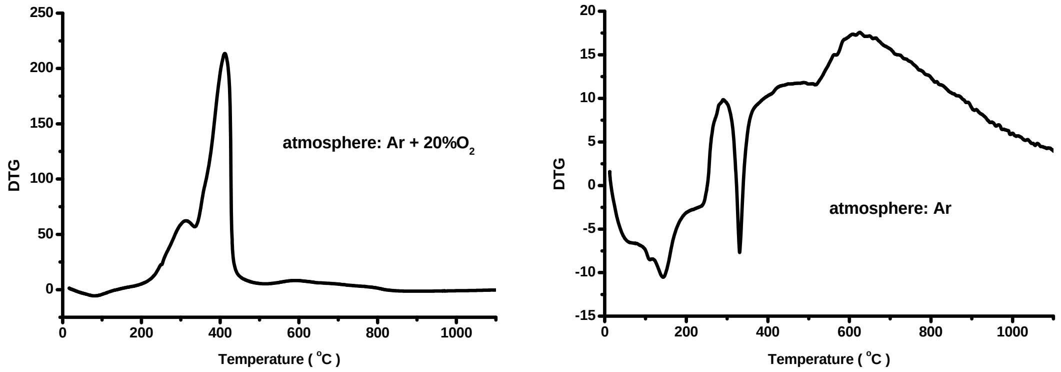

4.7a 4.7b

Fig. 4.7 DT anlysis of a precursor powder under different atmosphere.

a: Ar+20%O_2; b: Ar.

Fig.4.7 shows a DTA of the precursor powder under different atmospheres. A strong exothermic peak is observed at 400°C under Ar-20%O_2, it is replaced by an intense and fine endothermic peak under Ar, presumably due to the crystallization of ZrO_2. The strong exothermic peak under Ar-20%O_2 is the consequence of the burning of the precursor constituents under oxygenated atmosphere. It results in a non-uniform decomposition of the precursor powder with the formation of simple oxides like La_2O_3 and ZrO_2. In this case, LZO is formed by a solid-solid reaction ending up at a temperature higher than 1100°C, explaining why La_2O_3 and ZrO_2 are found in the residual powder when oxygenated atmosphere is used. So it is recommended to pyrolyse the precursor under a low oxygen atmosphere.

4.3.2 Deposition of LZO film on constantan substrate by CSD

4.3.2.1 Influences of annealing temperature

Because of the moderate annealing temperature required for the synthesis of LZO by CSD, it is possible to deposit LZO film on Cu-based substrate. So cube-textured constantan substrate was used. The constantan substrates[26] were spin-coated by the precursor solution with a concentration of 0.1 mol/l (with respect to La^{3+}), and then heat treated at different temperature for 30min. XRD (θ-2θ scans) are shown in Fig. 4.8. The LZO phase diffracts only if the annealing temperature is higher than 800°C, the intensity of LZO peaks increase with the annealing temperature. The diffraction of (222) planes at 28.6° is absent pointing to a c-axis orientation. A (222) pole figure of LZO film treated at 1100°C shows that the texture of LZO films is a cube with $<200>_{LZO}//<220>_{constantan}$.

In order for the texture of the oxide film to inherit the texture of the substrate, thermal stability of substrate' texture is often considered as a necessity. The (111) pole figure of the substrate after annealing at 1100°C , fig.4.10, shows that the substrate had recrystallised. This demonstrates that the nucleation of LZO layer has occurred at a temperature were the substrate's texture was still a cube one. Fig. 4.8 already showed that LZO was nucleated at 950°C, a temperature preserving the cube texture of the substrate. After being formed, this seed layer grows epitaxially, ignoring the behavior of the substrate. This important result implies that a cube-textured oxide layer can be formed on a metallic substrate provided that the substrate does not change its texture until the nucleation temperature of the oxide has been reached.

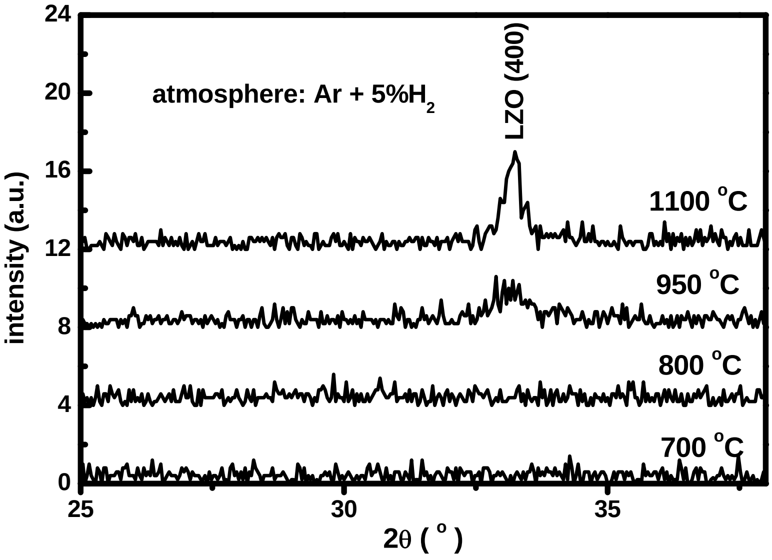

Fig. 4.8 θ-2θ scan of LZO films treated at different temperatures

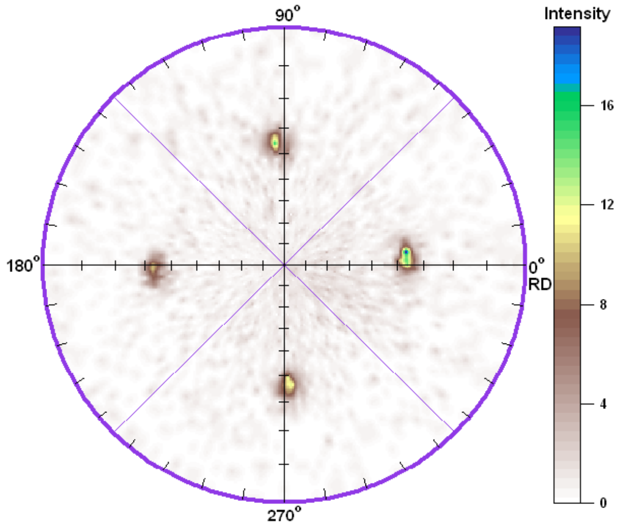

Fig. 4.9 (222) pole figure of a LZO film treated at 1100°C

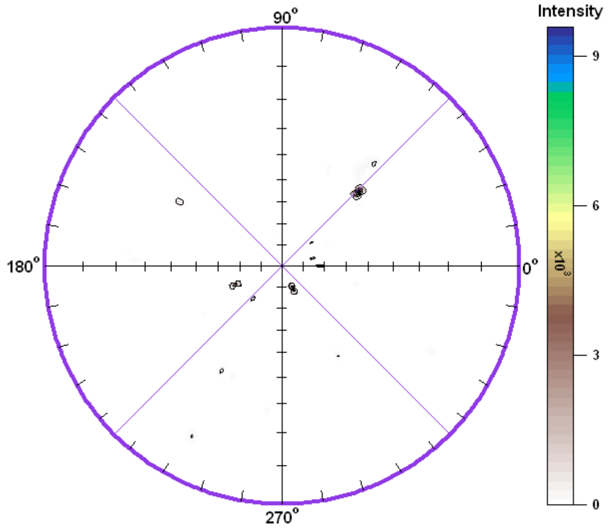

Fig 4.10 (111) pole figure of sample's substrate treated at 1100°C

4.3.2.2 Influence of the precursor concentration's in the solution

Fig. 4.11 shows θ-2θ scans of LZO film synthesized by precursor solutions having different concentrations. The intensity of $(400)_{LZO}$ peak increases with increasing concentration, but the (222) peak appears for concentrations larger than 0.1 mol/l. However, the (222) pole figure, Fig. 4.12, proves that the main component of the texture is cube. Comparing Fig. 4.12 and Fig. 4.9 makes clear that randomly oriented grains have grown for the concentrated precursors.

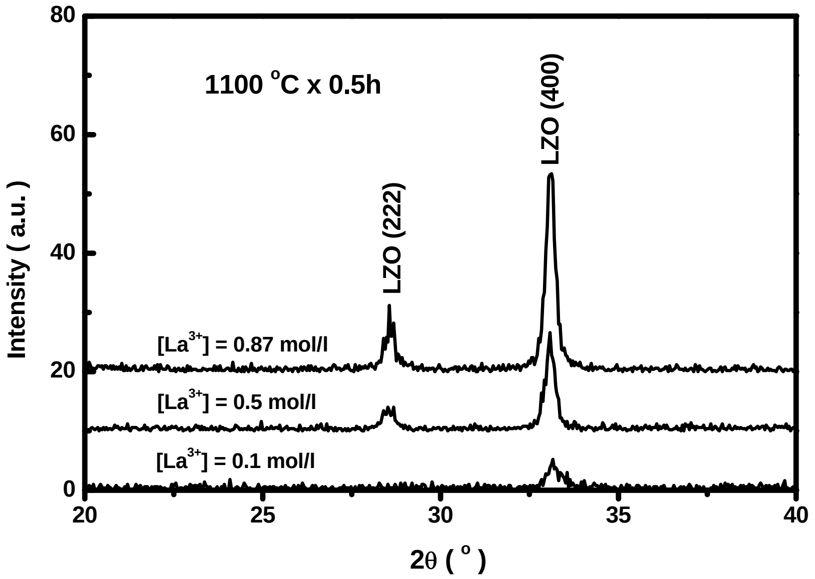

Fig. 4.11 θ-2θ scans of LZO films prepared with different concentrations of the precursor solutions

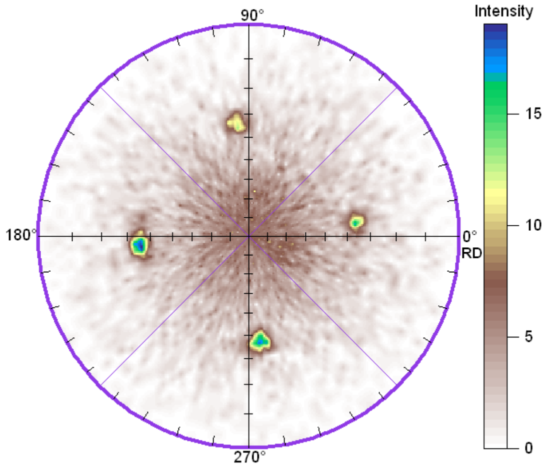

Fig. 4.12 (222) pole figure of LZO film for concentrated solution (0.87mol/l)

Because the annealing temperature is very much lower than the melting temperature of LZO phase, the driving force of nucleation is very large. It implies that heterogeneous and homogenous nucleations can occur with almost equal probabilities. The homogeneous nucleation with random orientation may compete with epitaxial grains heterogeneously nucleated on the substrate. On an other hand, if the concentration is too high, randomly oriented nuclei (La based) could precipitate during drying, contributing to random LZO grow.

4.3.2.3 Influences of annealing time

Fig. 4.13 shows the influence of increasing heating time on the intensity of (400) and (222) diffraction peaks formed by a film deposited with a middle concentrated solution (0.5 mol/l with respect to La^{3+}) and heat treated at 1100°C. The intensity of $(400)_{LZO}$ peak increases obviously with increasing heating time for heating time smaller than 5 hours. In comparison, the (222) peak changes very little. The volume fraction of cube texture in LZO film increases with the heat treatment time if it is shorter than 5 hours. Beyond 5 hours, a reaction occurs contributing to a loss of intensity. Long heat-treatment induces opening of pores or voids in LZO film, which is shown Fig. 4.14. A beginning (<1 hr), the LZO film is smooth and uniform with no pores nor voids, but with increasing heating time several pores appear and grow. For heating time larger than 5 hours particles can be found on the surface. These particles could not be distinguished by EDS from the rest of the film.

These results show that the volume fraction of the cube texture in the LZO film increase with the heat treatment time, but another phenomena contributes to open porosities, to grow particles at the surface and modify the texture after 10 hrs.

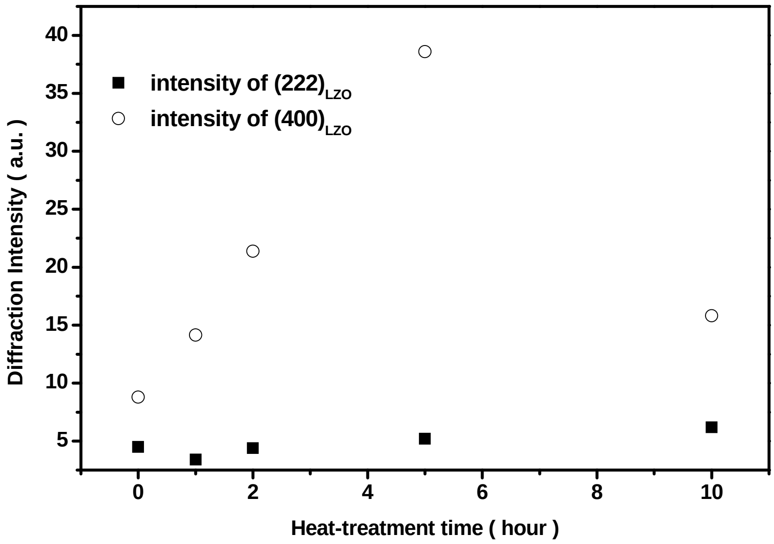

Fig. 4.13 Influence of heating time on texture of LZO films

At lower temperature, 950℃, influence of annealing time on the texture of LZO film is different, this shown on Fig. 4.15. It can be found that the intensity of (400) peak does not change too much while the intensity of (222) peak increase with annealing time.

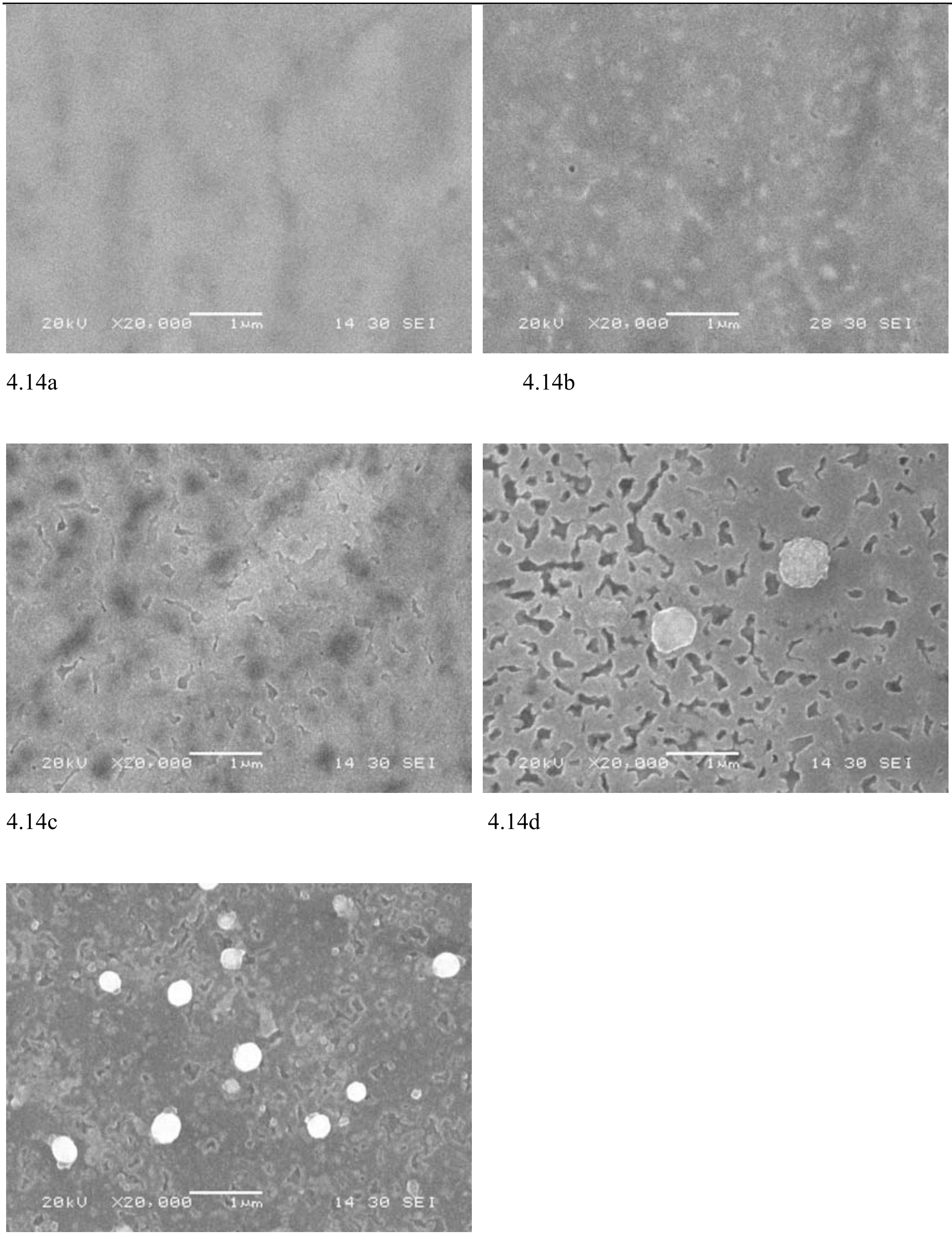

4.14a

4.14b

4.14c

4.14d

4.14e

Fig. 4.14 Influence of heating time on surface morphology of LZO films. The concentration of the solution was 0.5 mol/l (with respect to La3+) and the annealing temperature was 1100°C. a: 0 hr; b: 1 hr; c: 2 hr; d: 5 hr; e: 10 hr

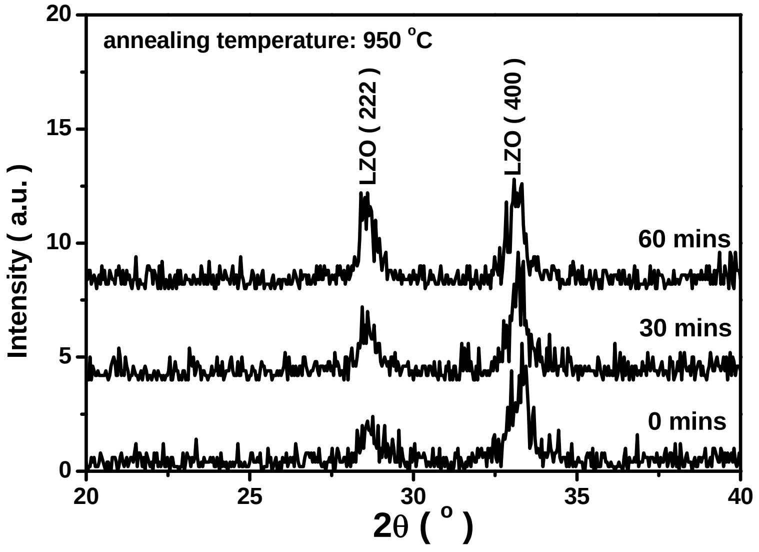

Fig. 4.15 Influence of heating time on the texture of LZO film, the annealing temperature is 950°C.

4.3.2.4 Influences of heating rate

The heating rate is also an important parameter of the heat-treatment, because the heating rate fixes the time spent in the low temperature range of the heat treatment, for example below 800°C. If the heating rate is very rapid, both pyrolysis and crystallization take place in the high temperature range. Slow heating rate is not good for epitaxial growth of LZO film, see Fig. 4.16.

The classical theory of nucleation tells that the free energy change is given by

$$\Delta G = -\frac{4\pi r^3}{3} \bullet \Delta\mu + 4\pi r^2 \gamma \qquad (4.1)$$

where r is the radius of a nuclei, Δμ is the free energy change for the formation of a nuclei of radius r , and γ represents the surface energy of a nuclei. So the critical radius of homogeneous nuclei is expressed by

$$r_c = {}^{2\gamma}\!/_{\Delta\mu} \qquad (4.2)$$

Based on expression 4.1 and 4.2, the homogeneous nucleation work can be expressed by

$$\Delta G_{homo} = -\frac{16\pi\gamma^3}{3\Delta\mu^2} \qquad (4.3)$$

In a similar way, the heterogenous nucleation work can be expressed by

$$\Delta G_{hete} = -\frac{16\pi r^3}{3\Delta\mu} \bullet \frac{(1-\cos\theta)^2(2+\cos\theta)}{4} \qquad (4.4)$$

where θ is a contact angle between nuclei and substrate. The expression 4.4 can be simplified by

$$\Delta G_{hete} = -\frac{16\pi r^3}{3\Delta\mu} \bullet f(\theta) \qquad (4.5)$$

where f(θ) is always lower than 1. A comparison of expression 4.5 and expression 4.3 shows that the heterogeneous nucleation takes place more easily.

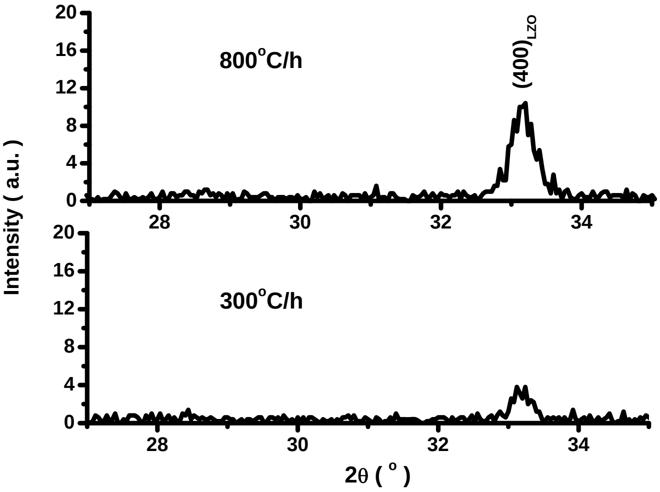

Fig. 4.16 Influence of heating rate on the texture of LZO film

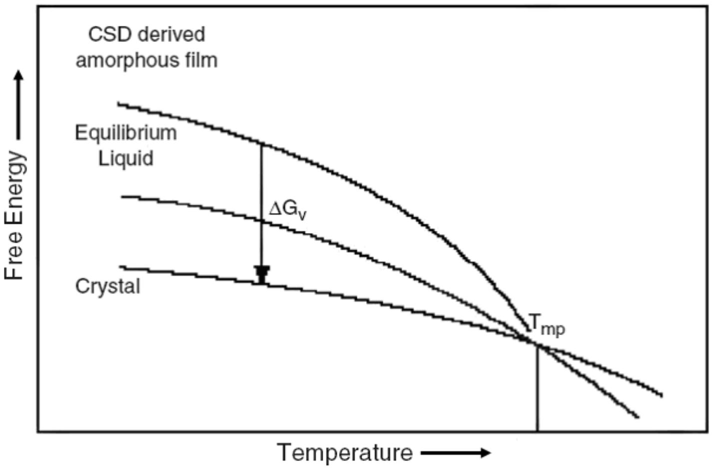

Fig. 4.17 Schematic diagram of the free energy change during CSD [94]

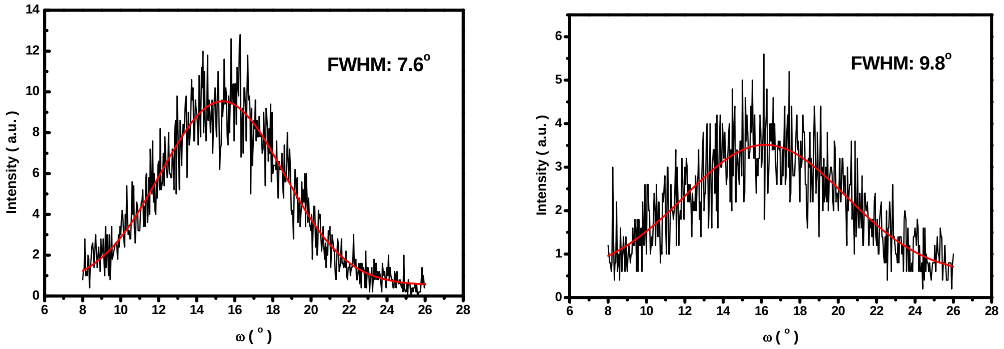

4.18a 4.18b

Fig. 4.18 Influence of heating rate on the sharpness of out-of-plane texture

a: 800° C/h; b: 300° C/h

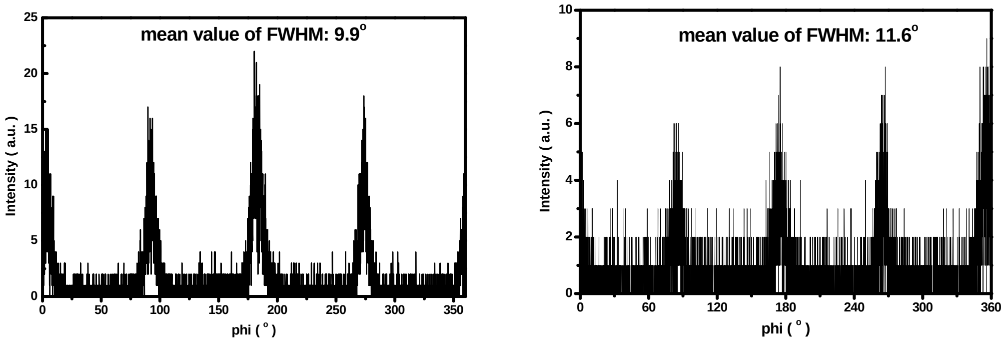

4.19a 4.19b

Fig. 4.19 Influence of heating rate on the sharpness of in-plane texture

a: 800°C/h; b: 300°C/h

The Gibbs free energy change during crystallization of LZO precursor film is represented schematically in Fig. 4.17[94]. For fast heating rate, the precursor film is heated rapidly to high temperature. Then the crystallization of the precursor film occurs in the high temperature range and according to Fig. 4.17, the free energy change is smaller. Consequently the driving force for nucleation gets smaller. Because the heterogeneous nucleation barrier is lower than that of homogeneous nucleation, the homogeneous nucleation will be less probable at high temperature. This analysis implies that a high heating rate is of benefit to increasing the volume fraction of cube texture in LZO film.

Fig. 4.16 shows the influence of heating rate on the θ-2θ scan for two samples, annealed at 1100°C for 30 min. It is obvious that the intensity of (400) peak increase with the heating rate, it is multiplied by 4 when the heating rate is increased from 300°C/h to 800°C/h.

High heating rates not only increase the volume fraction of cube texture in LZO film, but also the sharpness of its cube texture. Fig. 4.18 and Fig. 4.19 show this clearly. Increasing the heating rate from 300°C/h to 800°C/h improve the sharpness by 14 to 22% (14% for in plane and 22% for out of plane).

4.4 Summary

The precursor solution prepared by dissolving acetylacetonates into propionic acid is an efficient way for preparing a solution for depositing LZO film on a metallic substrate by CSD. Propionates are formed during this dissolution. The main residual impurity after heat treatment under Ar-5%H_2 is carbon. The atmosphere of the treatment influences the formation process of LZO powder.

The study of LZO films deposited on constantan substrate show that high annealing temperatures and high heating rates are benefic to increase the volume fraction of cube texture in LZO film. Increasing the heating time is efficient for increasing the volume fraction of cube texture in LZO film, but porosities appear after some time.

The substrate's texture must be stable up to the temperature range where the nucleation occurs. Recrystallization might occur above, it does not show detrimental effect on the growth.

The unsolved question of this study is the weakness of the intensity of LZO suggesting some absent nucleation sites and/or remaining amorphous phases. The aim of the next two parts is to increase the diffracted intensities.

Chapter V Modification of Surface Characteristics of Metallic Substrate by Sulfuration Process

5.1 Introduction

The results of the previous chapter show that the diffracted intensity of $La_2Zr_2O_7$ (LZO) film deposited on constantan substrate by CSD is small, and the texture of LZO film is not a pure cube one when the concentration of precursor solution is larger than 0.1 mol/l. Thus, in order to increase the crystalline fraction, even in thicker films, improvement of the epitaxial growth is necessary. But the different features of chemical bonding between metal and oxide makes this difficult. So we have considered modifying the metal/oxide interface. Ref. [61-63] showed that S element can be adsorbed on the surface of Ni substrate, and built a c(2×2)-S superstructure on its surface. This c(2×2)-S superstructure is very helpful to control the nucleation of the oxide layer deposited on Ni. Several authors[64,65] thought that, due to similar chemical properties of O and S, this c(2×2)-S over layer could become a template for nucleating the oxide film and controlling its texture. According to this analysis, sulfuration to form a c(2×2) superstructure on a metallic substrate may be a good method to modify the metal/oxide interface, and improve the epitaxial growth of LZO film on a metallic substrate.

Recent articles[64,65], have just discussed the influence of c(2×2)-S superstructure on the texture of an oxide layer in the case where it is deposited by a physical vapor deposition process, involving a sulfuration step using ultra-high vacuum. Ultra high vacuum ensure clean surface conditions of the substrate and enable to control the coverage at a precision of one sulfur monolayer. But in our case, the atmosphere of CSD is air, neutral or a reducing atmosphere but at ambient pressure, then the surface is not so well controlled and could contain other adsorbents than sulfur. No studies aimed to investigate if this could influences the c(2x2)-S superstructure and the texture after nucleation of the oxide layer by CSD.

In this chapter, the ways to obtain a c(2×2)-S superstructure on a metallic substrate by a simple process is discussed first, and then it is studied how the c(2×2)-S superstructure influences the epitaxial growth of an oxide layer deposited by CSD at ambient pressure.

5.2 Summarizing S absorption knowledge

Many results[61-63] show that H_2S is dissociated on clean Ni(100) surface with S adsorption and H desorption for temperatures larger than 200 K. When several layers of S are adsorbed, the first one is chemisorbed while the others are only physisorbed, the desorption of these layers is easier and may be done thermally above 1000 K, conversely the chemisorbed layer is stable up to 1200 K.

The different adsorption mode also induces different structures for each sulfur layers. In the first layer, S atoms occupy the four-fold sites on the Ni substrate's surface, and the sulfur monolayer can exist as a p(2x2) structure if the sulfur coverage is 0.25, or as a c(2x2) structure if the sulfur coverage is 0.5. Fig.5.1 shows the schematic diagram of c (2x2)-S superstructure and p (2x2)-S superstructure. The same references [61-63] also show that the form c(2x2) structure is a saturated one. When the concentration of adsorbed S exceeds the saturated one the excess S forms disordered layers.

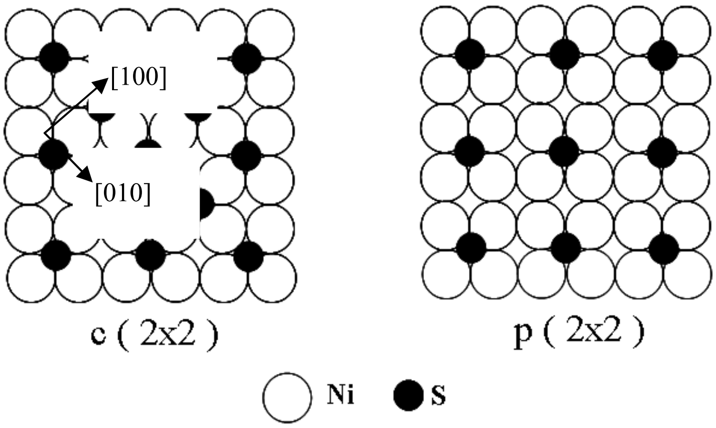

Fig. 5.1 Schematic diagram of c (2x2)-S superstructure and p (2x2)-S superstructure

According to the previous analysis, it is concluded that several layers of S can be adsorbed on a clean Ni surface. By thermal desorption, excess S can be removed down to the chemisorbed layer. This chemisorbed layer can be obtained by surface segregation of bulk residual S provided the right thermal profile has been applied. It is important to notice that, at first view, W (up to 5 at %) content does not substantially affect this result.

5.3 Experiments

Two sulfuration processes were designed, and tested on Ni-5 at% W substrate or constantan substrate. The processes are as follow: 1). the metallic substrates were annealed at 600°C for 20min under vacuum (pressure ~ 10^{-2}mbar). Then Ar - 0.1 % H_2S mixed gas was introduced into the furnace and the metallic substrates were annealed for another 10 min under the same gas and finally furnace cooled down to room temperature. After that, the samples were annealed at 850°C for 30 min under Ar - 5% H_2 to obtain the final samples; 2) The metallic substrates were annealed at 600°C for 30 min under vacuum (pressure ~ 10^{-2}mbar). Then the samples were quenched to room temperature under vacuum. Next, an Ar - 0.1% H_2S mixed gas was inserted into the furnace and the samples are exposed to this gas for 10min. Finally, the samples were annealed at 850℃ for 30 min under an Ar - 5% H_2 mixed gas.

These processes are shown on Fig. 5.2a and Fig.5.2b. These two processes involve two steps, adsorption of sulfur and modification of the sulfur content. The main difference between these two processes is the temperature of the substrate during adsorption of sulfur.

After sulfuration, all the samples were checked by Auger Electron Spectroscopy (AES) and Refection High-Energy Electron Diffraction (RHEED) to know information about their surface. During the measurement, the samples were annealed at 400°C under ultrahigh vacuum to remove the adsorbed contamination layer due to air exposure before AES and RHEED analyses.

In order to detect the influence of c(2x2)-S superstructure on the epitaxial growth of LZO film deposited by CSD, the texture of the deposited LZO was checked by XRD.

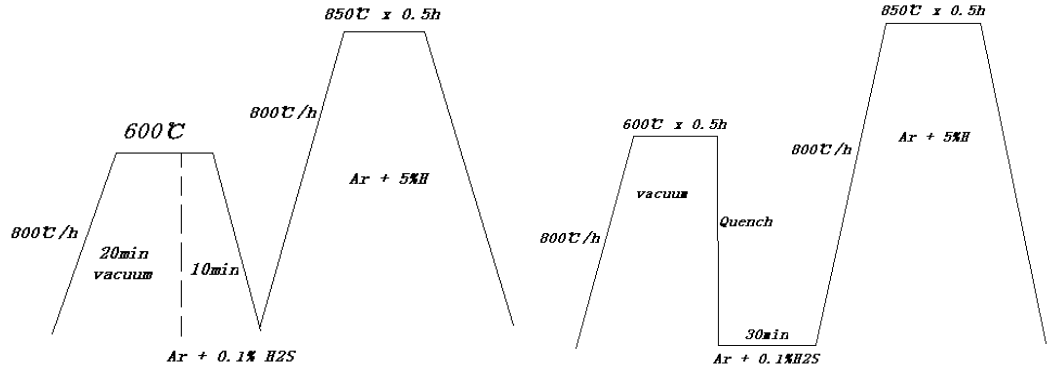

5.2a 5.2b

Fig. 5.2 Schematic diagram of sulfuration process. 5.2a: process I; 5.2b: process II

5.4 Results and Discussions

5.4.1 Sulfuration Process I

5.4.1.1 Sulfuration of Constantan Substrate

After sulfuration (process I), the surface color of the constantan was changed, it became black. This phenomenon implies that a new compound was formed on the sample's surface, identified as Cu_2S by XRD, Fig. 5.3. A further analysis shows that the texture of the constantan was also changed. Comparing Fig. 5.3 and diffracted data of constantan powder shows that the sample's surface orientation became random. Fig. 5.4 shows the morphology of sample's surface. The substrate which grain boundaries have disappeared is covered with a sulfite layer. Its thickness is large enough to make the underlying substrate invisible by XRD. It should be then in the range of several microns. To prove that the texture of the substrate was indeed unchanged, the sulfite layer was removed by polishing until the typical metallic color of constantan appears. XRD of the substrate, fig. 5.5 shows obviously the cube texture of constantan.

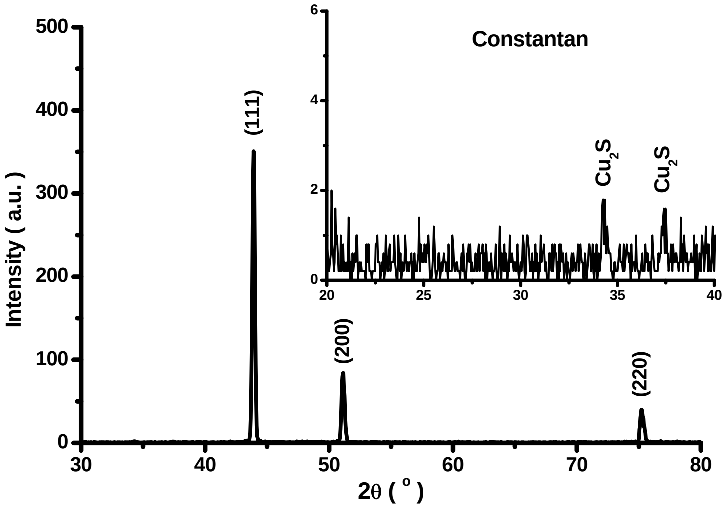

Fig. 5.3 θ-2θ scans of constantan substrate after sulfuration process I

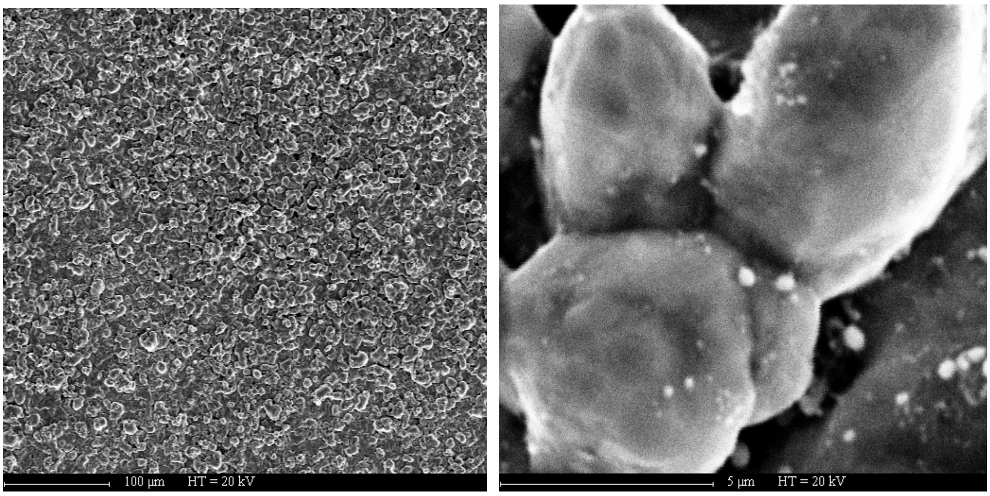

a： 200x b： 8000x

Fig. 5.4 Surface morphology of constantan substrate after sulfuration process I

The copper sulfite resulted from process I but it was unknown which step was responsible of the phases observed. The process I was then interrupted after the first step and analysed by XRD, fig.5.6. The results show that the larger peak is still (200), but with a shoulder attributed to $(200)_{Ni}$; in addition the diffracted peaks of Cu_2S and Ni_3S_2 are found in the angle range 20-42°. This result shows that the constantan substrate reacts with H_2S gas at 600°C but does not explain why Ni_3S_2 disappears during the second step of the process. A thermodynamic analysis can propose an explanation.

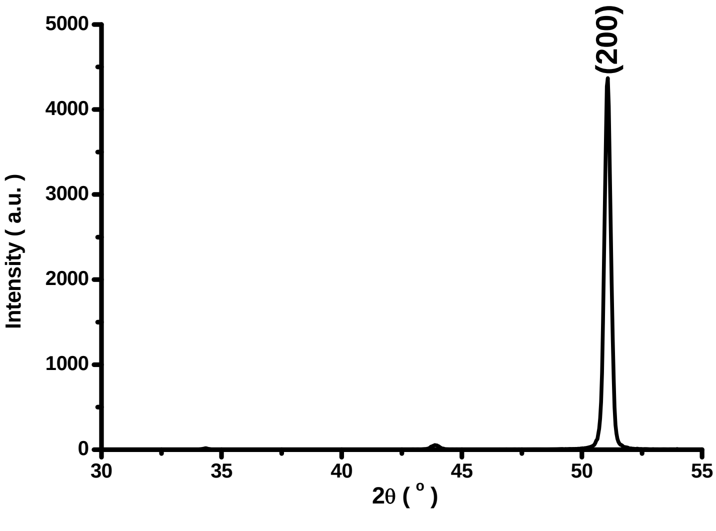

Fig. 5.5 θ-2θ scan of sample after removing the sulfite layer

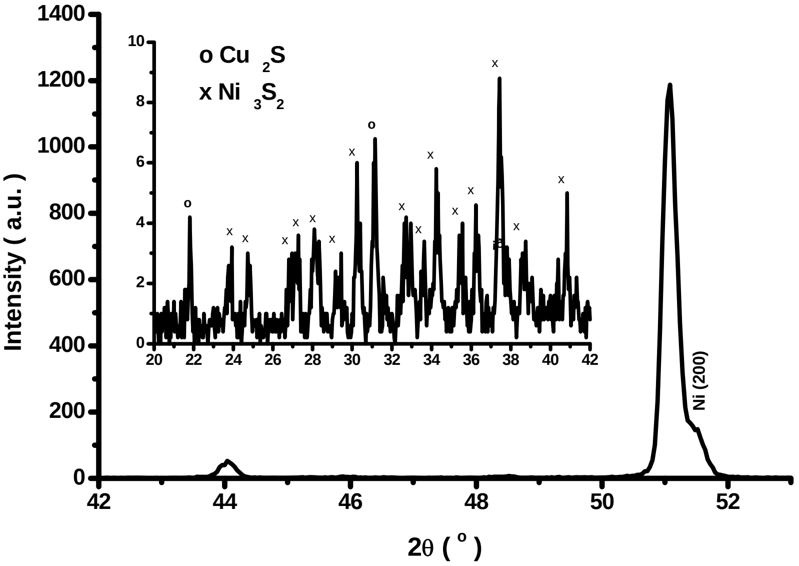

Fig. 5.6 θ-2θ scans of sample which underwent the first step of sulufration process I

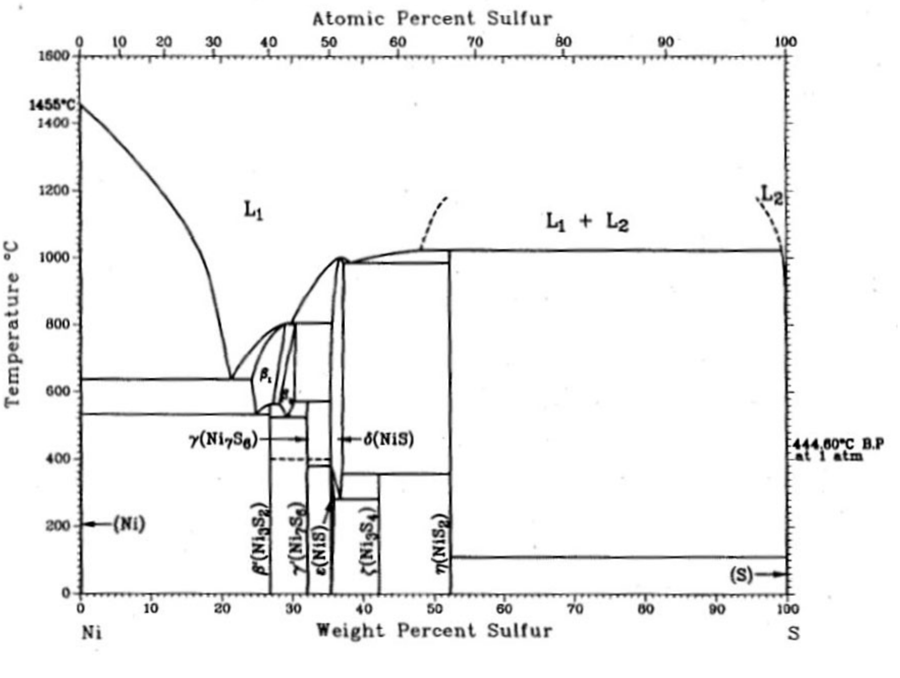

Fig. 5.7 Ni-S phase diagram

The reaction between Ni with S and one between Cu with S can be expressed by

$$3Ni + 2H_2S \rightarrow Ni_3S_2 + 2H_2 \qquad (1)$$

$$2Cu + H_2S \rightleftharpoons Cu_2S + H_2 \quad (2)$$

The free energy change of these two reactions can be expressed as follows

$$\Delta G_{Ni2S3} = \Delta G^{\theta} + RT\ln\left(\frac{P_H/P^{\theta}}{P_{H2S}/P^{\theta}}\right)^2 \quad (3)$$

$$\Delta G_{Cu2S} = \Delta G^{\theta} + RT\ln\left(\frac{P_H/P^{\theta}}{P_{H2S}/P^{\theta}}\right) \quad (4)$$

where ΔG^0s in expressions 3 and 4 are -22.775kcal/mol and -13.82kcal/mol respectively at 600°C. Before any treatment, the furnace system was pumped, and the pressure was lower than 10^{-2} mbar. Then the residual pressure of H_2 must be lower than 10^{-2} mbar. After introduction of the mixed gas of Ar-0.1 % H_2S, thermodynamic calculation showed that reaction 1 and 2 can take place spontaneously at 600°C. This explains why Cu_2S and Ni_3S_2 can be found after the first step of process I. In the second step, the samples are treated at 850°C, under Ar – 5% H_2. In this condition, the equilibrium pressure of H_2S for reaction 1 and 2 is $2.7x10^{-4}$ atm (0.27 mbar) and $4.8x10^{-5}$ atm ($4.8 x10^{-2}$ mbar), respectively. Because the furnace system was pumped to 10^{-2}mbar before starting the second step, the maximum residual pressure of H_2S should be lower than this and then much lower than the equilibrium pressure of reaction 1. So the inverse reaction of reaction 1 could take place during this second step. That is why Ni_3S_2 is not found on the surface of the substrate after the process. However, for reaction 2, the value of 10^{-2} mbar was very close to value of $4.8x10^{-5}$ atm, so inverse reaction of reaction 2 could, maybe, take place at the beginning of the second step, but this will raise the H_2S pressure and stop the inverse reaction. This justifies the unique presence of Cu_2S after the process.

This does not explain why the pure Ni contribution observed at the shoulder of Ni(200)constantan appears textured. The Ni-S phase diagram shown in Fig. 5.7 recalls that a eutectic exists between Ni and Ni_3S_2 and melts at 625°C. Because the samples are heated at 850℃ during the second step of the process I, the eutectic involving Ni and Ni_3S_2 will be melted. It is believed that during the reduction of Ni_3S_2, the recrystallisation of Ni occurs directly on the substrate and become textured by directional or epitaxial growth.

In summary, the constantan substrate reacts with Ar-0.1 % H_2S mixed gas at 600°C, Cu_2S and Ni_3S_2 are formed in the first step of sulfuration process I. During the second step of sulfuration process I, part of Cu_2S and all of Ni_3S_2 are be reduced. At same time, the melting of the eutectic formed between Ni and Ni_3S_2 favor the texture transfer to the superficial layer.

5.4.1.2 Sulfuration of Ni-5at%W substrate

The same study was reproduced on the Ni – 5 at % W. After sulfuration process I, the θ-2θ scan of sample is shown in Fig. 5.8. The diffracted peaks of Ni_3S_2 are well visible, and SEM photos show the surface morphology of the sample which is changed. The same analysis as previously explains the presence of Ni_3S_2 and the new surface morphology. This results shows that failure of the sulfuration process I is due to the formation of sulfites in Ar-0.1%H_2S at 600°C.

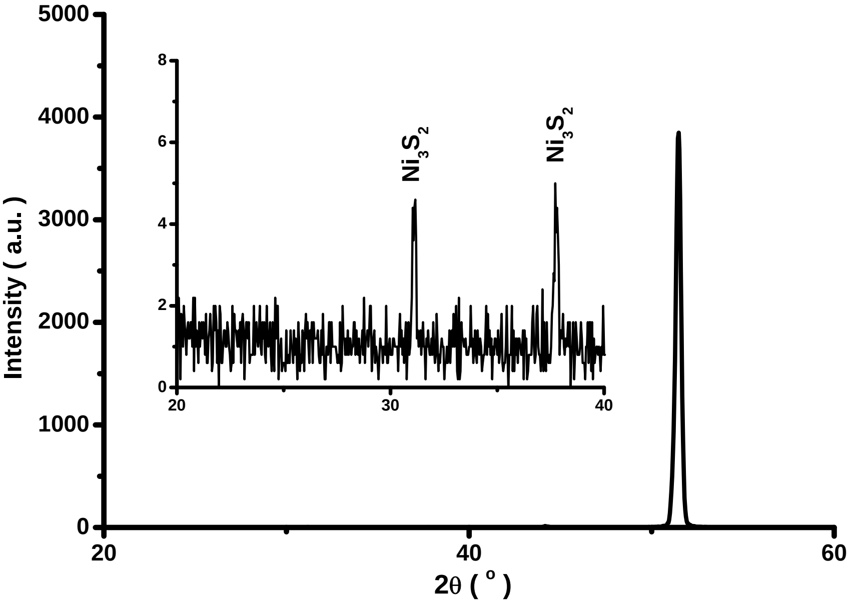

Fig. 5.8 θ-2θ scan of Ni-5at%W substrate after sulfuration process I

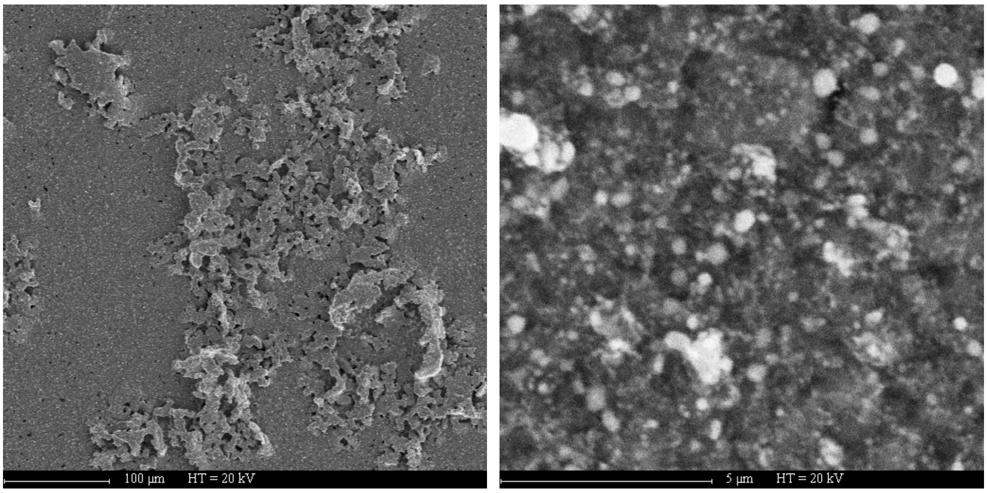

a： 200×

b： 8000×

Fig. 5.9 surface morphology of Ni-5at%W after sulfuration process I

5.4.2 Sulfuration process II

5.4.2.1 Sulfur deposition on Constantan Substrate

In this treatment, H2S is applied only at room temperature to avoid the sulfite formation. After applying the sulfuration process II, the sample was probed by XRD and the θ-2θ scan of sample is shown in Fig. 5.10. No diffracted peak of sulfites and no (111) peak of constantan are detected, the largest peak is $(200)_{constantan}$. It means that the sample's texture is not changed, and that sulfur adsorption at room temperature prevents the formation of sulfites.

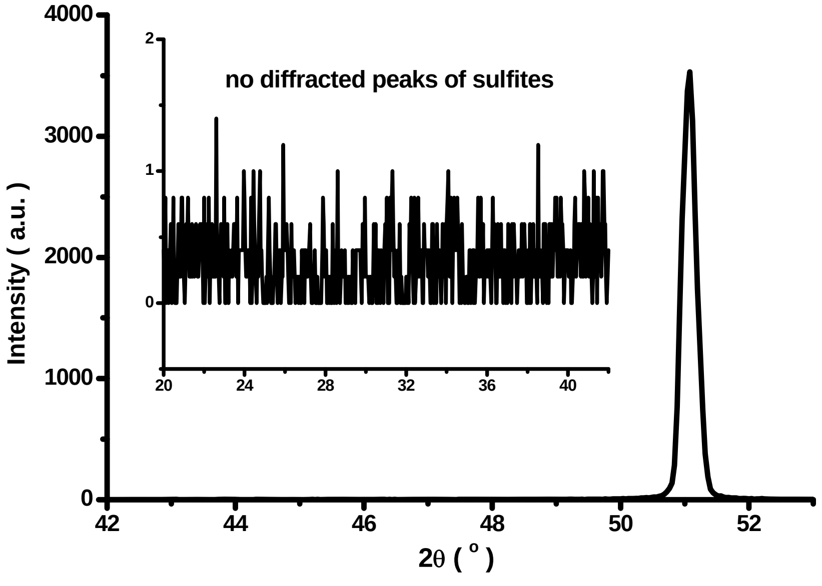

Fig. 5.10 θ-2θ scan of constantan after sulfuration by process II

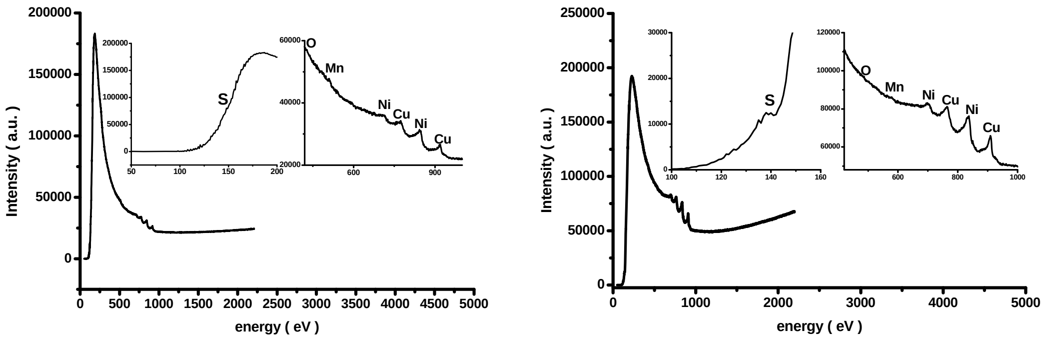

5.11a 5.11b

Fig. 5.11 AES before and after sulfuration by process II

a: before; b: after

XRD cannot have enough sensitivity to detect a few monolayer, so the sample was checked by Auger Electron Spectroscopy (AES) in order to know the composition of the superficial layer of sample where the thickness of layer only several nanometers or less. Fig. 5.11 shows AES data before and after sulfuration by process II. No sulfur can be found on the sample's surface before the sulfuration by process II. Conversely, sulfur is detected after the treatment of the sulfuration by process II. It means that sulfur was adsorbed on the sample's surface after this process. Unfortunately, it is impossible to obtain a clear RHEED pattern to prove the existence of a c(2x2)-S superstructure formed on the surface of constantan.

5.4.2.2 Sulfur deposit of Ni-5at%W substrate

After treatment of sulfuration by process II, θ-2θ scans and AES data of Ni-5at%W substrate were measured and are shown in Fig. 5.12 and Fig. 5.13, respectively. The sample's texture is not changed, and sulfur is adsorbed on the sample's surface.

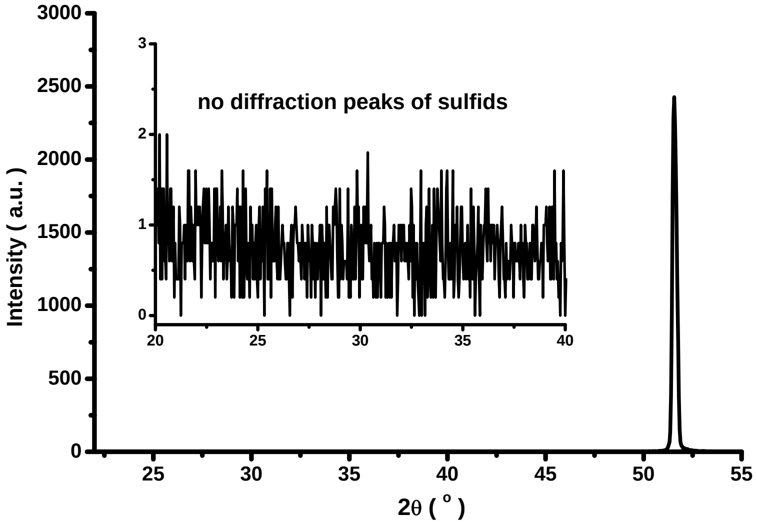

Fig. 5.12 θ-2θ scan of Ni-5at%W substrate after sulfuration by process II

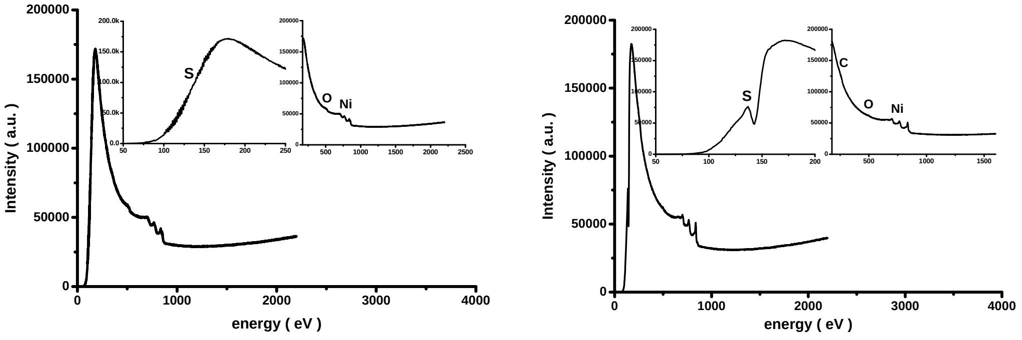

5.13a 5.13b

Fig. 5.13 AES of Ni-5at%W substrate before and after the treatment of sulfuration by process II

a: before; b: after

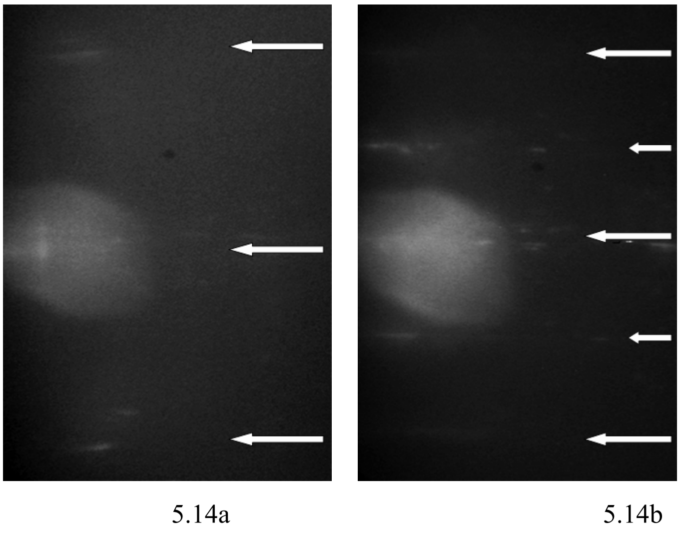

Fig. 5.14 RHEED patterns before and after sulfuration by process II. The incident direction of the electron beam is $<200>_{Ni}$ a: before; b: after

5.14a 5.14b

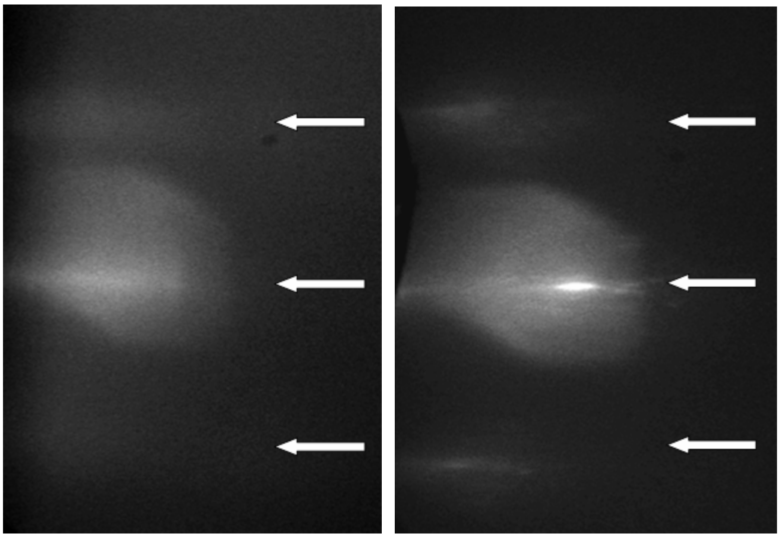

5.15a 5.15b

Fig. 5.15 RHEED patterns before and after sulfuration by process II. The incident direction of the electron beam is $<220>_{Ni}$. a: before; b: after

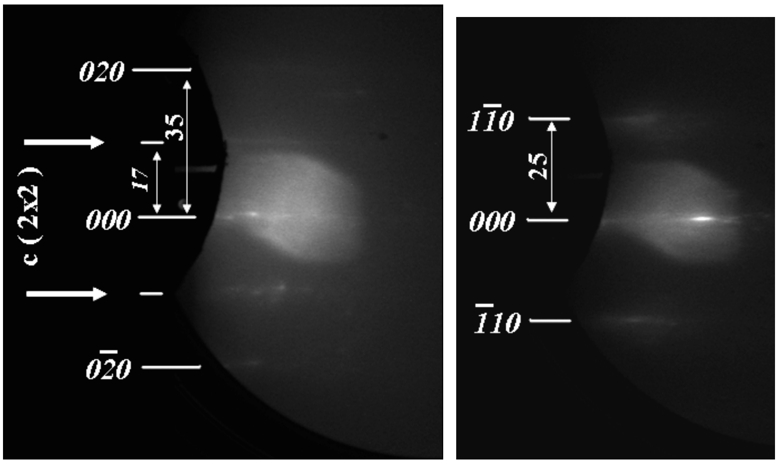

516a 5.16b

Fig. 5.16 RHEED pattern of sample after sulfuration by process II

a: the incident direction of electron beam is $<200>_{Ni}$ direction

b: the incident direction of electron beam is $<220>_{Ni}$ direction

The RHEED patterns of Ni-5at % W substrate before and after treatment of sulfuration by process II are shown in Fig. 5.14 and Fig. 5.15 respectively, the incident direction of the electron beam being $<200>_{Ni}$ in Fig. 5.14 and $<220>_{Ni}$ in Fig. 5.15. The distance between two adjacent diffracted streaks is deceased twice after sulfuration by process II in the $<200>_{Ni}$ direction. In contrast, no change is observed along the

<$220>_{Ni}$ direction. A further analysis shows that the distance between two diffracted streaks in Fig. 5.15b is 1.414 (√2) times the value measured in Fig. 5.14b. This is also shown in Fig. 5.16 on a better sample. This is exactly what is expected from the c(2x2)-S superstructure.

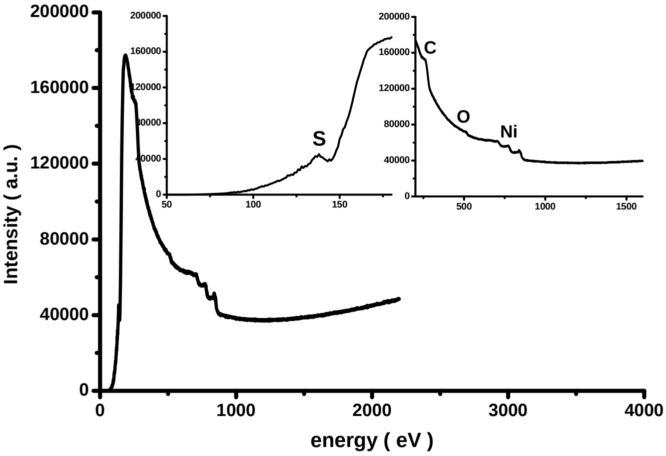

Fig. 5.17 AES data of sample treated by the first step of sulfuration process II

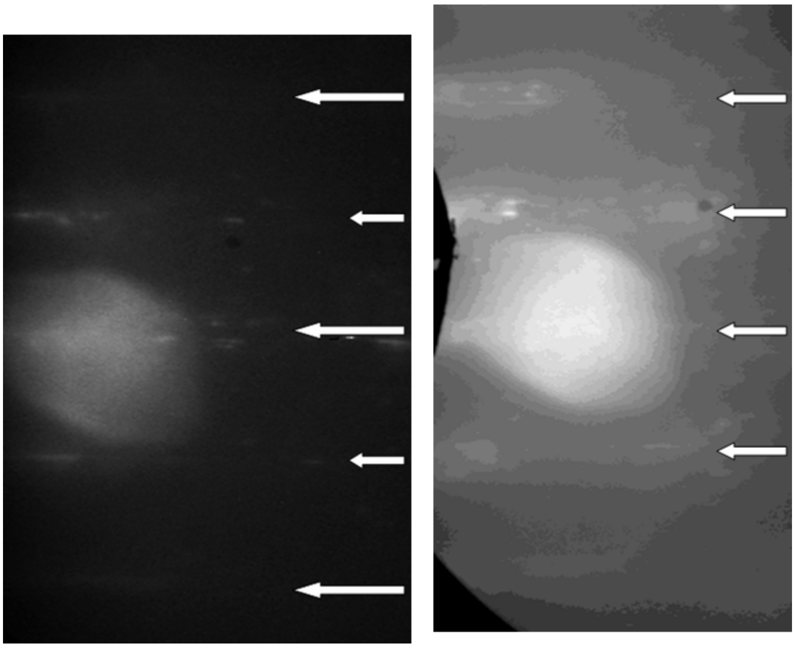

Fig. 5.18 RHEED patterns comparing a sample treated at 850°C (sample of Fig. 5.14b) with a sample treated at 700°C (sample of Fig. 5.17). RHEED in the direction $<200>_{Ni}$. On right hand side: sample treated at 700°C, left hand side: Fig. 5.14b

The results of fig. 5.14 and fig.5.15 show that the c(2x2)-superstructure is obtained after process II, but it does not tell the details of the layer formation. To know more about it, two additional experiments were done. First, a spectrum was measured after the first step of process II (after S adsorption), fig.5.17. S is well adsorbed on the surface. Then a similar sample was heat treated at an intermediate temperature of 700°C and observed by RHEED, fig. 5.18 (right hand part) where it is compared with the pattern obtained on a sample treated at 850°C (left hand part). The RHEED pattern shows weak and broad strikes in the former case compared to the very sharp strikes seen in the later case. This suggests a disordered structure for the sample treated at 700°C.

Based on the above results, the formation of the c(2x2)-S superstructure is as follows: after the vacuum treatment and exposition to Ar - 0.1% H_2S gas at room temperature, sulfur is adsorbed on the sample's surface. At this time, the S structure is disordered because of the excessive amount adsorbed. After the heat treatment at 850°C, the extra sulfur is desorbed, and the c(2×2)-S superstructure is obtained on a Ni-5 at% W substrate.

5.4.3 Influence of c(2x2)-S superstructure on the texture of LZO film deposited by CSD

Several experiments were done to evaluate the usefulness of the c(2x2)-S superstructure on Ni – 5 at% W as a template for the nucleation of LZO. A first result is shown in Fig. 5.19 where it can be found that the diffracted intensity is low, and a $(222)_{LZO}$ contribution is obvious. A further research shows that the bad texture was due to a non optimal heat treatment as it will be explained in the next chapter.

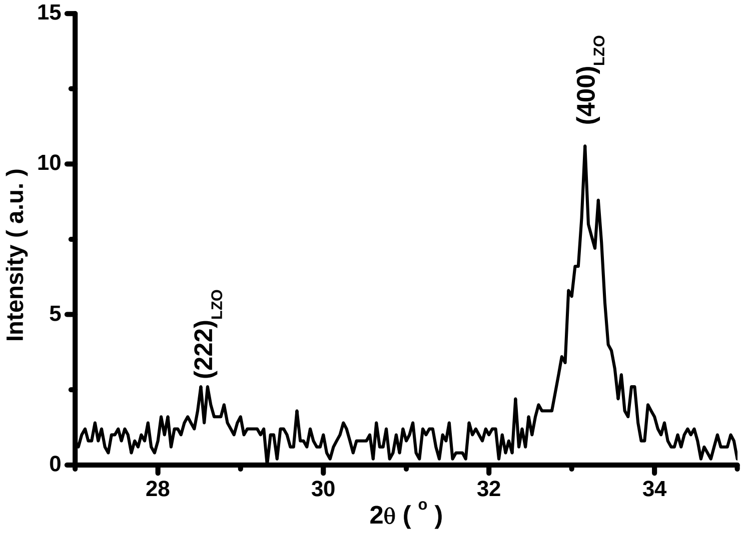

Fig. 5.19 θ-2θ scan of LZO film deposited on Ni-5at%W substrate with a c(2x2)-S superstructure, after a not optimized heat treatment.

After optimizing the heat treatment, LZO films deposited on Ni-5at%W substrate with the C(2x2)- S template or not were studied by XRD, Fig. 5.20, both showing an absence of $(222)_{LZO}$ diffraction. From this experiment it was not possible to conclude whether the template is efficient or not. Ref. [65] showed that c(2x2)-S superstructure can control the in-plane texture of buffer layer. So the ϕ (222) scan of a LZO film deposited on a substrate not covered with C(2x2)-S was done. The result is shown in Fig. 5.21 using a log scale to enhance possible parasitic orientations. It is clear that the texture of this LZO film is a pure cube texture. These first results do not show any influence (negative or positive) of the c(2x2)-S superstructure (fig.5.19 to 5.21).

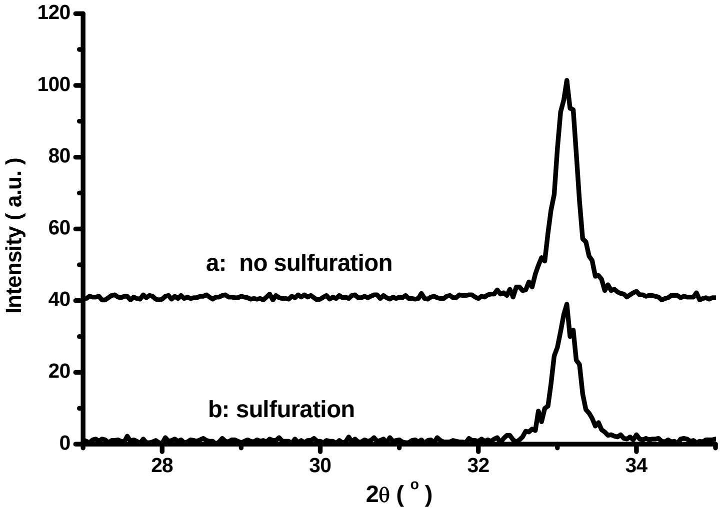

Fig. 5.20 θ-2θ scan of two LZO films deposited on Ni-5 at% W substrates with or without c(2x2)-S superstructure.

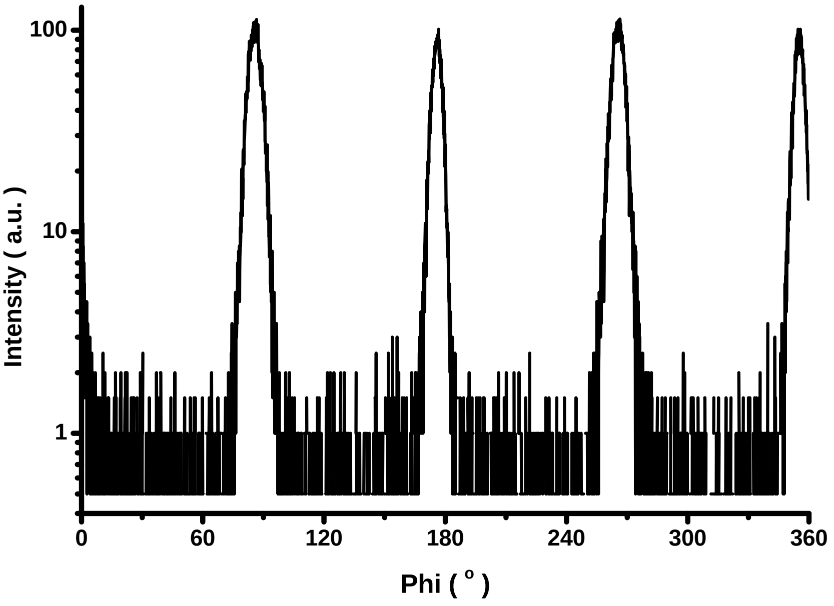

Fig. 5.21 ϕ(222) scan of a LZO film deposited on Ni-5at%W substrates without c(2x2)-S superstructure

However, the next experiment shows an influence of the c(2x2)-S superstructure. The experiment was conducted as follows: a Ni-5 at% W substrate, 2 cm long was cut along the longitudinal direction of another batch as that of the previous experiment. One part was sulfurated, the other was not. The substrates were covered with LZO by dip coating and heat treated in the same heat-treatment using the optimized process (see next chapter). After this, θ-2θ scans of the two LZO films were recorded and shown in Fig. 5.22.

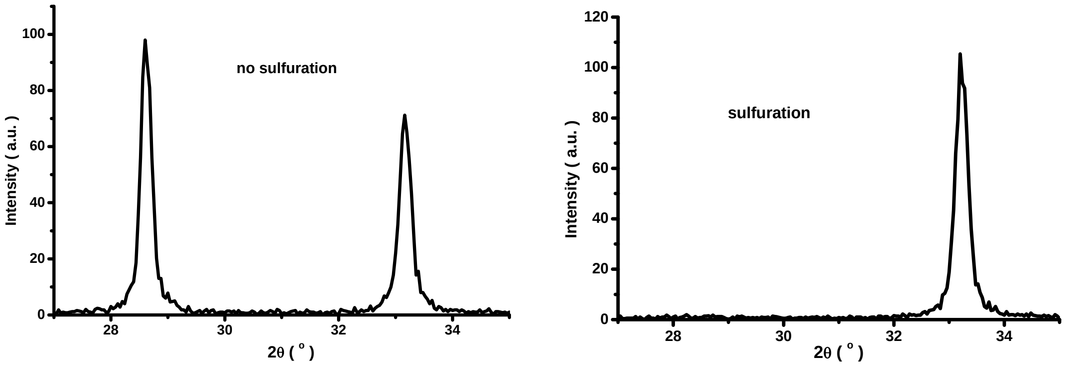

5.22a 5.22b

Fig. 5.22 θ-2θ scan of two LZO films deposited on parts of the same Ni-5 at% W tape with or without c(2x2)-S superstructure. a: no sulfuration; b: sulfuration

Summarizing these experiences: first, the c(2x2)S superstructure is not detrimental to the formation of cube textured LZO. Secondly, two behaviors have been observed for optimized treatments (see the next chapter that describes the optimization): i) the c(2x2)-S has no effect; ii) the c(2x2)-S is able to suppress wrong orientations ((222) for example). To comment these results, let us recall that crystallization is a process involving two different phenomena: nucleation and growth, nucleation is only concerned here. Heterogeneous nucleation on the substrate is at origin of the epitaxial growth enabling to transfer the texture of the substrate to that of the buffer layer. If the c(2x2)-S as an effect on crystallization, it will be will be on the nucleation. Considering the two different results, we are forced to conclude that two different substrates have been probed: those influenced by the c(2x2)-S and those who are not. We suggest that the difference is the existence or not of a c(2x2)-S layer at their surface. When it does not exist, it can be restored by the treatment proposed here. When it already exists, because the c(2x2)-S layer is at saturation, adding S will only add physically adsorbed layers that are removed during the annealing treatment. We underline that this layer may already exists because of segregation during cooling of bulk S contained in the Ni substrate, a phenomenon very well known to occur in this metal. However, this segregated layer may be damaged during the process of substrate preparation. Then, this sulfur treatment might be considered as a healing step restoring appropriate surface for nucleation of LZO.

5.5 Summary

Comparing with sulfuration process which was reported in references, the sulfuration by process II is an easy efficient sulfuration process, efficient at atmospheric pressure and compatible with CSD. The c(2x2)-S superstructure does not destroy the texture of LZO film deposited on Ni -5 at% W substrate. It is helpful to obtain a cube textured LZO film on Ni-5at%W substrate for optimized treatment. The function of c(2x2)-S superstructure is to control the orientation of initial LZO grains which nucleate on the surface of metallic substrate.

Chapter VI Improvement of Epitaxial Growth of $La_2Zr_2O_7$ Film on Metallic Substrate

6.1 Introduction

YBCO layer of coated conductors is deposited on a buffer layer by physical vapor deposition process (PVD), or chemical solution deposition process (CSD). So the texture of YBCO layer depends mainly on the texture and surface morphology of the buffer layer. It implies that the buffer layer transferring the texture from the substrate to YBCO layer has a prefect surface with a high volume fraction of cube texture and a well crystallized surface.

CSD processes can be divided into three basic steps, the first one is the preparation of the precursor solution, the second one is to deposit the precursor solution on the substrate, and the last one is the heat-treatment were the film is crystallized. It can be divided in two sub-steps, pyrolysis and crystallization. How to prepare the precursor solution has been detailed previously, so the content of this chapter is focused on the last steps of CSD process.

Crystallization of oxide films combines nucleation and growth process. The nucleation is a fast process, while the growth is a slow diffusion-controlled process. The limiting factors of these mechanisms must be identified. In order to crystallize the buffer layer with a high volume fraction of cube texture and with a well crystallized surface, the nucleation and growth must be controlled. In the previous chapter, the sulfuration process and its influences were discussed. Although the c(2x2)-S superstructure influences the orientation of nucleus on the metallic surface it cannot orientate the final texture of LZO film. How to improve the epitaxial growth of LZO film is a major topic of this chapter.

In this chapter, we analyze firstly the thermodynamics of the heat-treatment. Based on these analyses, the limiting step of growth of LZO film was identified and proved by experiments. After optimizing the heat-treatment, $La_2Zr_2O_7$ films with high volume fraction of cube texture and with crystallized surface was formed successfully by chemical solution process.

6.2 Experiments

After the metallic substrates were cleaned by acetone for 10 min in an ultrasonic bath, and were treated by sulfuration to obtain a c(2x2)-S superstructure on its' surface, they were covered by the precursor solution using spin-coating (rotation speed: 2500rpm, rotation time: 30s, acceleration: 3000rpm/min). After being spin-coated the samples were dried at 80°C for several minutes in air.

The standard heat-treatment of samples was as follows, the samples were heated at 950°C for 30 min under Ar - 5% H_2 atmosphere, in which the atmosphere pressure is a little larger than 1 atm with a heating rate of 800°C/h. Several parameters like oxygen partial pressure, gas speed flowing over the samples, and total pressure during the heat-treatment process were changed and compared with the parameters of standard heat-treatment.

The texture of all the samples was characterized by a XRD using a four-circle diffractometer (Siefert MZ IV using Xenocs multilayer optics with a horizontal divergence of 0.06^o and a spot size of 1×2 mm) working at the Cu Kα wave length and Electron Backscatter Diffraction (EBSD). The surface crystalline property was checked by Refection of High-Energy Electron Diffraction (RHEED).

Besides NiW and Ni/Cu bi-metallic substrate, $LaAlO_3$ (100) single crystals (LAO) were also chosen as substrates in some cases.

6.3 Results and Discussions

The θ-2θ diagram of a sample treated by a non optimized treatment was shown fig.5.19. The diffracted intensity was very low and the (222) peak was obvious. It implies that the texture of this LZO film was not a pure cube texture. It also implies also that the c(2x2)-S superstructure can only influence the orientation of nucleus of LZO on the metallic substrate, and cannot influence the finial texture of the LZO film. In order to obtain a LZO film containing a high volume fraction of cube texture and with a well crystallized surface, the heat-treatment process must be optimized. Before that, the limiting factors of LZO growth must be found.

6.3.1 Thermodynamic analyses about the pyrolysis of precursor film

Ref.[96] detected residual carbon in CeO_2 film deposited by CSD, and suggested that this residual carbon inhibits the growth of CeO_2 grains. Such effect was also observed in Si grown from sol-gel and then it is a rather general phenomenon. A chemical analysis of the powders which were obtained by heating the precursor powder at different temperatures showed that the main impurity was carbon (see Table 4.2 in Chapter IV). So it is reasonable to think that this residual carbon will also inhibits the growth of LZO grains. This residual C could result of an incomplete pyrolysis, however this is not consistent with thermal weight analyses (see chap IV) and it is believed that another reason may explain the carbon deposition.

Carbon deposition is an important phenomenon in catalysis, which is one of the reasons for catalyst lost activity. Ref.[129] showed that the reactions resulting in carbon deposition can be expressed by

$$CO + H_2 \rightarrow C + H_2O \qquad (6.1)$$

$$2CO \rightarrow C + CO_2 \qquad (6.2)$$

$$CH_4 \rightarrow C + 2H_2 \qquad (6.3)$$

This is the case in Ni/Al_2O_3 supported catalyst used in the partial oxidation of methane to produce syngas. It is believed that the same phenomenon can explain the amount of residual carbon measured in Table 4.2.

Let us consider the thermodynamic stability of CO gas first. According to reaction 6.1, CO will be reduced if

$$\frac{P_{H_2O} / P^{\vartheta}}{P_{co} / P^{\vartheta} \bullet P_H / P^{\vartheta}} < \exp(-\frac{\Delta G^{\vartheta}}{RT}) \qquad (6.4)$$

where ΔG^{θ} is the standard Gibbs free energy for reaction 6.1, and P_i is the partial pressure of the considered specie. At 500°C, the value of ΔG^{θ} is -5.953kcal/mol, and taking into account the concentration of hydrogen in the gas phase (5%), the limiting ratio for P_{CO}/P_{H2O} is

$P_{CO}/P_{H2O} = 1/2.4$ (6.5).

When P_{CO}/P_{H2O} is larger than this limit, then CO is in conditions to be reduced. In practical, the system was pumped to 10^{-2}mbar before heat-treatment, therefore the residual pressure of H_2O vapor was lower than 10^{-2}mbar. So the limit in eq 6.5 is easily reached and CO is in conditions to be reduced at 500°C. Taking into account the values of ΔG^{θ} at 700°C and 940°C (0.887kcal/mol and 9.106kcal/mol respectively), the Eq 6.5 become 32 and 1000 at 700 and 940°C respectively. These two values imply that reducing CO gas becomes more and more difficult with increasing temperature.

The reaction 6.2 which is also called Boudouard reaction takes place if expression 6.6

$$\ln\left(\frac{P_{co_2}}{P_{co}} \bullet \frac{P^{\vartheta}}{P_{co}}\right) < -\frac{\Delta G^{\vartheta}}{RT} \qquad (6.6)$$

is verified. The value of ΔG^{θ} is -70858.2J/mol at 500°C, so the value of the right-hand side of expression 6.6 is 11.02. Because of the reducing atmosphere used during the heat-treatment process, it is reasonable to assume that the partial pressure of CO is larger than that of CO_2. Based on this, the reaction 6.2 will take place if the value of P_{co}/P^{θ} is larger than $1.64x10^{-5}$. It is not difficult to prevent the reaction 6.2 from taking place. A similar analysis shows that the reaction 6.2 would take place if the value of P_{co}/P^{θ} were larger than 1 at 700°C or 4180 at 940°C. These results imply that it is impossible that the reaction 6.2 occurs at 700°C or 940°C.

A similar calculation shows that CH_4 gas would be decomposed at 500℃, 700℃ or 940℃ if the partial pressure of CH_4 were larger than 1.14 atm, $3.3x10^{-4}$atm, or 3.67×10^{-5}atm, respectively. The above-mentioned calculation implies that the cracking of CH_4 gas becomes more and easier with increasing temperature.

To summarize, all these results show that the main reason of carbon deposition is due to reaction of CO with H_2 and to thermal decomposition of CO and during the low temperature stage, and decomposition of CH_4 during the high temperature stage.

6.3.2 Control of the growth of LZO film

Because the residual carbon could affect the crystallization of the film[96], it must be eliminated to improve the crystallization of LZO film. From the results of the previous section, it is clear that the carbon deposition results from the decomposition of C-containing gaseous compounds. Two ways exists to decrease the amount of residual carbon: by increasing the oxygen partial pressure to prevent the C-containing gaseous compounds from decomposition (thermodynamic effect), or by increasing the flow speed of gas above the sample during the heat-treatment process to dissipate the C-containing gaseous compounds as soon as possible (kinetic effect). These two ways are very efficient when the substrate is a $LaAlO_3$ (100) single crystals (LAO). Figure 6.1 shows effects of both ways. The intensity of $(400)_{LZO}$ peak increases with increasing the flow speed of gas. When the atmosphere is static air, the intensity of $(400)_{LZO}$ peak becomes 5 times bigger. These results show the efficiency of these two ways very obviously.

One of the result of chapter IV (Fig. 4.6) shows that increasing the oxygen partial pressure is not beneficial for obtaining pure LZO powder. It seems to conflict with results in Fig. 6.1. However we must stress that it concerns powder formation and may be not used directly in film formation.

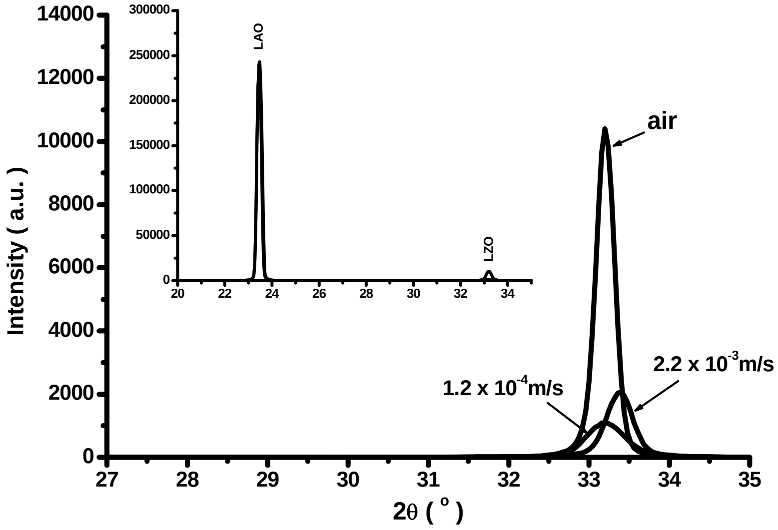

Fig. 6.1 θ-2θ scan of LZO films obtained on LAO single crystals

6.3.2.1 Influence of the gas speed on the growth of LZO film

In the experiments performed to study the effect of the gas speed, the configuration was as represented in fig. 6.2. Two alumina tubes with inner diameters of ϕ 7.2 mm or ϕ 40 mm were used, the maximum gas flux was fixed to 10 l/h, so the Reynolds number was considerably lower than 2000. Thus the flow was always laminar and the distribution of gas speed as a function of distance to the sample follows the equation

$$u = u_{\max}(1 - \frac{x^2}{r^2}) \qquad (6.7)$$

where u_{max} is the maximum value of the gas speed, equal to twice the average gas speed, x represents the distance from the center of the tube's inner cross-section to measuring point; r is the inner radius of tubes. The average gas speed was simply the flux of gas divided by the area of cross-section of the tube used to drive the gas.

The value of x is fixed and it is seven tenths that of r during experiments, so the gas speed flowing over the sample's center equals the average speed of the flow of gas. In the following, the average speed of gas was taken as a useful parameter.

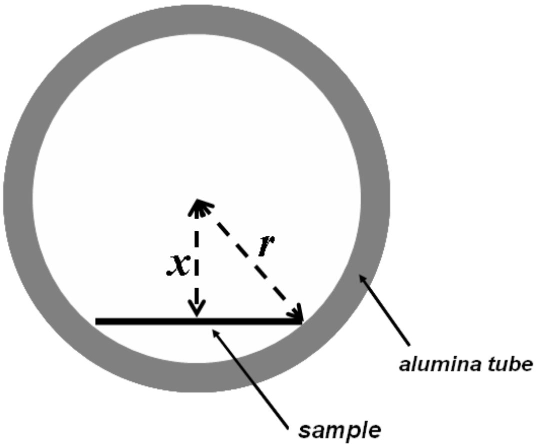

Fig. 6.2 Position of the sample in the alumina tube

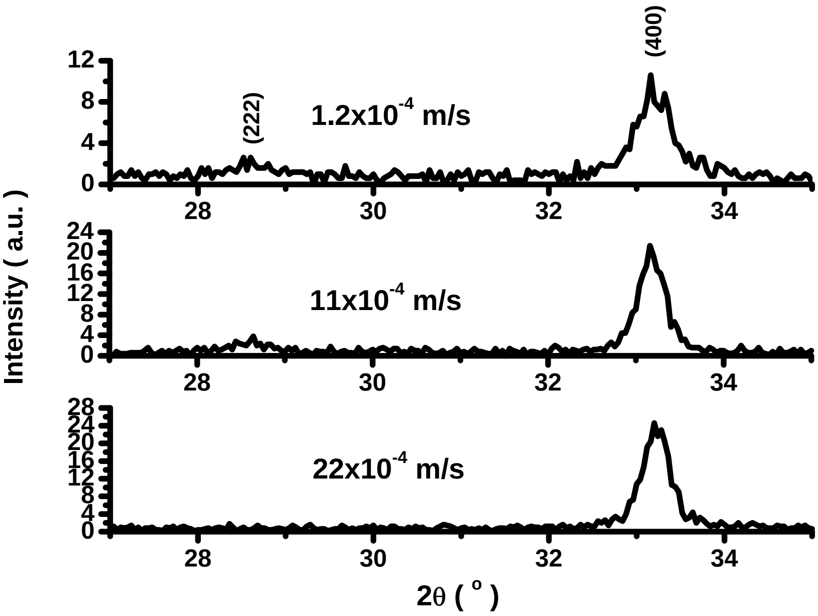

Fig. 6.3 θ-2θ scan of samples obtained under different speed of gas

Figure 6.3 and Fig. 6.4 show the effect of the average speed of gas on the diffracted intensity of LZO film. The intensity of (400) increases with increasing the average speed of gas, no (222) peak is detectable for average speed larger than 1.1x10^{-3} m/s. The results in Fig. 6.4 also shows an interesting relationship between the gas speed and the integral intensity of (400) peak of LZO film. The integral intensity of (400) peak is proportional to the logarithm of the gas speed. This is shown in the insert of Fig. 6.4. More experiments should be done to explain quantitatively this relationship in terms of kinetics of decomposition and of mass transfer.

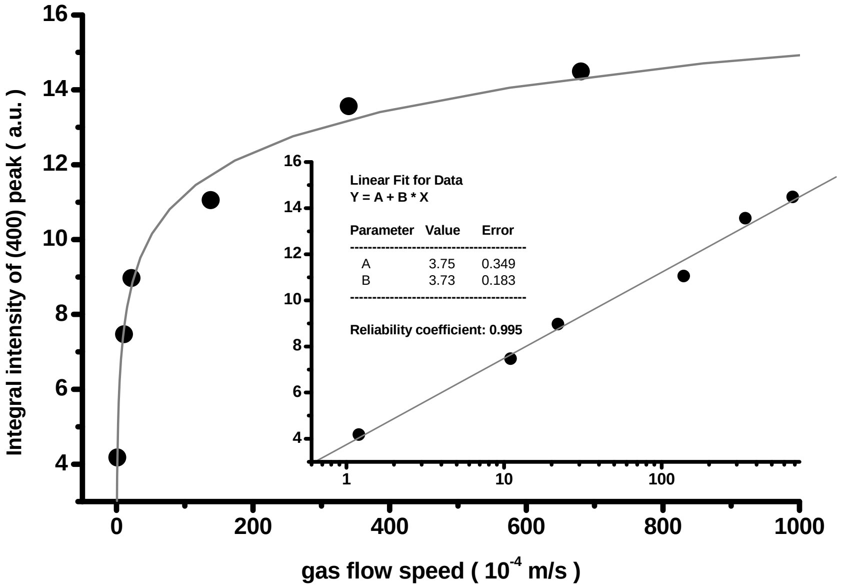

Fig. 6.4 Influence of gas speed on the integral intensity of $(400)_{LZO}$ peak

Based on XRD, in a polycrystalline material, all crystallographic faces {hkl} are related with a sphere in the reciprocal space. All points of the intersection between the Ewald sphere and the reciprocal sphere will lead to diffraction peaks, and the diffracted intensity distributes uniformly over this zone. However, in textured materials, the intersecting zone is composed of several separated regions where the diffracted intensity is concentrated. The sharper the texture is, the smaller the total area of these regions is. It implies that the measured intensity of (hkl) peak increase with the quality of texture. So an increase of the intensity of the (400) peak of LZO film implies that the volume fraction of the cube texture in LZO film increases.

According to the previous analysis, the amount of residual carbon in LZO film should decreased under large gas flow on the sample's surface, and this will favour the growth of LZO grains. But it cannot explain directly why the volume fraction of cube texture in LZO film increases with increasing the gas speed.

At beginning it must be commented why the (222) peak is observed in certain circumstances. It is admitted[94] that under cooling is very large in CSD derived films, and it should also be the case for LZO deposited films by CSD process. This induces a very large driving force for nucleation, and heterogeneous and homogenous nucleation can occur with comparable probabilities. Usually heterogeneous nucleation is easier than homogenous nucleation, so heterogeneous nucleation takes place first. If the grains nucleate heterogeneously on the biaxially textured substrate and grow rapidly, the texture of LZO film is expected to be epitaxial cube texture. But due to growth inhibitions, homogenous nucleation could become competitive and force the texture of LZO film to contain some random oriented. That is why the (222) peak can be found in θ-2θ scan curve. If a large gas speed is applied, the amount of residual carbon is reduced. Then the factor inhibiting the growth can be eliminated, and the grains developed from heterogeneous nucleation can grows enough rapidly. So a LZO film with high volume fraction of cube texture is obtained. Because slow gas speed ($<2.2\text{x}10^{-3}$ m/s) is inefficient to disperse the C-containing gaseous compounds, and much carbon will be retained in the film, the residual carbon will inhibit the epitaxial grins to grow and the unwanted random orientation can develop.

Table 6.1 Gas speed schedule

Switching temperature	20°C 650°C 850°C 950 °C
sample I (m/s)	--------------------------------$1.2\text{x}10^{-4}$---------------------------------
sample II (m/s)	----$2.2\text{x}10^{-3}$-----$1.2\text{x}10^{-4}$---
sample III (m/s)	-------------$2.2\text{x}10^{-3}$--------------------$1.2\text{x}10^{-4}$-----------------------
sample IV (m/s)	--------------------------------$2.2\text{x}10^{-3}$---------------------------------

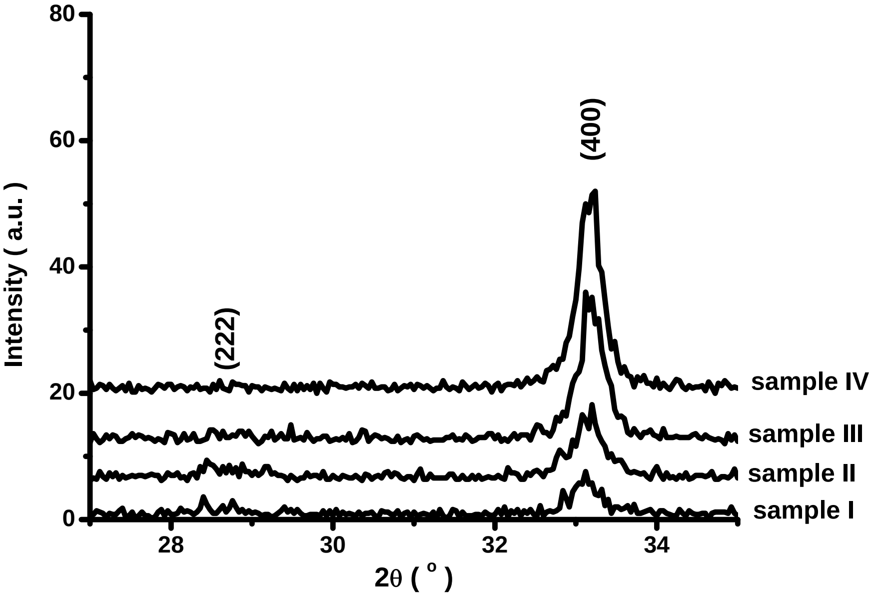

Fig. 6.5 Effect of changing the way to apply the gas flow (see table 6.1) on the texture of LZO films deposited on NiW.

In summary, increasing the gas speed enables the C-containing gaseous compounds to be dispersed as rapidly as possible and to decrease the amount of residual carbon. Because of that, the epitaxial cube-textured LZO layer could grow from the bottom to the top of film.

Based on TG analysis[92], it is clear that most of the C-containing gaseous compounds are formed below 500°C. Thus, at first view, the C-containing gaseous compounds must be dispersed in the low temperature part of the treatment. In order to prove it, four samples were prepared on NiW substrates. All four samples were annealed at 950°C for 30 min with the same annealing parameters, except that the gas speed was modified according to Table 6.1. For sample I, the gas speed was kept constant small ($1.2\text{x}10^{-4}$m/s) during all the processes. For sample II, the gas speed was fast ($2.2\text{x}10^{-3}$m/s) during the first part of the heating, i.e. up to 650°C and then slowed down to low speed (1.2×10^{-4}m/s). For sample III, the gas speed was kept constant fast ($2.2\text{x}10^{-3}$m/s) until 850°C. Sample IV was annealed under a constant fast gas speed ($2.2\text{x}10^{-3}$m/s) during all the heat treatment. XRD results are shown in Fig. 6.5. Comparing sample II and sample I, it can be observed that the ratio of I(400)/I(222) does not changed too much (from

3.2 to 3.4). It means the epitaxial growth of LZO film is not improved. It is believed that this is due to problems encountered in the decomposition of precursor. In a previous paper[92], result of TG analysis showed that the La-precursor decomposition extend up to 850°C. So the carbon deposition can still take place in the temperature range from 650°C to 850°C. Thus, decreasing the gas speed at 650°C is too early. When the switching temperature is 850°C, the intensity of (400) peak is increased with respect samples I and II. The (222) parasitic orientation is hardly found and the ratio of I(400)/I(222) is changed to 12.9. It implies that the epitaxial growth of LZO film is improved in this case. For sample IV, the ratio of I(400)/I(222) is increased wizardly to 101. All these results prove that dispersing the C-containing gaseous compounds is important to improve the epitaxial growth of LZO film.

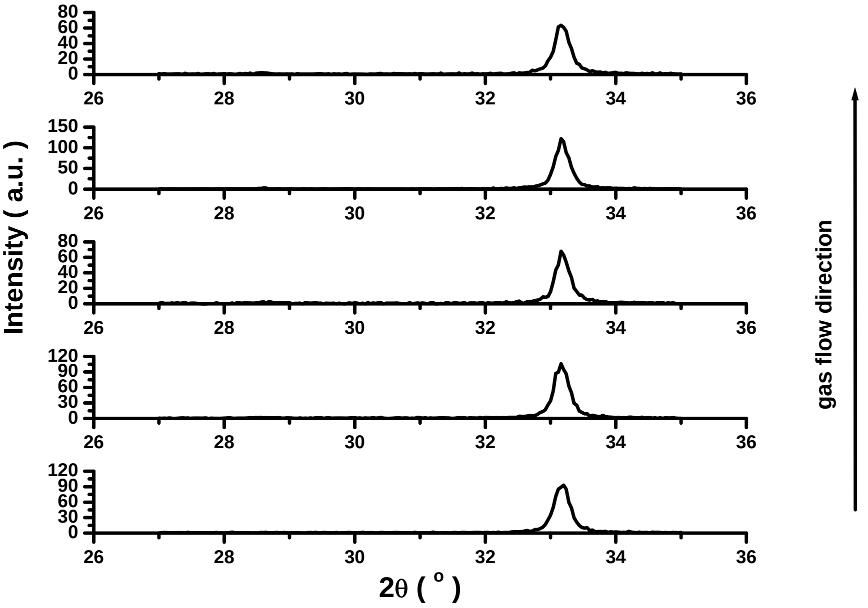

Fig. 6.6 θ-2θ diagrams of different parts of a sample flushed with the gas along its length

6.3.2.2 Effect of the gas flow direction

According to hydrodynamics, a boundary layer of C-containing specie should exist on the surface of LZO precursor film during pyrolysis under Ar+5%H_2 flow. This boundary layer always exists even for large gas speed. Increasing the gas speed can only decrease its thickness. The consequence is a probable non-uniform C distribution along the gas flow direction; it will induce a non-uniform LZO film.

Fig. 6.6 shows the θ-2θ diagrams of a sample flushed by the gas along its length of 2 cm. No (222) peak is found showing a good texture along the length of the sample. However, a plot of the ratio $I(400)_{LZO}/I(200)_{Ni}$ versus position, fig. 6.7 shows a non-uniformity of the LZO film. These results suggest that it would be better to flow the gas in the transverse direction to the sample.

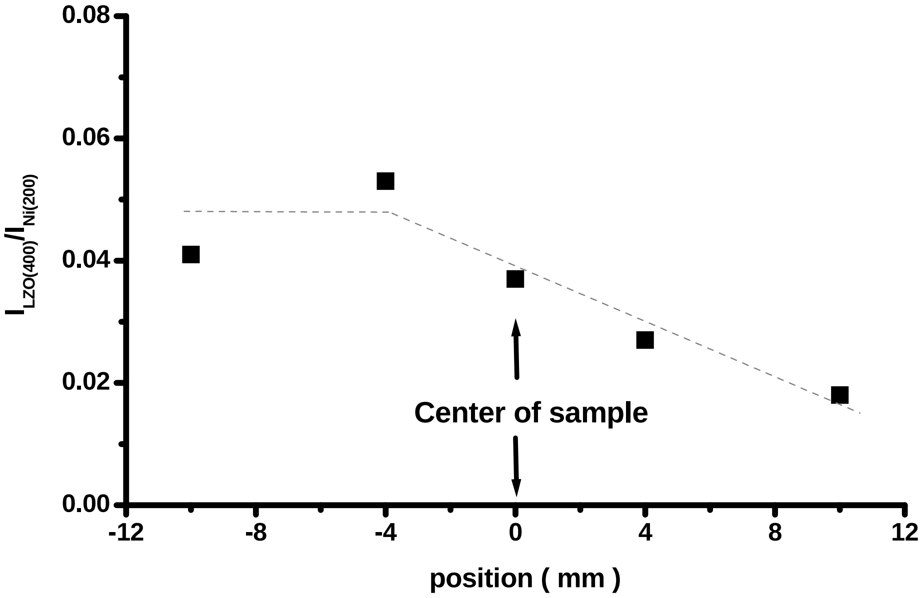

Fig. 6.7 $I(400)_{LZO}/I(200)_{Ni}$ versus position along the sample.

6.3.2.3 Influence of oxygen partial pressure on the growth of LZO film

In the previous section, the influences of the gas flow speed have been discussed. The idea, that the C-containing gaseous compounds are dispersed by a large flow speed of gas and reduce the amount of residual carbon in LZO film, comes a kinetic viewpoint. According to the analyses of the section 6-3-2, it is believed that increasing the oxygen partial pressure can also decrease the amount of residual carbon, in this section; we study the influence of the oxygen partial pressure on the growth of LZO film.

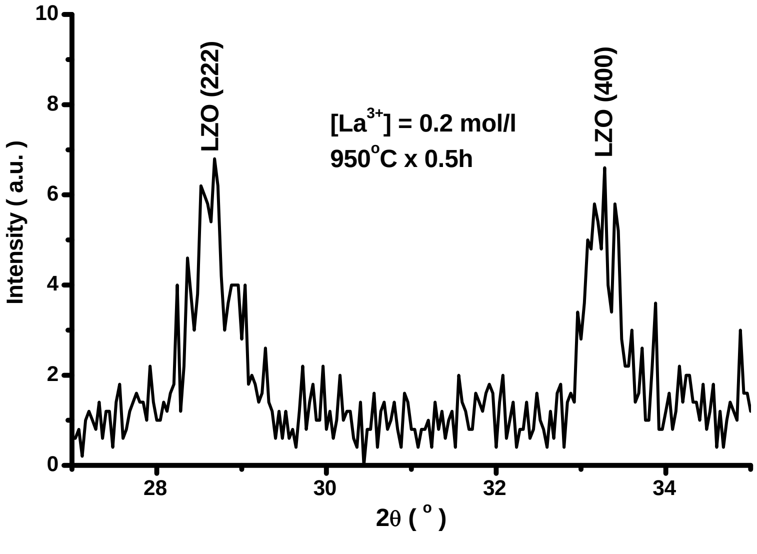

Fig. 6.8 θ-2θ scan of LZO film deposited on a NiW substrate submitted to an oxygen partial pressure larger than in Ar- 5% H_2.

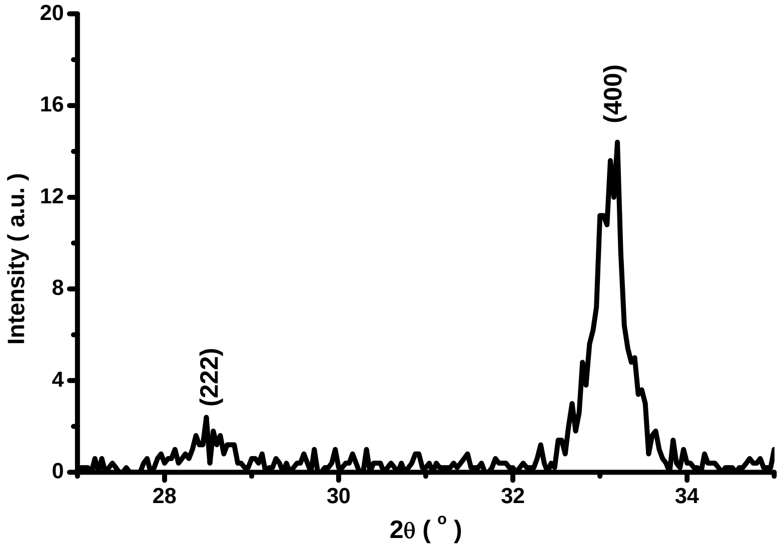

Fig. 6.9 θ-2θ scan of LZO film deposited on a Cu-Ni bi-metallic substrate submitted to an oxygen partial pressure larger than in Ar- 5% H_2

At sufficiently high T, when the equilibrium between H_2 and O_2 is thermodynamically possible

$$2H_2 + O_2 \rightleftharpoons 2H_2O ,$$

Then, the oxygen partial pressure is controlled by the water vapor pressure. Passing the Ar- 5% H_2 mixed gas through distilled water at room temperature will increase substantially the water vapor pressure in the heat-treatment system and then the oxygen partial pressure. XRD pattern of LZO film treated by the above-mentioned treatment is shown in figure 6.8, in which the substrate is a Ni-5at%W substrate. It is clear that the texture of LZO film is very bad. Based on thermodynamic considerations, W element should oxidize under these conditions, giving $NiWO_4$ as a probable phase. So it is suspected that this bad result is due to the oxidation of the substrate. In order to prevent it, a Ni/Cu bi-metallic substrate[30] was used, not susceptible to be oxidized under these experimental conditions. As a result, Fig. 6.9, it is clear that the texture of LZO film is also not a pure cube texture. This implies that the bad texture is not only due to oxidation of substrate. Thus increasing the oxygen partial pressure may affect the C content in film with a complex influence on the growth.

The results in Fig. 6.3 and Fig. 6.5 show that intensity of (400) peak is larger than that of (222) peak, even though the texture of LZO film remains poor. So the hypothesis is suggested that, due to some special reasons, the residual carbon inhibits the growth of homogeneous nucleus more than the growth of heterogeneous nucleus. Based on this, it is believed that the random grains shown in Fig. 6.8 and Fig. 6.9 are due to removing the C-containing species too early in the process. This suggests that C-containing species could be useful in inhibiting the growth of randomly oriented grains.

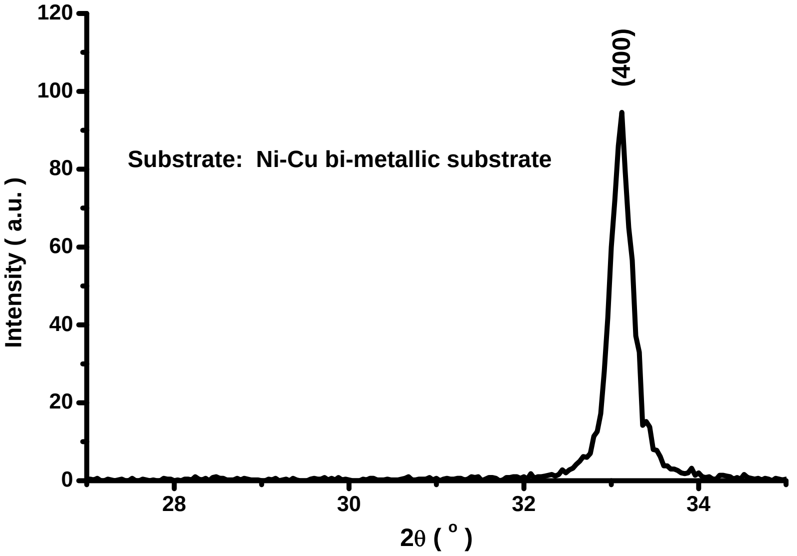

Fig. 6.10 θ-2θ scan of LZO film deposited on Cu-Ni bi-metallic substrate, submitted to an oxygen partial pressure larger than in Ar- 5% H_2

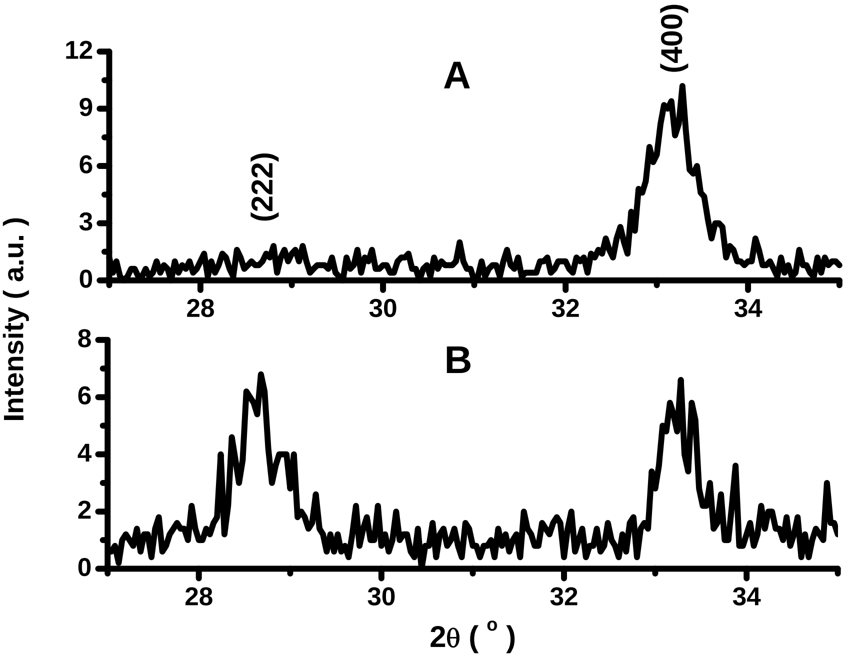

Fig. 6.11 Influence of increasing oxygen partial pressure in the growth stage where substrate is Ni-5at%W substrate

a: θ-2θ scan when humid Ar-5%H_2 gas is introduced at high temperature

b: θ-2θ scan when humid Ar-5%H_2 gas is introduced at initial stage of heat-treatment

Based on these results, it can be concluded that a good cube texture would be obtained if the oxygen partial pressure is increased in the high temperature stage, not in the pyrolysis stage of the heat-treatment. So the following experiment was done to prove this hypothesis: a LZO precursor film deposited on a Cu-Ni bi-metallic substrate was annealed at 950°C for 30 min. During annealing, dry Ar- 5% H_2 was used below 930°C, and was switched to humid Ar- 5% H_2 only above this temperature. The result is shown in Fig. 6.10. It is clear that a strong (400) peak can be found, and there is no (222) peak. It indicates that the sample's texture is very good. It proves the above-mentioned hypothesis. Unfortunately, this procedure does not apply well for Ni-5at%W substrate. The cube texture is enhanced as expected, but random orientations still remain. This is shown on fig. 6.11 (A) where the data are compared with those obtained by introducing the water vapor in the pyrolysis step (B). It is believed that the small (222) contribution in Fig. 6.11A is related with the W oxidation. Although the texture of LZO film is poor, the results in Fig. 6.11 also prove the above-mentioned hypothesis because the intensity of (222) peak in curve A is decreased.

6.3.2.4 Influence of the total pressure on the growth of LZO film

According to the results in previous two sections, the best way to improve the epitaxial growth of LZO film on metallic substrate is to disperse the C-containing gaseous compounds by a large gas speed. Following this conclusion, it is reasonable to expect an influence of the total pressure.

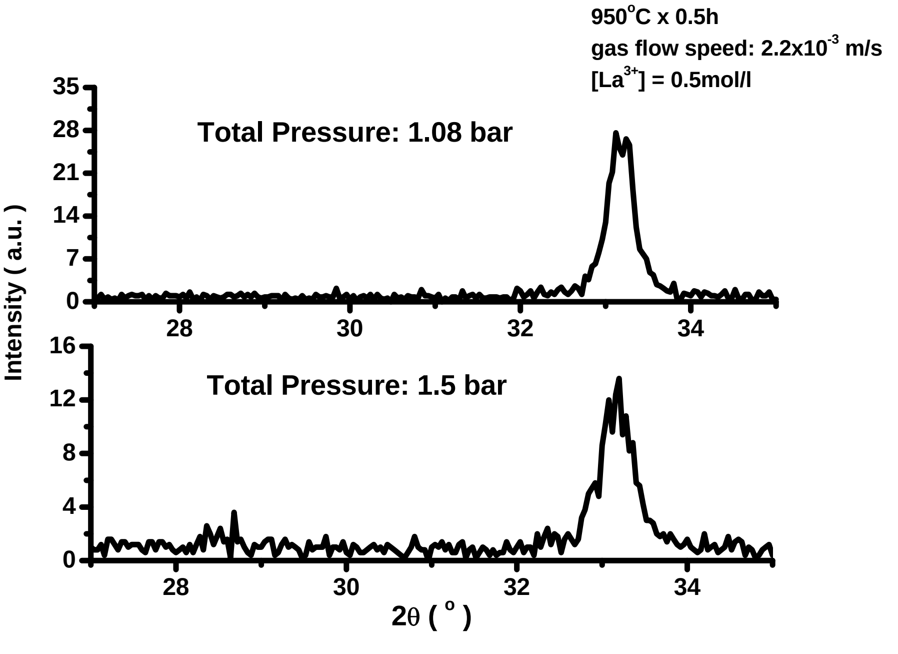

Fig. 6.12 Influence of total pressure on the growth of LZO film

Fig.6.12 shows the influence of the total pressure on the growth of LZO film. It is obvious that the intensity of (400) peak is decreased and a small (222) contribution observed if the total pressure is increased. Two reasons may explain this result. First the dispersion effect of the gas is reduced because the mean free path is reduced. Second, the equilibrium reaction 6.1 is shifted to the right at high pressure.

This suggests that the elimination of C does not occur through a chemical reaction involving a solid-gas reaction such as methane formation (eq.6.4). So increasing the total pressure is not good for obtaining a sharp cube-textured LZO film.

6.3.3 Influences of carbon deposition on the epitaxial growth of LZO

In this section, the influence of the carbon deposition on the growth of LZO film is discussed. Fig. 4.17 shows the relationship between of ΔG and temperature. Usually, the nucleation driving force is inverse proportional to the square of undercooling. So it is clear that the crystallization driving force is very large in chemical solution deposition process. The heterogeneous nucleation occurs more easily than the homogenous nucleation and takes place first. However, a large crystallization driving force makes that the homogenous nucleation could become competitive if the grains nucleating heterogeneously on the substrate cannot grow rapidly due to some inhibition. The competition between the growth of heterogeneous nucleus and homogeneous nucleus induce a mixture of cube texture and random texture.

In order to prevent the oxidation of the metallic substrate, the atmosphere should be reducing. The gaseous species containing C emitted by the pyrolysis diffuses through the bulk of the film and are reduced at the surface of the film; this produces a C layer at the surface. The carbon results from reaction 6.1 and 6.2 at low temperature and from reaction 6.3 at high temperature. Thus, a gradient of C exists inside the LZO film which steepness increase with the flow of gas, as drawn in fig.6.3. It is reasonable to admit that the gradient of residual carbon preexists to the nucleation of LZO and we expect it to affect the growth of the grains.

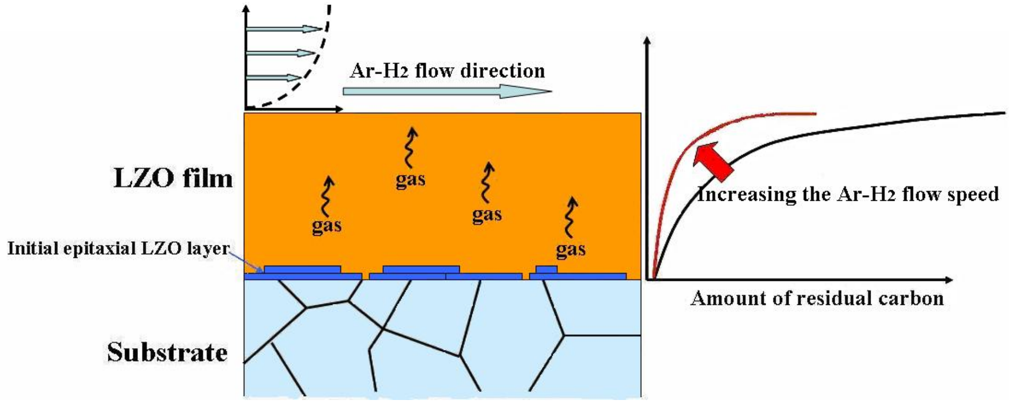

Fig. 6.13 Schematic diagram representing the distribution of residual carbon in LZO film

However, hydrodynamics recalls that the real speed of gas near the sample's surface is almost zero even if for large gas speed. It implies that carbon deposition always exists. Due to the distribution of residual carbon, the epitaxial LZO layer can grow rapidly, but the growth of random nucleus in bulk of LZO film is inhibited. If the gas speed is not large enough, the distribution gradient of residual carbon is flat, and the epitaxial growth of LZO film is inhibited. It results in the existence of unwanted randomly oriented grains in the LZO film. At sufficiently high speed of gas, LZO film with a high volume fraction of cube texture can be obtained finally.

When the oxygen partial pressure is increased, the residual carbon cannot be deposited at the surface of the film. Then homogenous nucleus can grow and compete with heterogeneous nucleus, resulting in a texture composed of cube texture and random grains. However, if the oxygen partial pressure is increased at high temperature, the deposition of C can occur in the beginning of the process and prevents homogeneous grains to grow. When the total pressure is increases, it is believed this makes the distribution of residual carbon to become flat which is not favorable. So finally, the existence of a distribution gradient of residual carbon appears to be helpful for the epitaxial growth of LZO films.

To summary, the influence of the deposited carbon on the growth of LZO film is related with its gradient of concentration inside the LZO film. A sharp gradient is helpful to grow a cube-textured LZO film on metallic substrate by CSD process.

6.3.4 Characteristics of LZO film

6.3.4.1 Crystal structure of LZO film

The LZO phase exists according to two structures[130]: pyrochlore structure and fluorite which is a disordered variety of the pyrochlore. These two phases have the different ability to resist the oxygen diffusion, the pyrochlore being the best to resist oxygen diffusion. Note that according to the equilibrium phase diagram, the fluorite is metastable in the temperature range below 1100°C

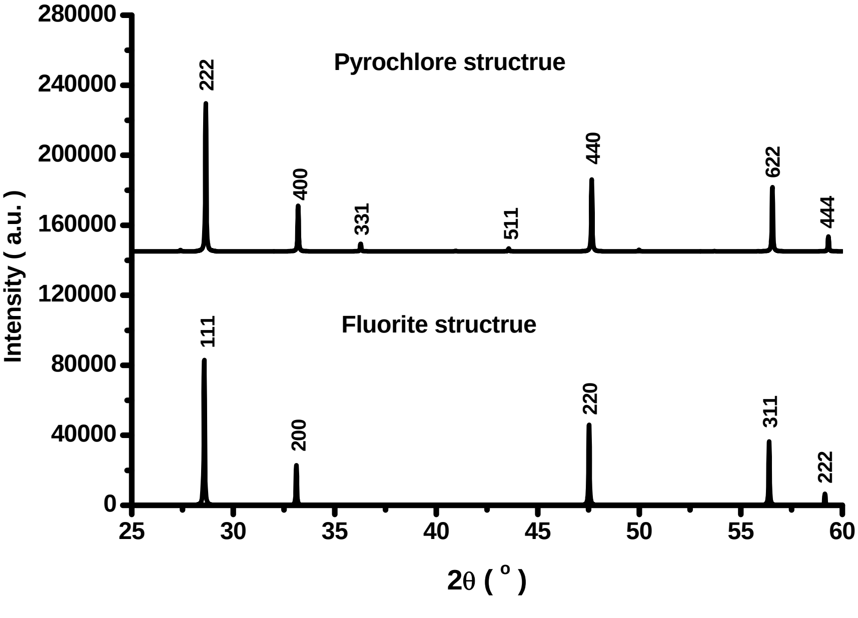

Fig. 6.14 ideal θ-2θ scans of LZO phases with different crystal structure

Ideal θ-2θ diagrams of these two different structures are shown on fig.6.14 (plotted using powdercell software). From Fig. 6.14, it is clear that the difference between these two structures in the θ-2θ range is that the two peaks indexed as (331) and (511) peak in the pyrochlore structure do not exist in fluorite structure. The ideal {331} pole figure of LZO crystal having the pyrochlore structure is shown in Fig. 6.15. Twelve poles should be seen at $\chi = 46.5^{o}$ and 76.7^{o}, respectively, eight come from (331) equivalent reflections and four from (133) equivalents. So if the structure of the LZO film which was deposited on the Ni-5at%W substrate is a pyrochlore structure, there would be 8 peaks in ϕ scan curve of (331). The results are shown in Fig. 6.16 from what 8 weak peaks are obvious. This proves that the LZO film's crystal structure is a pyrocholore structure.

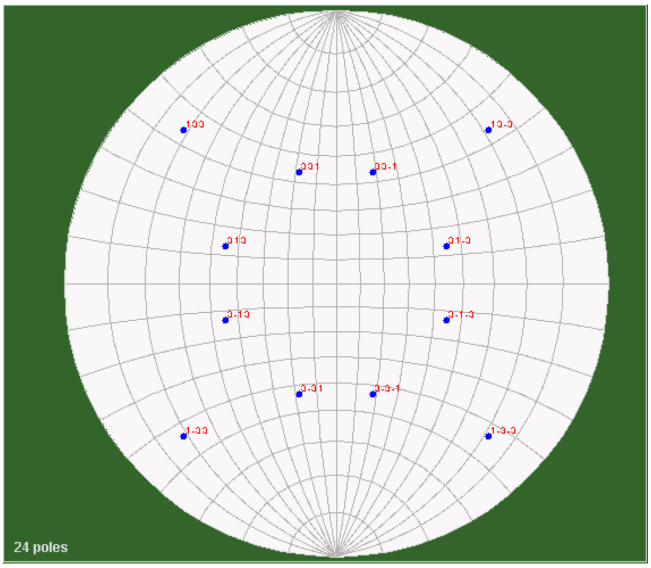

Fig. 6.15 an ideal (331) pole figure of LZO crystal with pyrochlore structure

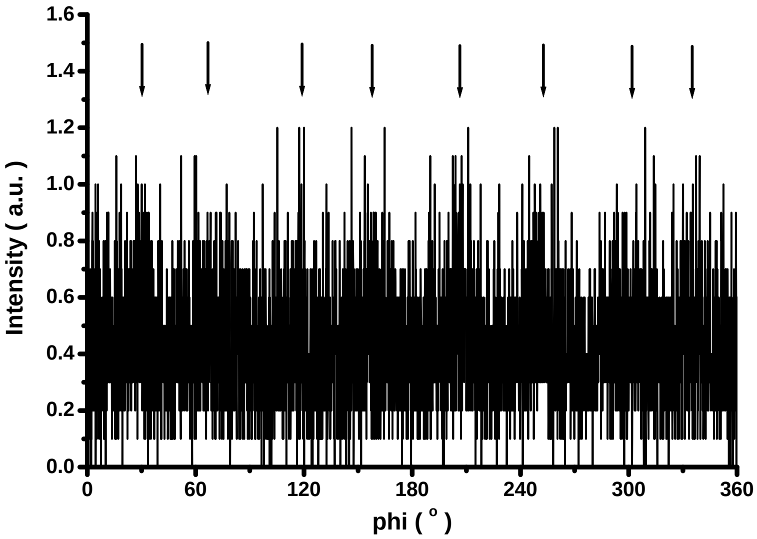

Fig. 6.16 ϕ(331) scan of LZO film

6.3.4.2 Texture sharpness and surface characteristics of LZO film

A LZO film must have a sharp cube texture and a good surface crystallinity. In previous sections of this chapter we discussed how to improve the volume fraction of cube texture. In this section, we focus on the sharpness of cube texture and surface characteristics of the LZO films.

Fig.6.17 and Fig 6.18 show the texture's sharpness of samples fabricated under different gas flow speeds were $2.2x10^{-3}$m/s and $6.8x10^{-2}$m/s respectively. At first sight, it may be concluded that the gas flow speed does not influence the sharpness of cube texture of LZO film because the FWHM values of ω scans and one of ϕ scans are similar. But a more careful comparison between the sharpness of the textures shows that the film has a sharper texture when the speed of the gas is larger. It implies that a large gas flow speed is benefit to the epitaxial growth of LZO film on a Ni-5at%W substrate.

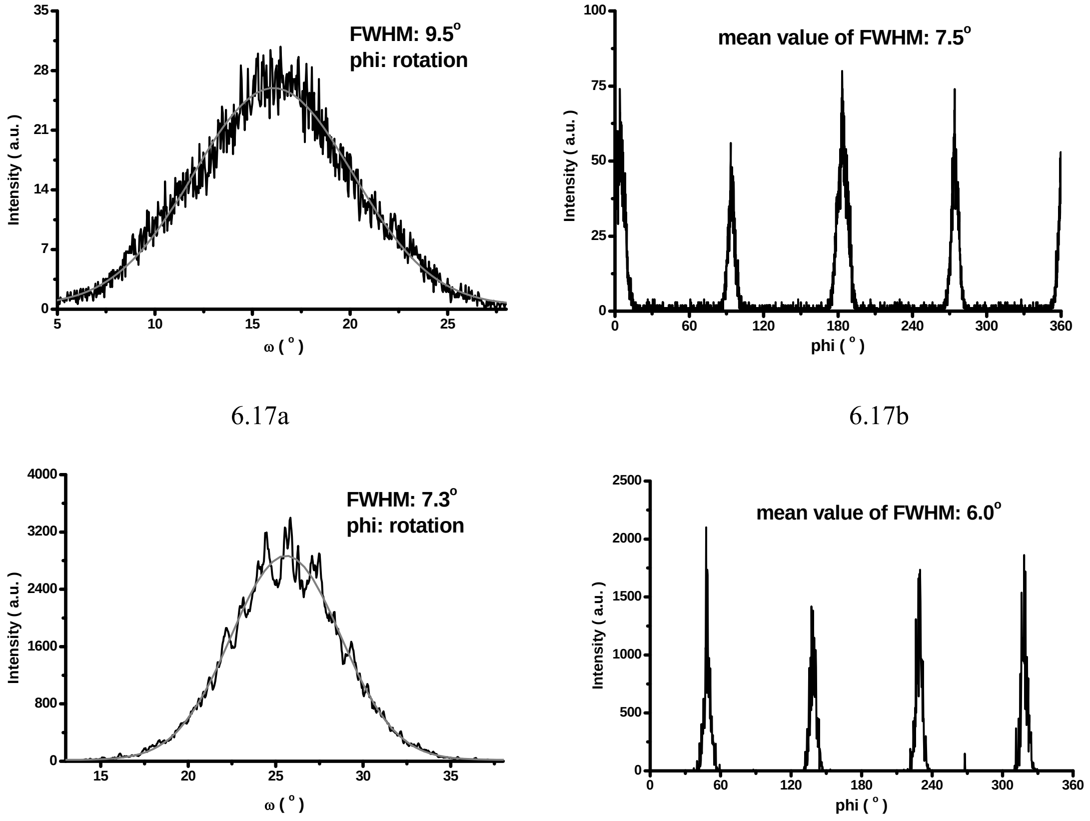

6.17a

6.17b

6.17c

6.17d

Fig. 6.17 Sharpness of cube texture of a LZO film for a slow gas speed ($2.2x10^{-3}$m/s). a and b: LZO film c and d: substrate

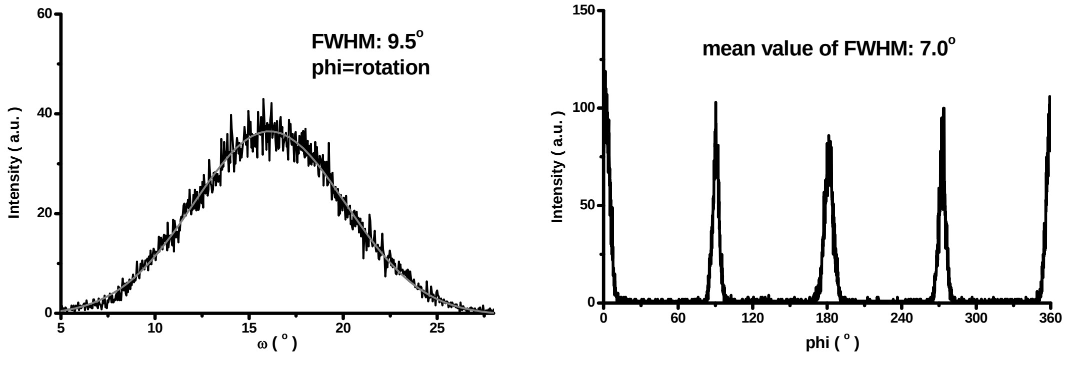

6.18a

6.18b

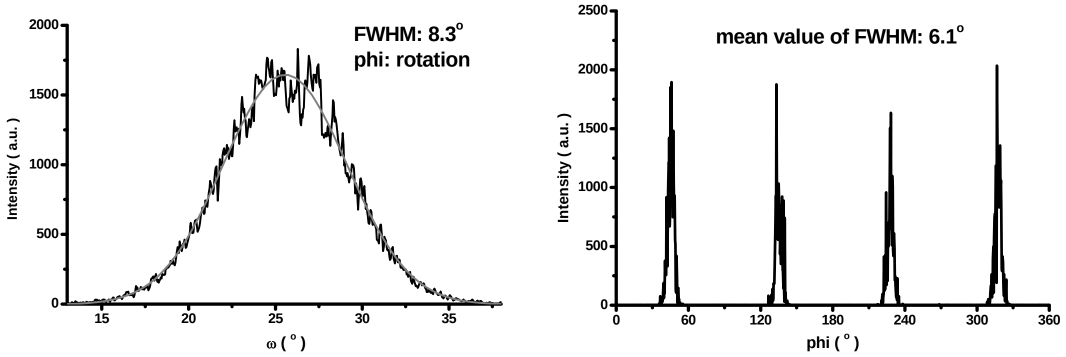

6.18c 6.18d

Fig. 6.18 sharpness of cube texture of LZO film for a high gas speed ($6.8x10^{-2}$m/s). a and b: LZO film c and d: substrate

Because the penetration depth of x ray is larger than several microns, the data of XRD cannot show the information about the top layer of LZO films. The texture characteristics of the top layer of LZO film are very important for depositing other oxide layer. It is then necessary to check the texture of the top layer by a method sensitive to the surface. Fig. 6.19 shows the EBSD images for a sample fabricated under a high gas flow speed ($6.8x10^{-2}$m/s). From this figure, it is found that this sample has a pure cube texture at all measured scales, except in some small places (black spots). Calculation shows that the volume fraction of cube texture is larger than 96%.

Although EBSD is very sensitive to the structure of the surface, the penetration depth of EBSD is still several nanometers. Refection High-Energy Electron Diffraction (RHEED) technology is more sensitive to the structure of surface, it probe only a few atomic layers of the surface and is therefore powerful to study the surface crystallinity of LZO film. Fig. 6.20 shows the RHEED image of LZO film obtained under the gas flow speed of $6.8x10^{-2}$m/s. It is obvious that the diffraction occurs in spots but not rings, pointing out to a textured surface with a three-dimensional morphology.

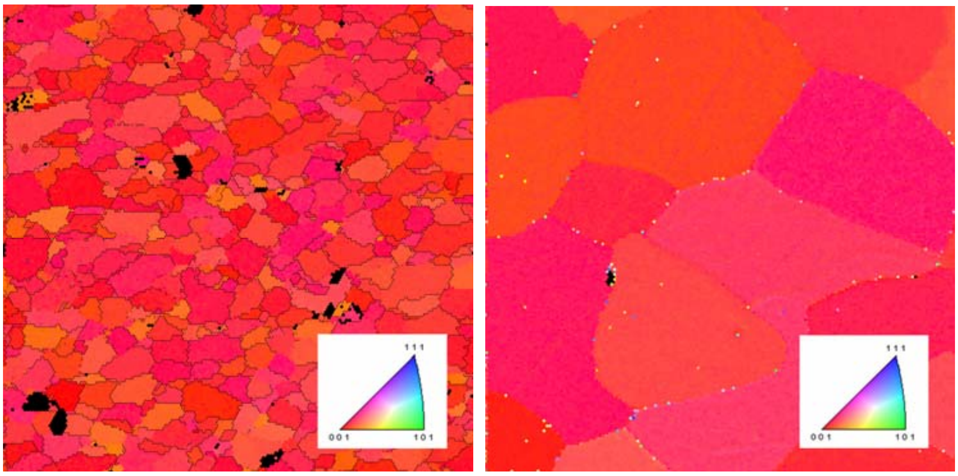

6.19a 6.19b

Fig. 6.19 EBSD images. Insert shows the inverse pole figure. a: scale 600×600 μm; b: scale is 80×80 μm

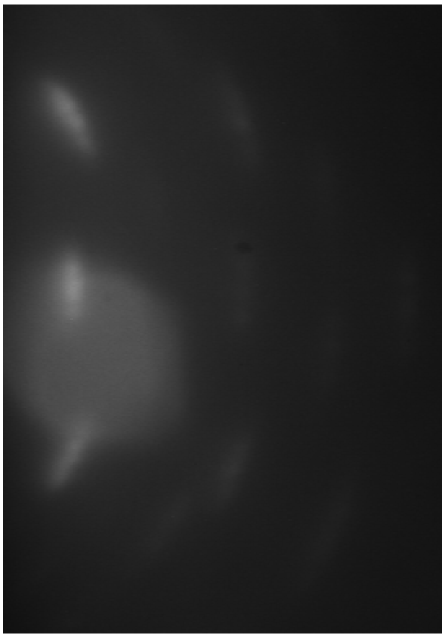

Fig. 6.20 RHEED of the same sample

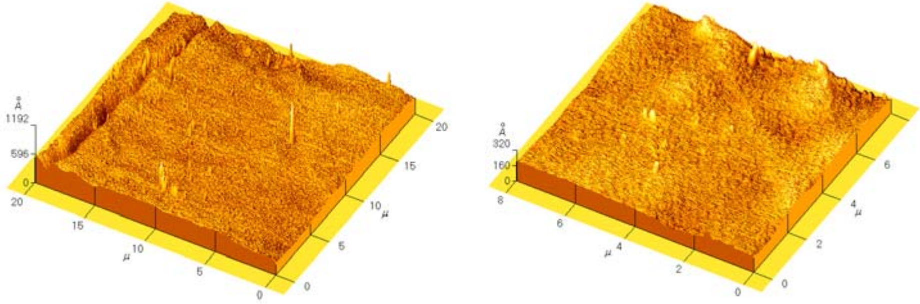

6.21a 6.21b

Fig. 6.21 AFM of the same film

a: scale 20×20 μm; b: scale 8×8 μm

The roughness (Ra) of this probed by AFM, fig. 6.21 is in the range of 6.6 nm in a square of 20x20 μm, and 3.2 nm in a square of 8x8 μm.

6.3.5 Deposition of CeO_2 layer on LZO film by CSD

To confirm that the LZO layer deposited on Ni- 5 at% W substrate was suitable to grow a second epitaxial layer, a film of CeO_2 was deposited on its surface. X-ray diffraction results are shown in Fig.6.22, in which a θ-2θ scan of the sample without CeO_2 layer is also plotted in Fig. 6.22 for comparison.

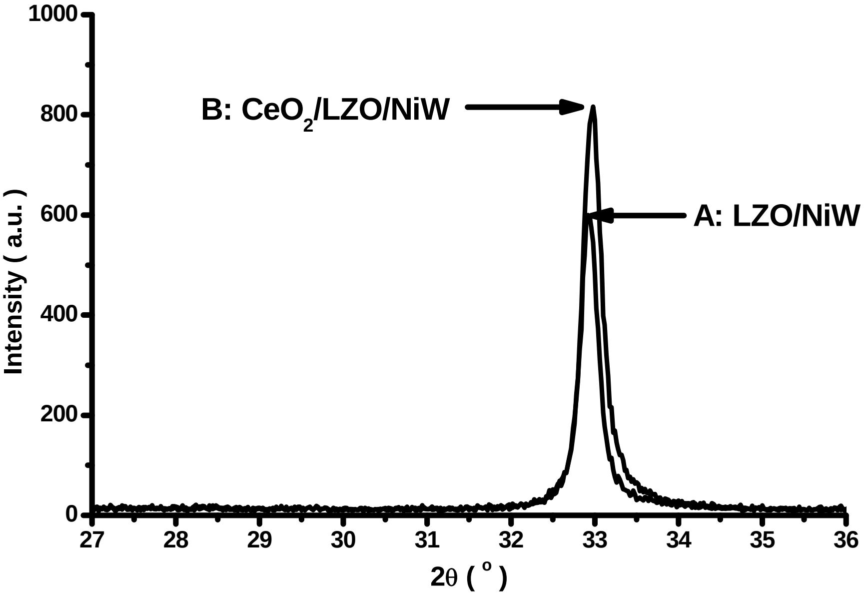

Fig. 6.22 θ-2θ diagrams of a sample A : LZO/NiW and B CeO2/LZO/NiW

Table 6.2 Texture sharpness of samples of MOD-CeO_2/MOD-LZO/NiW

	FWHM value of ω scan (°) (ϕ = rotation)	FWHM value of ϕ scan (°)
CeO_2/LZO layer	8.2	6.3
Ni-5at%W substrate	7.5	6.1

Because the diffraction angle of $(200)_{CeO2}$ peak (33.08°) is very close to that of $(400)_{LZO}$ peak (33.19°), and because the peaks are rather broad, there is no split of the peak. But, comparison of the intensities of peaks B and A shows that the increase is due to the contribution of the CeO_2 layer. Furthermore, no peak is found at 28.5° where the (111) diffraction peak of CeO_2 could occur. It indicates that the texture of CeO_2 layer has reproduced that of LZO by epitaxy.

The (400) peak position of LZO bulk should be at 33.19°, but the $(400)_{LZO}$ is observed at 32.92° in LZO film. It means that LZO film is strained. The c axis is elongated and the (ab) plane compressed as expected from the lattice of mismatch with Ni5W. After deposition of CeO_2 layer the diffracted peak is found at 32.99°, indicating that the strain is partially relaxed.

Table 6.2 compares the sharpness of CeO_2/LZO layer's textures to that of substrate's texture. The differences between FWHM values of CeO_2/LZO layers and that of substrate are 0.6° for ω scan and 0.2° for ϕ scan, respectively. It proves that the CeO_2/LZO layers deposited by CSD grow epitaxially on Ni-5 at% W substrate.

6.4 Summary

The residual carbon of pyrolysis has an influence on the final texture of $La_2Zr_2O_7$ film deposited on a metallic substrate like Ni 5at% W. The residual C modifies the respective contribution from heterogeneous and homogeneous nucleates.

The gas speed flowing over the sample is an important parameter to decrease the carbon amount and increase the volume fraction of cube texture in LZO film, the oxygen partial pressure is also very efficient to oxidize the residual carbon, but it should be preferentially employed at high temperature.

The characteristics of LZO film obtained under optimal conditions show that the LZO film with cube texture can be epitaxially grown up to its top surface. The volume fraction of cube texture of LZO film is larger than 96%, the FWHM of ω scan of LZO film is 8.1^o, and the FWHM of ϕ scan of LZO film is 6.0^o. At the same time, the surface of LZO film is crystallized and smooth. Depositing successfully a cube textured CeO_2 layer on such LZO layer also proves the success of depositing a $La_2Zr_2O_7$ film on a metallic substrate by CSD.

Chapter VII Conclusions and Future Works

In order to find a simple and economical method to obtain coated conductors, two fields were explored: one was to fabricate a new bi-metallic substrate by electro-deposition with low magnetic properties, the other was to deposit $La_2Zr_2O_7$ (LZO) film on metallic substrate by chemical solution deposition CSD.

The study of electro-deposition shows that the Cu-Ni bi-metallic substrate gets sharp cube texture and a good thermal stability of the texture. The weakness of the pure Cu substrate has been then overcome by electro-depositing a Ni layer on the Cu substrate. This new Cu-Ni bi-metallic substrate has a lower magnetic moment compared to that of Ni-5at%W substrate. The magnetic properties of this Cu-Ni substrate decrease after annealing because of the inter-diffusion between Cu and Ni layer. The fact that a cube-textured LZO film can be deposited successfully on it by CSD implies that the Cu-Ni bi-metallic substrate is an interesting new potential metallic substrate for coated conductors.

The deposition of LZO films on metallic substrate by CSD has been studied in this thesis. The modification of the surface characteristics of the metallic substrates by a sulfuration process, the influence of a c(2x2)-S superstructure on the formation of a LZO film, and the factor inhibiting the epitaxial growth of LZO film on a metallic substrate are discussed in details. The results show that the c(2x2)-S superstructure can control the orientation of LZO nucleus formed at the metal/oxide interface. The residual carbon is the main factor inhibiting the epitaxial growth of LZO layer on a NiW substrate. For optimized conditions, cube-textured LZO films with good surface crystallinity can be deposited on metallic substrate, such as Ni-5at%W substrate and Cu-Ni bi-metallic substrate, by CSD.

7.1 Main conclusions

7.1.1 Fabrication of Cu-Ni bi-metallic substrate

The rolling deformation rate is a key factor to obtain cube textured Cu tapes. The cube-textured Cu tapes are obtained only for rolling deformation rate larger than a critical one (>95.8%). The thickness per pass reduction influences the sharpness of the texture. A large thickness reduction per pass will decrease the sharpness of the out-of-plane component along the transverse direction. The texture of the superficial zone may be different from that of the bulk. A shear texture can be found sometimes in the superficial zone, but it does not impede the cube texture formation; it influences the sharpness of the cube texture.

Study of heat-treatments show that the higher the temperature of heat treatment is, the larger the volume fraction of cube texture in samples is, provided the temperature remain below the recrystallisation temperature. It can also be found that the growth speed of cube texture in Cu tapes is very rapid. After rolling-recrystallizion, the volume fraction of cube texture is larger than 97%, the sharpness of in-plane texture and of out-of-plane texture are 6.1° and 6.9° respectively.

When the pH is between 4 and 5, at room temperature, a cube-textured Ni layer can be deposited on a cube-textured Cu tape by electro-deposition if the cathode potential is lower than -0.96V (SEC). The texture of the Cu-Ni bi-metallic is characterized by a FWHM of ω scan equal to 5.2^o and a FWHM of ϕ scan equal to 7.1^o. After the heat-treatment at 950℃ during 30 mins, the in plane FWHM (ϕ scan) is decreased to 6.1°. Cathode potential, pH and temperature of electrolyte, morphology of the Cu substrate and thickness of the Ni layer influence the texture's sharpness. Low roughness is favourable to obtain sharp texture of the Ni layer but mechanical polishing of the Cu tape impede to deposit cube-textured Ni. The thickness of the deposited Ni layer not only influences the sharpness of its texture, but also its thermal stability: the thermal stability becomes poor with increasing the thickness of the Ni layer.

A comparison of the magnetic properties of Cu-Ni bi-metallic substrate before and after their heat treatment at 950°C shows a lowering of their magentisation after the heat treatment and smaller magnetic losses of Cu-Ni bi-metallic substrate comparerd to Ni-5at%W substrate.

7.1.2 Deposition of LZO film by chemical solution deposition process

Acetylacetonate is diffuclt to dissolve in organic solvents except carboxylic acids. Hence propionic acid is a good solvent for preparing a precursor solution of LZO. The heat treatment of the precursor powder show that LZO phase can be formed above 700°C under reducing conditions (Ar- 5% H_2), oxygen atmosphere is not appropriate for such precursor.

High heating temperature and high heating rate are helpful for the epitaxial growth of LZO film on constantan substrates. Increasing the heating dwell is good for obtaining a high volume fraction of cube texture in LZO film if the heating time is shorter than 5 hours, but increasing the heating time beyond this time results in pores and crack opening at the surface of the LZO film. It is important to consider that cube-textured LZO film can be formed on constantan substrate even when the texture of the substrate changes during the heat-treatment. It implies that a cube-textured oxide layer can be deposited on a metallic substrate provided that the texture of the substrate does not change until the nucleation temperature of the oxide layer is reached by the schedule of the heat treatment.

A simple sulfuration process deliver a c(2x2)-S superstructure on Ni-5at%W substrate and Cu-Ni bi-metallic substrate, this process combines a cleaning step under vacuum, a chemisorptions of S at room temperature, a desorption of the excess at high temperature under Ar- 5% H_2 atmosphere. This c(2x2)-S superstructure does not improve the final texture of LZO film alone, but this is a combination of optimum heat-treatment with sulfuration process that can fabricate a cube-textured LZO film with a good surface crystallinity on metallic substrate. A further analysis shows that c(2x2)-S superstructure can control the orientation of initial LZO grains (nucleus) formed on the metal-oxyde interface.

The residual carbon in LZO film is an influent factor that inhibits the epitaxial growth of LZO film. It results from the reduction of C-containing gaseous speicies emitted during the pyrolysis stage of LZO precursor. The residual carbon influences the texture of LZO film by its effects on the relative contribution of the heterogeneous growth and of the homogenous growth. This is dictated by the residual C distribution before the crystallizing of LZO film. A sharp gradient of residual carbon in the pyrolysed LZO film (before crystallization) is welcome to grow the cube-textured LZO film on Ni-5 at %W. Increasing gas speed flowing over the sample or oxygen partial pressure are two ways to suppress the negative influence of residual carbon. However, increasing the gas speed flowing over the sample is the best way in our conditions to obtain sharpe cube-textured LZO films with a good surface crystallinity on Ni-5 at %W substrate.

Analysis of the crystal structure, texture and surface characteristics of LZO film show that, after the optimized heat-treatment of LZO precursor, a cube-textured LZO film with a good crystalline and smooth surface can be obtained by CSD on metallic substrate. The volume fraction of cube texture of LZO film is larger than 96%, and its sharpness good (FWHM of ω scan of LZO film is 9.5°, and FWHM of ϕ scan of LZO film is 7.0^o). A cube-textured CeO_2 layer can also be deposited successfully on this LZO film by a similar method.

7.2 Future work

The successful deposit of LZO film on the Cu-Ni bi-metallic substrate shows that this new substrate is a good potential substrate for coated conductors. However this work was restricted to short samples, the technologies to obtain long substrates must be worked out.

The quantification of the sharpness of metallic substrates' texture is still an open question which is not solved only by measuring ω and ϕ scan. For example, in measurements of ω scan, the measured value in rotating conditions (ϕ angle) is generally intermediate between the values measured in transverse direction and along the rolling direction. However some exceptions were highlighted in this thesis. Thus more experiments should be done in order to have more consistent characterization of the sharpness of the cube texture.

Based on chemical and thermodynamic analysis, the inhibiting factor of the epitaxial growth of LZO film on metallic substrate has been discussed qualitatively. However more detailed information about nucleation and epitaxial growth of LZO film should be done to reach a quantitative description of the phenomenon. It will be a future work.

In order to process a long YBCO tape, a dip-coating is the simplest way to fabricate coated conductors by CSD. But we only used spin-coating in this thesis. Further experiments should be done to solve the scientific and technologic questions about deposition of LZO films on metallic substrate by dip-coating.

YBCO layer is the functional layer of coated conductors, but deposition of a buffer layer on metallic substrate has just been considered in this thesis due to limited time, so it is an important future work to study the deposition of YBCO layer on CeO_2/LZO buffer layer architecture.

References

1. Wu M K, Ashburn J R, Torng C J, Hor P H, Meng R L, Gao L, Huang J, Wang Y Q, Chu C W. Superconductivity at 93K in a new mixed-phase Yb-Ba-Cu-O compound system at ambient pressure[J]. Phy.Rev.Lett., 1987,58:908-910

2. 赵忠贤, 陈立泉, 杨乾声, 黄玉珍, 陈庚华, 唐汝明, 刘贵荣, 崔长庚, 陈烈, 王连忠, 郭树权, 李山林, 毕建清. Ba-Y-Cu氧化物液氮温区的超导电性[J]. 科学通报, 1987, 6: 412

3. Xu Y L, Shi D L. A Review of coated conductor development[J]. Tsinghua science and technology, 2003, 8(3):342-369

4. Satou M, Yamada Y, Murase S, Kitamura T, Kamisada Y. Densification effect on the microstructure and critical current density in $(Bi,Pb)_2Sr_2Ca_2Cu_3Ox$ Ag sheathed tape[J]. Appl.Phys.Lett., 1994, 64(5):640-642

5. Utsunomiya H, Sakai T, Saito Y, Matsuo T. Critical current density of rolled silver-sheathed Bi(2223) tapes[J]. Physica C, 1995, 250(3-4): 340-348

6. Huang Y B, G F de la Fuente, Larrea A, Navarro R. Formation and stability of the 2223 phase in high-Jc Ag-sheathed $(Bi,Pb)_2Sr_2Ca_2Cu_3O_{10+delta}$ tapes[J]. Supercond.Sci.Technol., 1994, 7:759-764

7. S.X.Dou, Liu H K. Ag-sheathed Bi(Pb)SrCaCuO superconducting tapes[J]. Supercond.Sci. Technol., 1993, 6:297-301

8. Li C S, Zhang P X, Yu Z M, Zheng H L, Xiong X M, Liu Y S, Wang Q Y, Liu F S, Wu Y F, Ji P, Zhou L. The effect of processing parameters on the phase assemblage and critical current density in Bi(Pb)-2223 tapes[J], Physica C,2003,386:127-130

9. Zhou L, Zhang P X Ji P, Wang K G, Wang J R, Wu X Z. The properties of YBCO superconductors prepared by a new approach: the 'powder melting process'.Supercond. Sci.Technol. 1990, 3(10):490-492

10. Jin S, Tiefel T H, Sherwood R C, Davis M E, van Dover R B, Kammlott G W, Fastnacht R A, Keith H D. High critical current in Y-Ba-Cu-O superconductors. Appl.Phys.Lett., 1988, 52:2074-2076

11. Murakami M, Gotoh S, Fujinoto H, Yamaguchi K, Koshizuka N, Tanaka S. Flux pinning and critical currents in melt processed YbbCuO supercondiuctors. Supercond.Sci.Technol. 1991, 4(1S):S43-S50

12. Iijima Y, Tanabe N, Kohno O, Ikeno Y. In-plane aligned $YBa_2Cu_3O_7$ thin films deposited on polycrystalline metallic substrates[J]. Appl.Phys.Lett., 1992,60(6):769-771

13. Norton D P, Goyal A, Budai J D, Christen D K, Kroeger D M, Specht E D, He Q, Saffian B, Paranthaman M, Klabunde C E, Lee D F., Sales B C, List F A. Epitaxial $YBa_2Cu_3O_7$ on Biaxially Textured Nickel (001): An Approach to Superconducting Tapes with High Critical Current Density[J]. Science, 1996, 274(5288):755-757

14. Goyal A, Norton D P, Kroeger D M, Christen D K, Paranthaman M, Specht E D, Budai J D, He Q, Saffian B, List F A, Lee D F, Hatfield E, Martin P M, Klabunde C E, Mathis J, Park C. Conductors with controlled grain boundaries: An approach to the next generation, high temperature superconducting wire[J]. J.Mater.Res., 1997,12(11):2924-2939

15. Lvanov Z G, Nilsson P Å, Winkler D, Alarco A, Claeson T, Stepantsov E A, Tzalenchuk A Ya.

Weak links and dc SQUIDS on artificial nonsymmetric grain boundaries in $YBa_2Cu_3O_{7-\delta}$[J]. Appl.Phys.Lett.,1991, 59(23):3030-3032

16. Heinig N F, Redwing R D, Nordman J E, Larbalestier D C. Strong to weak coupling transition in low misorientation angle thin film $YBa_2Cu_3O_{7-x}$ bicrystals[J]. Physical review B, 1999, 60(2):1409-1417

17. Paranthaman M, Goyal A, List F A, Specht E D, Lee D F, Martin P M, He Q, Christen D K, Norton D P, Budai J D, Kroeger D M. Growth of biaxially textured buffer layers on rolled-Ni substrates by electron beam evaporation[J]. Physica C, 1997, 275(3-4):266-272

18. He Q, Christen D K, Budai J D, Specht E D, Lee D F, Goyal A, Norton D P, Paranthaman M, List F A, Kroeger D M. Deposition of biaxially-oriented metal and oxide buffer-layer thilms on textured Ni tapes: New substrates for high-current, high-temperature superconductors[J]. Physica C, 1997, 275(1-2):155-161

19. Eickemeyer J, Selbmann D, Opitz R, Wendrock H, Maher E, Miller U, Prusseit W. Highly cube textured Ni-W-RABiTS tapes for YBCO coated conductors[J]. Physica C, 2002, 372-376:814-817

20. Ijaduola A O, Thompson J R, Goyal A, Thieme C L H, Marken K. Magnetism and ferromagnetic loss in Ni-W textured substrate for coated conductors[J]. Physica C, 2004, 403:163-171

21. Zhou Y X, Naguib R, Fang H, Salama K. Development of cube textured Ni-W alloy tapes using powder metallurgy along with high energy ball milling for HTS coated conductors[J]. Supercond.Sci.Tech., 2004, 17:947-953

22. Leonard K J L, Goyal A, Kang S, Yarborough K A, Kroeger D M. Identification of a self-limiting reaction layer in Ni-3at.%W rolling-assisted biaxially textured substrates[J]. Supercond.Sci.Tech., 2004, 17:1295-1302

23. Woodcock T G, Cheung Y L, Grenfell J R A, Abell J S. Formation of $NiWO_4$ during high temperature oxidation of Cube textured Ni-3at.%W substrates[J]. Supercond.Sic.Tech., 2005, 18:721-725

24. Huhne R, Kursumovic A, Tomov R I, Glowacki B A, Holzapfel B, Evetts J E. Texture and microstructure analysis of epitaxial oxide layers prepared on textured Ni-12wt%Cr tapes[J]. J.Phys.D: Appl.Phys., 2003, 36:1053-1057

25. de Boer B, Eickemeyer J, Reger N, Fernandez L, Richter J Holzapfel B, Schultz L, Prusseit W Berberich P. Cube textured nickel alloy tapes as substrates for $YBa_2Cu_3O_7$-coated conductors[J]. Acta Mater., 2001, 49:1421-1428

26. Soubeyroux J L, Bruzek C E, Girard A, Jorda J L, Thermal treatments for biaxially textured Cu-Ni alloys for YBCO coated conductors[J]. IEEE-Trans Applied Superconductivity, 2005, 15:2687-2690

27. Tuissi A, Corti R, Villa E, Bramley A P, Vickers M E, Evetts J E. Biaxially textured Ni and CuNi alloy substrate tapes for HTS coated conductor applications[J]. Inst.Phys.Conf.Ser., 2000, 167:399-402

28. Yust N A, Nekkanti R, Brunke L B, Srinivasan R, Barnes P N. Copper metallic substrates for high temperature superconducting coated coanductors[J]. Supercond.Sci.Tech., 2005, 18:9-13

29. Pinol S, Diaz J, Segarra M, Espiell F. Preparation of biaxially cube textured Cu substrate tapes for HTS coated conductor applications[J]. Soubeyroux J L, Bruzek C E, Girard A, Jorda J L, Thermal treatments for biaxially textured Cu-Ni alloys for YBCO coated conductors. Supercond.Sci.Tech., 2001, 14:11-15

30. Yu Z M, Odier P, Ortega L, Zhang P X, Li C S, Liu X H, Zhou L. LZO covered Cu-based substrates[J]. Jouranl of Alloy anc Compounds, In press.

31. Cantoni C, Christen D K, Specht E D, Verela M, Thompson J R, Gapud A, Thieme C Xu Y, Pennycook S J. Characterization of suitable buffer layers on Cu and Cu-alloy metal substrates for the development of coated conductors[J]. Supercond.Sci.Technol., 2004, 17:S341-S344

32. Aytug T, Paranthaman M, Thompson J R, Goyal A, Rutter N, Zhai H Y, Gapud A A, Ijduola A O, Christen D K. Electrical and magnetic properties of conductive Cu-based coated conductors[J]. Applied Physics Letters, 2003, 83(19):3963-3965

33. Kyunghoon Kim, Paranthaman M, Norton D P, Aytug T, Cantoni C, Gapud A A, Goyal A, Christen D K. A perspective on conducting oxide buffers for Cu-based YBCO-coated conductors[J]. Supercond.Sci.Technol., 2006, 19:R23-R29

34. Mingji Jin, Han S C, Sung T H, Kwangsoo N. Biaxial texturing of Cu sheets and fabrication of ZrO_2 buffer layer for YBCO HTS films[J], Physica C, 2000, 344:243-248

35. Zhou Y X, Sun L, Chen X, Putman P T, Salama K. The manufacturing of an electroplated Ni Layer on textured Cu substrate for Cu-based HTS coated conductors[J]. Supercond.Sci.Tech., 2005, 18:107-111

36. Rutter N A, Goyal A, Vallet C E, List F A, Lee D F, Heatherly L Kroeger D M. Ni overlayers on biaxially textured Ni-alloy and Cu substrates by DC sputtering[J]. Supercond.Sc. Tech., 2004, 17:527-531

37. Yu Z M, Zhou L, Odier P, Zhang P X. Niew Cu-Ni substrate for coated conductors[J]. Materials Science Forum, 2007, 546-549:1877-1880

38. Suo H L, Genoud J Y, Triscone G, Walker E, Schindl M, Passerini R, Cleton F, Zhou M L, Flukiger R. Preparation and characterization of {100}<001> cube textured Ag substrates for in-plane oriented HTS tapes[J]. Supercond.Sci.Technol., 1999, 12:624-632

39. Liu D M, Li E, Hu Y C, Liu M, Xiao W Q, Zhou M L. The influence of annealing parameters on texture of Ag substrate[J]. Physica C, 2004, 406:79-86

40. Budai J D, Young R T, Chao B S. In-plane exptaxial alignment of $YBa_2Cu_3O_{7-x}$ films grown on silver crystals and buffer layers[J]. Appl.Phys.Lett., 1993, 62(15):1836-1838

41. Liu M, Liu D M, Zhou M L, Zhao Y, Gao X, Liang J X. Fabrication of YBCO tapes on Ag substrates by the ultrasonic spray pyrolysis method[J]. Superoncd.Sci.Technol., 2004, 17:676-680

42. Li M, Ma B, Koritala R E, Fisher B L, Dorris S E, Venkataraman K, Balachandran U. Growth and properties of YBCO thin films on polycrystalline Ag substrates by inclined substrate pulsed laser deposition[J]. Supercond.Sci.Technol., 2002, 15:986-990

43. Doi T, Mori M, Shimohigahsi H, Hakuraku Y, Onabe K, Okada M, Kashima N, Nagaya S. {110}<112> and {110}<110> textured Ag tapes for biaxially oriented $YBa_2Cu_3O_7$ coated conductors[J]. Physica C, 2002, 378-381:927-931

44. Wells J J, MacManus-Driscoll J L, Genoud J Y, Suo H L, Walker E, Flukiger R. {110}<110> textured Ag ribbons for biaxially aligned YBa2Cu3O7-x coated conductor tapes[J]. Suprecond.Sci.Technol., 2000, 13:1390-1398

45. Kreiskott S, Arendt P N, Coylter J Y, Dowden P C, Folytn S R, Gibbons B J, Matias V, Sheehan C J. Reel-to-reel preparation of ion-beam assisted deposition (IBAD)-MgO based coated conductors[J]. Supercond.Sci.Techonl., 2004, 17:S132-S134

46. Yamada Y, Muroga T, Iwai H, Watanabe T, Miyata S, Shiohara Y. Current status of pulsed laser deposition YBCO coated conductors in SRL using buffer layers by ion-beam assisted deposition GZO and self-epitaxy pulsed laser deposition CeO_2[J]. Supercond.Sci.Technol., 2004, 17:S328-S331

47. Hasegawa K, Fujino K, Mukai H, Konishi M, Hayashi K., Sato K., Honjo S, Ishii H, Iwata Y. Biaxially aligned YBCO tapes fabricated by all pulsed laser deposition[J]. Applied Superconductivity, 1996, 4(10-11):487-493

48. Balachandran U, Ma B, Li M, Fisher B L, Koritala R E, Miller D J, Dorris S E. Development of coated conductors by inclined substrate deposition[J]. Physica C, 2003, 392-396:806-814

49. Pomar A, Cavallaro A, Coll M, Gazquez J, Palau A, Sandiumenge F, Puig T, Obradors X, Freyhardt H C. All-chemical $YBa_2Cu_3O_7$ coated conductors on IBAD-YSZ stainless steel substrates[J]. Supercond.Sci.Technol., 2006, 19:L1-L4

50. Bhuiyan M S, Paranthaman M P, Kang S, Lee D F, Salama K. Growth of epitaxial Y_2O_3 buffer layers on biaxially textured Ni-W substrates for YBCO coated conductors by MOD approach[J]. Physica C, 2005, 422:95-101

51. Kim H S, Chung K C, Lee B S, Lim S M, Youm D. Direct current sputtering conditions for the growth of yttria-stabilized ZrO_2 buffer layers of coated conductors[J]. Supercond. Sci.Technol., 2004, 17:291-294

52. Kerstin Knoth, Ruben Huhne, Steffen Oswald, Schultz L, Holzapfel B. Highly textured $La_2Zr_2O_7$ buffer layers for YBCO-coated conductors prepared by chemical solution deposition[J]. Supercond.Sci. Technol., 2005, 18:334-339

53. Paranthaman M P, Aytug T, Zhai H Y, Heatherly L, Goyal A, Christen D K. Growth of YBCO films on MgO-based rolling-assisted biaxially textured substrates templates[J]. Supercond. Sci.Technol., 2005, 18:223-228

54. Groves J R, Arendt P N, Foltyn S R, Jia Q X, Holesinger T G, Kung H, Depaula R F, Dowden P C, Peterson E J, Stan L, Emmert L A. Recent progress in continuously processed IBAD MgO template meters for HTS applications[J]. Physica C, 2002, 382(1):43-47

55. Kakimoto K, Sutoh Y, Kaneko N, Iijima Y, Saitoh T. Research of long IBAD-PLD coated conductors with high quality[J]. Physcia C, 2005, 426-431:858-865

56. Kim C S, Jo S J, Jeong M, Kim W J, Baik H K, Lee S J, Song K M. Study of growth of biaxially textured CeO_2 films during ion-beam-assisted deposition[J]. Supercond.Sci. Technol., 2005, 18:330-333

57. Jarzina H, Sievers S, Jooss Ch, Freyhardt H C, Lobinger P, Roesky H W. Epitaxial MOD-YSZ buffer layers on IBAD-YSZ substrates[J]. Supercond.Sci.Technol., 2005, 18:260-263

58. Uprety K K, Ma B, Koritala R E, Fisher B L, Dorris S E, Balachandran U. Growth and properties of YBCO-coated conductors on biaxially textured MgO films prepared by inclined substrate deposition[J]. Supercond.Sci.Technol., 2005, 18:294-298

59. Xu Y, Lei C H, Ma B, Evans H, Efstathiadis H, Rane M, Massey M, Balachandran U, Bhattacharya R. Growth of textured MgO through e-beam evaporation and inclined substrate deposition[J], Supercond.Sci.Technol., 2006, 19:835-843

60. Goyal A. RABiTS: Status and Issues. HTS Wire development workshop, 2003

61. Papageorgopoulos C A, Kamaratos M. Adsorption of elemental S on Ni(100) surface[J]. Surface Science, 1995, 338:77-82

62. Blaszczyszyn M, Blaxzczyszyn R, Meclewski R, Melmde A J, Madey T E. Interactions of sulfur with nickel surfaces: Adsorption, diffusion and desorption[J]. Surface Science, 1983, 131:433-447

63. Partridge A, Tatlock G J, Leibsle F M, Flipse C F, Hormandinger G, Pendry J B.

Scanning-tunneling-microscopy investigation of the p(2×2) and c(2×2) overlayers of S on Ni(100)[J]. Physical Review B, 1993, 48(11):8267-8276

64. Cantoni C, Christen D K, Feenstra R, Goyal A, Ownby G W, Zehner D M, Norton D P. Reflection high-energy electron diffraction studies of epitaxial oxide seed-layer growth on rolling-assisted biaxially textured substrate Ni(001): The role of surface structure and chemistry[J]. Appl.Phy.Lett., 2001, 79(19):3077-3079

65. Cantoni C, Christen D K, Heatherly L, Kowalewski M M, List F A, Goyal A, Ownby G W, Zehner D M, Kang B W, Kroeger D M. Quantification and control of the sulfur c (2x2) superstructure on {100}<100> Ni for optimization of YSZ, CeO_2 and $SrTiO_3$ seed layer texture[J]. J.Mater.Res., 2002, 17(10):2549-2554

66. Goyal A, Lee D F, List F A, Specht E D, Feenstra R, Paranthaman M, Cui X, Lu S W, Martin P M, Kroeger D M, Christen D K, Kang B W, Norton D P, Park C, Verebelyi D T, Thompson J R, Williams R K, Aytug T, Cantoni C. Recent progress in the fabrication of high-Jc tapes by epitaxial deposition of YBCO on RABiTS[J]. Physica C, 2001, 357-360:903-913

67. Kim K, Kwon Y W, Norton D P, Christen D K, Budai J D, Sales B C, Chisholm M F, Cantoni C, Marken K. Epitaxial $(La,Sr)TiO_3$ as a conductive buffer for high temperature superconducting coated conductors[J]. Solid-State Electronics, 2003, 47:2177-2181

68. Aytug T, Paranthaman M, Kang B W, Sathyamurthy S, Goyal A, Christen D K. $La_{0.7}Sr_{0.3}MnO_3$: A single, conductive-oxide buffer layer for the development of $YBa_2Cu_3O_{7-\delta}$ coated conductors[J]. Applied Physics Letters, 2001, 79(14):2205-2207

69. Zhu X B, Liu S M, Hao H R, Li H X,Song W H, Sun Y P. Chemical solution deposition preparation of $Sr_{1-x}La_xTiO_3$ $(0\leq x\leq 0.4)$ buffer layers for YBCO coated conductors[J]. Physica C, 2005, 418:59-62

70. Bhuivan M S, Paranthaman M P, Sathvamurthv S, Aytug T, Kang S, Lee D F, Goyal A, Payzant E A, Salama K. MOD approach for the growth of epitaxial CeO_2 buffer layers on biaxially textured Ni-W substrates for YBCO coated conductors[J]. Supercond.Sci.Technol., 2003, 16:1305-1309

71. Jun B H, Sun J W, Kim H J, Lee D W, Jung C H, Park S D, Kim C J. Fabrication of YSZ buffer layer by single source MOCVD technique for YBCO coated conductor[J]. Physica C, 2003, 392-396:867-872

72. Arendt P N, Foltyn S R, Civale L, Depaula R F, Dowden P C, Groves J R, Holesinger T G, Jia Q X, Kreiskott S, Stan L, Usov I, Wang H, Coulter J Y. High critical current YBCO coated conductors based on IBAD MgO[J]. Physica C, 2004, 412-414:795-800

73. Wang H, Foltyn S R, Arendt P N, Jia Q X, Li Y, Zhang X. Thickness effects of $SrTiO_3$ buffer layers on superconducting properties of $YBa_2Cu_3O_{7-\delta}$ coated conductors[J]. Physica C, 2005, 433:43-49

74. Matsumoto K, Takechi A, Ono T, Hirabayashi I, Osamura K. Effect of perovskite oxide cap layer on superconducting properties of $YBa_2Cu_3O_x$ films grown on mechanically polished SOE substrates[J]. Physica C, 2003, 392-396:830-834

75. Engel S, Knoth K, Huhne R, Schultz L, Holzapfel B. An all chemical solution deposition approach for the growth of highly textured CeO_2 cap layer on $La_2Zr_2O_7$-buffered long lengths of biaxially textured Ni-W substrates for YBCO-coated conductors[J]. Supercond. Sci.Technol., 2005, 18:1385-1390

76. Akin Y, Heiba Z K, Sigmund W, Hascicek Y S. Engineered oxide thin films as 100% lattice match buffer layers for YBCO coated conductors[J]. Solid-State Electronics, 2003, 47:2171-2175

77. Worz B, Heinrich A, Stritzker B. Epitaixal NiO buffer layer by chemical enhanced surface oxidation epitaxy on Ni-5%W RABiTS for YBCO coated conductors[J]. Physica C, 2005, 418:107-120

78. Takechi A, Matsumoto K, Osamura K. $YBa_2Cu_3O_{7-x}$ films on oxide buffer layer with perovskite structure prepared by metal-organic deposition method[J]. Physcia C, 2003, 392-396:895-899

79. Paranthaman M P. Strategic buffer layer R&D for YBCO coated conductors[C]. HTS wire development workshop, 2003

80. Malozemoff A P, Annavarapu S, Fritzemeier L, Li Q, Prunier V, Rupich M, Thieme C, Zhang W. Low-cost YBCO coated conductor technology[C]. Eucas Conference, 1999

81. Paranthaman M P, Sathyamurthy S, Heatherly L, Martin P M, Goyal A, Kondenkandath T, Li X, Thieme C L H, Rupich M W. All MOD buffer/YBCO approach to coated conductors[J]. Physica C, 2006, 445-448:529-532

82. Yamada Y, Muroga T, Iwai H, Watanabe T, Miyata S, Shiohara Y. Progress of PLD and IBAD processes for YBCO wire in the SRL-Nagoya coated conductor center – new method for a coated conductor using a self-epitaxial PLD-CeO2 buffer[J]. Supercond.Sci.Technol., 2004, 17:S70-S73

83. 吴自勤, 王兵. 薄膜生长[M]，北京：科学出版社，2001

84. Teranishi R, Izumi T, Shiohara Y. Highlighs of coated conductor development in Japan[J]. Supercond.Sci.Technol., 2006, 19:S4-S12

85. Haugan T, Barnes P N, Brunke L, Maartense I, Murphy J. Effect of O_2 partial pressure on $YBa_2Cu_3O_{7-\delta}$ thin film growth by pulsed laser deposition[J]. Physica C, 2003, 397:47-57

86. Murugesan M, Obara H, Kosaka S, Nakagawa Y, Nie J C, Yamasaki H. Growth and characterization of PLD grown $Dy_{0.4}Ho_{0.6}Ba_2Cu_3O_z$ thin films[J]. Physica C 2004, 411:72-76

87. Varesi E, Celentano G, Petrisor T, Boffa V, Ciontea L, Galluzzi V, Gambardella U, Mancini A, Ruflolni A, Vannozzi A. Pulsed laser deposition of high critical current density $YBa_2Cu_3O_{7-x}/CeO_2$/Ni-W architecture for coated conductors applications[J]. Supercond.Sci. Technol. 2003, 16:498-505

88. Rupich M W, Zhang W, Li X, Kodenkandath T, Verebelyi D T, Schoop U, Thieme C, Teplitsky M, Lynch J, Nguyen N, Siegal E, Scudiere J, Maroni V, Venkataraman K, Miller D, Holesinger T G. Progress on MOD/RABiTS 2G HTS wire[J]. Physica C, 2004, 412-414: 877-884

89. Zhu X B, Chen L, Liu S M, Song W H, Sun Y P, Shi K, Sun Z Y, Chen S, Han Z. Effect of seed layers on the preparation of $SrTiO_3$ buffer layers on Ni tapes via sol-gel method[J]. Physcia C 2004, 415:57-61

90. Obradors X, Puig T, Pomar A, Sandiumenge F, Pinol S, Mesters N, Castano O, Coll M, Cavallaro A, Palau A, Gazquez J, Gonzalez J C, Gutierrez J, Roma N, Ricart S, Moreto J M, Rossell M D, Tendeloo G van. Chemical solution deposition: a path towards low cost coated conductors[J]. Supercond.Sci.Technol., 2004, 17:1055-1064

91. Morlens S, Ortega L, Rousseau B, Phok S, Deschanvre J L, Vhaudouet P, Odier P. Use of cerium ethylhexanoate solutions for preparation of CeO_2 buffer layers by spin coating[J]. Materials Science and Engineering B, 2003, 104:185-191

92. Yu Z M, Oider P, Ortega L, Zhou L, Zhang P X, Girard A. $La_2Zr_2O_7$ films on Cu-Ni alloy by chemical solution deposition process[J]. Materials Science and Engineering B, 2006, 130:126-131

93. Schwartz R W. Chemical solution deposition of perovskite thin films[J]. Chem.Mater. 1997, 9:2325-2340

94. Bhuiyan M S, Paranthaman M, Salama K. Solution-derived textured oxide thin films — a review[J]. Supercond.Sci. Technol. 2006, 19:R1-R21

95. Lange F F. Chemical solution routes to single-crystal thin films[J], Science, 1996, 273:903

96. Sandiumenge F, Cavallaro A, Gazquez J, Puig T, Obradors X, Arbiol J, Freyhardt H C. Mechanisms of nanostructural and morphological evolution of CeO_2 functional films by chemical solution deposition[J]. Nanotechnology, 2005, 16:1809-1813

97. Chen Y M. MOCVD process for coated conductors[C]. 2005 wire development workshop

98. Matsumoto K, SeokBeom Kim, Jian-Guo Wen, Hirabayashi I. Fabrication of In-plane aligned YBCO films on polycrystalline Ni tapes buffered with surface-oxidized NiO layers[J]. IEEE Trans. Appl.Supercond., 1999, 9(2):1539-1542

99. Katsuya Hasegawa, Toru Izumi, Teruo Izumi, Yuh Shiohara, Toshihiko Maeda. Improvement of in-plane alignment for surface oxidized NiO layer on textured Ni substrate by two-step heat-treatment[J]. Physica C 2004, 412-414:864-870

100. Gupta A, Jagannathan R, Cooper E I, Giess E A, Landman J I, Hussey B W. Superconducting oxide-films with high transition temperature prepared form metal trifluoroacetate precursors[J]. Appl.Phys.Lett., 1988, 52(24):2077-2079

101. Takeshi Araki, Izumi Hirabayashi. Review of a chemical approach to $YBa_2Cu_3O_{7-x}$-coated superconductors — metalorganic deposition using trifluoroacetates[J]. Supercond.Sci.Technol. 2003, 16:R71-R94

102. Tokunaga Y, Honjo T, Izumi T, Shiohara Y, Iijima Y, Saitoh T, Goto T, Yoshinake A, Yajima A. Advanced TFA-MOD process of high critical current YBCO films for coated conductors[J]. Cryogenics, 2004, 44:817-822

103. Honjo T, Nakamura Y, Teranishi R, Tokunaga Y, Fuji H, Shibata J, Asada S, Isumi T, Shiohara Y, Iijima Y, Saitoh T, Kaneko A, Murata K. Fabrication and growth mechanism of YBCO coated conductors by TFA-MOD process[J]. Physica C, 2003, 392-396:873-881

104. Teranishi R, Honjo T, Nakamura Y, Fuji H, Tokunaga Y, Matsuda J, Izumi T, Shiohara Y. Growth mechanism of YBCO film by TFA-MOD process[J]. Physica C, 2003, 392-396:882-886

105. Kaneko A, Fuji H, Teranishi R, Tokunaga Y, Matsuda J S, Asada S, Murata K, Honjo T, Izaumi T, Shiohara Y, Goto T, Yoshinaka A, Yajima A. Fabrication of REBa2Cu3O7-y film by advanced TFA-MOD process[J]. Physica C 2004, 412-414:926-930

106. Paranthaman M P. Current Status of the national project of coated conductors in Japan. 2005 wire development workshop.

107. Kashima N, Niwa T, Mori M, Nagaya S, Muroga T, Miyata S, Watanabe T, Yamada Y, Izumi T, Shiohara Y. YBCO coated conductor by multiple-stage CVD[J]. Physica C, 2005, 426-431:887-892

108. Xie Y Y, Knoll A, Chen Y, Li Y, Xiong X, Qiao Y, Hou P, Reeves J, Salagaj T, Lenseth K, Civale L, Maiorov B, Iwasa Y, Solovyov V, Suenaga M, Cheggour N, Clicker C, Ekin J W, Weber C, Selvamanickam. Progress in scale-up of second-generation high-temperature superconductors at SuperPower Inc[J]. Physica C, 2005, 426-431:849-857

109. Ma B, Li M, Koritala R E, Fisher B L, Markowitz A R, Erck R A, Baurceanu R, Dorris S E, Miller D J, Balachabdran U. Pulsed laser deposition of YBCO films on ISD MgO buffered metal tapes[J]. Supercond.Sci.Technol., 2003, 16:464-472

110. Barnes P N, Nekkanti R M, Haugan T J, Campbell T A, Yust N A, Evans J M. Pulsed laser deposition of YBCO coated conductor using Y_2O_3 as the seed and cap layer[J]. Supercond. Sci.Technol., 2004, 17:957-962

111. Iwai H, Muroga T, Watanabe T, Miyata S, Yamada Y, Shiohara Y, Kato T, Hirayama T. Investigation of high Jc $YBa_2Cu_3O_{7-x}$ coated conductors prepared by pulsed laser deposition on self-epitaxial CeO_2 buffers[J]. Supercond.Sci.Technol., 2004, 17:S496-S499

112. Christen H M, Lee D F, List F A, Cook S W, Leonard K J, Heatherly L, Martin P M, Paranthaman M, Goyal A, Rouleau C M. Pulsed electron deposition of fluorine-based precursors for $YBa_2Cu_3O_{7-x}$-coated conductors[J]. Supercond.Sci.Technol., 2005, 18:1168-1175

113. Ichinose A, Kikuchi A, Kiss T, Tachikawa K, Akita S, Inoue K. Preparation and microstructures of high current density YBCO films by no-water post-annealing of precursor films including BaF_2[J]. Physica C, 2003, 392-396:927-931

114. Lee D F, Leonard K J, Heatherly Jr, Yoo J, List F A, Rutter N, Cook S W, Sathyamurthy S, Paranthaman M, Martin P M. Reel-to-reel ex situ conversion of high critical current density electron-bean co-evaporated BaF2 precursor on RABiTS[J]. Supercond.Sci.Technol., 2004, 17:386-394

115. Qi X, Lockman Z, Bugoslavsky Y, Kursumovie A, Tomov R, Glowacki B A, Evetts J E, MacManus-Driscoll J L. YBCO/Nd_2CuO_4/NiO/Ni coated conductors fabricated by liquid phase epitaxy based techniques[J]. Supercond.Sci.Technol., 2004, 17:1144-1147

116. Yoo J, Leonard K J, Hsu H S, Heatherly L, List F A, Lee D F, Gapud A A, Martin P M, Cook S, Paranthaman M, Goyal A, Kroeger D M. The growth of YBCO films with high critical current at reduced pressures using the BaF_2 ex situ process[J]. Supercond.Sci.Technol., 2004, 17:1209-1214

117. Odier P, Supardi Z, De-Barros D, Vergnieres L, Ramirez-Castellanos J, Gonzales-Calbet J M, Vallet-Regi M, Villard C, Peroz Ch, Weiss F. Spray pyrolysis for high Tc superconductors films[J]. Superconduct.Sci.Technol., 2004, 17:1303-1310

118. Shiohara Y, Yoshizumi M, Izumi T, Yamada Y. Current status and prospects of national project on coated conductors in Japan[J]. Physica C, 2007, 4463-465:1-6

119. Chirayil T G, Paranthaman M, Beach D B, Lee D F, Goyal A, Williams R K, Cui X, Kroeger D M, Feenstra R, Verebelyi D T, Christen D K. Epitaxial growth of La2Zr2O7 thin films on rolled Ni-substrate by sol-gel process for high Tc-superconducting tapes[J]. Physica C, 2000, 336:63-69

120. Sathyamurthy S, Paranthaman M, Zhai H Y, Kang S, Aytug T, Cantoni C, Leonard K J, Payzant E A, Christen H M, A. Goyal. Chemical solution deposition of lanthanum zirconate barrier layers applied to low-cost coated-conductor fabrication[J]. J.Mater.Res., 2004, 19:2117-2123

121. 毛为民, 张新明. 晶体材料织构定量分析[M]，北京：冶金工业出版社，1995

122. Truszkowski W, Krol J, Major B. On penetration of shear texture into the rolled aluminum and copper[J]. Metallurgical transactions A, 1982, 13A:665-669

123. Schoenfeld S E, Asaro R J. Through thickness texture gradients in rolled polycrystalline alloys[J]. Int.J.Mech.Sci., 1996, 38(6):661-683

124. Wenk H R. Houtte P V. Texture and Anisotropy[J], Rep.Prog.Phys., 2004, 67:1367-1428

125. Reddy A K N. Preferred orientations in nickel electro-deposits[J]. Journal of electroanalytical chemistry, 1963, 6:141-152

126. Pangarov N A. Preferred orientations in electro-deposited metals[J]. Journal of electroanalytical

chemistry, 1965, 9:70-85

127. Amblard J, Epelboin I, Froment M, Maurin G. Inhibition and nickel electrocrystallization[J]. Journal of applied electrochemistry, 1979, 9:233-242

128. 黄子勋. 实用电镀技术[M]. 北京：化学工业出版社，2002

129. Yan Q G, Wu T H, Li J T, Luo C R, Weng W Z, Yang L F, Wan H L. Mechanism study of carbon deposition on Ni/Al2O3 catalyst during partial oxidation of methane to syngas. Journal of Natural Gas Chemistry, 2000, 9(2): 92-93

130. Seo J W, Fompeyrine J, Guiller A, Norga G, Marchiori C, Siegwart H, Locquet J P. Interface formation and defect structures in epitaxial La2Zr2O7 thin films on (111) Si[J]. Applied Physics Letters, 2003, 83(25):5211-5213

Le Coated Conductor est un empilement de couches tampon sur un substrat, il est composé d'un substrat métallique, de couches tampon, d'une couche d'YBCO et d'une couche protectrice. Développer de bons substrats métalliques, simplifier l'architecture des couches tampon et trouver des méthodes de fabrication d'YBCO économiques sont les sujets essentiels de ce domaine. On a développé un nouveau substrat bimétallique Cu-Ni par dépôt électrochimique d'une couche de Ni sur un ruban de cuivre texturé et on discute comment déposer un film de $La_2Zr_2O_{7\,(LZO)}$, de même texture, sur un substrat métallique par un processus chimique en solution (CSD). La fabrication de rubans de Cu texturé par un procédé de laminage-recristallisation est présentée en premier, puis on s'intéresse au dépôt électrochimique du Ni sur ces rubans. La stabilité thermique de la texture et les propriétés magnétiques de ces substrats Cu-Ni est discutée. Le dépôt d'une couche tampon de LZO texturée sur ces substrats par le procédé CSD confirme leur intérêt potentiel pour les Coated Conductors. Le dépôt de couches de LZO sur divers substrats métalliques, la préparation de précurseurs et des substrats, la croissance épitaxiale de couches tampon de LZO sont discutés en détail. On montre que l'acetylacétonate dissout dans l'acide propionique est une bonne solution. Une couche de S de structure c(2x2) à la surface du substrat permet le contrôle de l'orientation initiale des couches de LZO. Le carbone résiduel issu de la synthèse de LZO est un facteur inhibant la croissance des grains de LZO mais son gradient sous la surface est utile. La maitrise de l'ensemble de ces facteurs permet la formation de couches de haute qualité.

Coated conductor is a stack of buffer films on a substrate and can be divided into four parts: metallic substrate, buffer layers, YBCO layer and protecting layer. Developing appropriate metallic substrate, simplifying the architecture of buffer layers and finding an economical process for the YBCO layer are the three essential areas of this field. One has developed a new bi-metallic substrate by electro-depositing a Ni layer on a textured Cu tape, and we discuss how to fabricate a textured $La_2Zr_2O_7$(LZO) film on a metallic substrate by the chemical solution deposition (CSD) process. The fabrication of textured Cu tapes by a rolling-recrystallization process is discussed first, and then the electro-deposition of a Ni layer on this tape is presented. The thermal stability of texture and the magnetic property of this Cu-Ni substrate are discussed. The deposition of a textured LZO buffer layer by CSD confirms the potential interest of this substrate for coated conductors. The deposition of a LZO buffer layer, the preparation of a precursor solution and of the substrate, the epitaxial growth of LZO buffer layer are discussed in details. It is proved that a solution of acetylacetonate dissolved into propionic acid is a good precursor solution. A very thin film of S with the structure c(2×2) at the surface of the substrate is beneficial for controlling the orientation of initial LZO layer. The residual carbon issued from the synthesis of LZO is an inhibiting factor of the growth but its distribution gradient under the surface is useful. A good control of all these factors is a key for processing high quality buffers.